Forward and Inverse Models of Electromagnetic Scattering From Layered Media With Rough Interfaces

by

Seyed Alireza Tabatabaeenejad

A dissertation submitted in partial fulfillment
of the requirements for the degree of
Doctor of Philosophy
(Electrical Engineering)
in The University of Michigan
2008

Doctoral Committee:

       Associate Professor Mahta Moghaddam, Chair
       Professor Fawwaz T. Ulaby
       Associate Professor Peter D. Miller
       Assistant Professor Anthony Grbic

ABSTRACT

Forward and Inverse Models of Electromagnetic Scattering From Layered
Media With Rough Interfaces

by

Seyed Alireza Tabatabaeenejad

Chair: Mahta Moghaddam

This work addresses the problem of electromagnetic scattering from layered dielectric structures with rough boundaries and the associated inverse problem of retrieving the subsurface parameters of the structure using the scattered field. To this end, a forward scattering model based on the Small Perturbation Method (SPM) is developed to calculate the first-order spectral-domain bistatic scattering coefficients of a two-layer rough surface structure. SPM requires the boundaries to be slightly rough compared to the wavelength, but to understand the range of applicability of this method in scattering from two-layer rough surfaces, its region of validity is investigated by comparing its output with that of a first principle solver that does not impose roughness restrictions. The Method of Moments (MoM) is used for this purpose. Finally, for retrieval of the model parameters of the layered structure using scattered field, an inversion scheme based on the Simulated Annealing method is investigated and a strategy is proposed to address convergence to local minimum.

To my parents and my sister.

ACKNOWLEDGEMENTS

I would like to sincerely thank my research advisor Professor Mahta Moghaddam for her continuous support and encouragement, for the opportunity she provided for me to conduct independent research, and for her exemplary respect for my otherness. I would also like to thank my dissertation committee members, Professor Fawwaz Ulaby, Professor Peter Miller, and Professor Anthony Grbic for accepting to be on my dissertation committee. I feel grateful to Professor Eric Michielssen for accepting to be on my dissertation committee despite the fact that he was going to be out of the United States at the time of my defense. Professor Eric Michielssen was my co-advisor on Chapter 3.

I owe my first research advisor, Professor John Volakis, a great debt of gratitude for his great support during the first two years of my graduate studies at the University of Michigan.

I would like to acknowledge the unconditional help Dr. Leland Pierce provided for me with programming in FORTRAN.

The supportive work and efforts of the staff members of my department are hereby acknowledged. I would also like to sincerely thank all of my friends in the Radiation Laboratory for their invaluable friendship. I am especially grateful to Jane Whitcomb and Dr. Mojtaba Dehmollaian for editing this dissertation and to Farhad Bayatpur, Dr. Amelia Buerkle, Mark Haynes, Mehrnoosh Vahidpour, and Jacquelyn Vitaz for attending the rehearsal for my presentation.

I would like to thank all of my Iranian friends, especially Dr. Reza Azadegan, Dr. Nader Behdad, and Dr. Mojtaba Dehmollaian, for their invaluable friendship and support since the very first days I came to the United States.

TABLE OF CONTENTS

LIST OF FIGURES

LIST OF TABLES

LIST OF APPENDICES

APPENDIX

CHAPTER 1

Introduction

1.1   Problem Statement

The thrust of this dissertation is the problem of electromagnetic scattering from layered dielectric structures with rough boundaries and the associated inverse problem of retrieving the subsurface parameters of the structure using the scattered field. This work has several important applications such as retrieval of soil moisture, which is of fundamental importance to environmental engineering, hydrology, geology, soil physics, civil engineering, and planetary sciences. Exploration of resources such as oil, space explorations such as searching for water on planets, detection of Improvised Explosive Devices (IEDs), and medical imaging are a few other applications of the problems addressed in this dissertation.

1.2   Overview of the Study

A layered structure with homogenous dielectric layers and slightly rough boundaries is considered. The Small Perturbation Method (SPM) is applied to the first order and the scattered field is calculated. The scattered field is first calculated for a two-layer case and then for an N-layer structure. The region of validity of the forward model in a two-layer case is also addressed. The work then focuses on the problem of retrieving the model parameters of the two-layer structure using synthesized backscattering coefficients at different frequencies and incidence angles. The inverse problem is formulated as a parameter estimation problem

that is solved using a global optimization scheme known as the Simulated Annealing.

1.3 Background and Motivation

The problem of scattering from random rough surfaces has been the subject of numerous studies dating back to the 1950's, starting with a single rough surface [1–3]. Researchers have continued developing new rough surface scattering models over the past decades to increase the accuracy of the old models over various parameters of the rough surface [4]. The interest in this problem is due to the fact that layered structures with rough boundaries are representative models for many naturally occurring surface and subsurface structures ranging from layered soil, rivers, lakes, and multi-year ice to smaller scale objects such as the human body and manufactured optical components comprised of metal-deposited dielectrics.

Among the wide range of applications of scattering from rough surfaces, study of soil moisture is of fundamental importance to many hydrological and biological processes. Soil moisture information is critical to agencies and companies concerned with weather and climate, runoff potential and flood control, soil erosion, reservoir management, geotechnical engineering, and water quality. Soil moisture plays a fundamental role in controlling the exchange of water and heat energy between the land surface and the atmosphere through evaporation and plant transpiration. Consequently, soil moisture becomes a key factor in the development of weather patterns and production of precipitation. Simulations have shown that improved characterization of surface soil moisture, vegetation, and temperature can lead to significant weather forecast improvements. Soil moisture also strongly affects the amount of precipitation that runs off into nearby streams and rivers. Large-scale dry or wet surface regions have been observed to impart positive feedback on subsequent precipitation patterns, such as in the extreme conditions over the central U.S. during the 1988 drought and the 1993 floods. Soil moisture information can be used for reservoir management, early warning of droughts, irrigation scheduling, and crop yield forecasting.

Effects of soil moisture and surface roughness on the backscattered field have been studied dating back to the 1960's and 70's [5–7]. Research in soil moisture remote sensing began in the mid 1970's shortly after the surge in satellite development [8, 9]. Studies have widely

been done in the microwave regime of the electromagnetic spectrum, because microwave measurements are largely unaffected by clouds, and, up to wavelengths of about 3 cm, are also unaffected by rain. Furthermore, microwave sensors do not depend on solar radiation as the source of target illumination. Quantitative measurements of soil moisture in the surface layer of soil have been most successful using passive remote sensing, but use of radiometers in soil moisture detection is limited because of their low resolution at lower frequencies, which are required for subsurface observations.

The frequencies used for study of soil moisture should be chosen judiciously in order to allow use of appropriate scattering models and allow obtaining reliable data. Accuracy of the scattering model and penetration through soil are two important factors that should be considered when a measurement system is being designed. Moreover, since 30% of the Earth land area is covered with vegetation, penetration through vegetation cover is another important factor that needs to be considered. To probe the properties of soil, we can ideally use three ranges of frequencies: L-band (1–2 GHz), UHF (0.3–3 GHz), and VHF (30–300 MHz). The penetration depth increases as the frequency decreases. Lower frequency microwaves are needed to achieve penetration through soil, because they retain their information content while they travel through significant vegetation canopies and through soil. L-band can be used to estimate soil moisture in the top 0–5 cm in the presence of up to 4 kg/m^2 of vegetation [10–15]. UHF measurements enhance the capability to characterize vegetation effects as the amount of vegetation is increased to up to 20 kg/m^2 [16, 17] and to retrieve soil moisture in the 0–50 cm depth [18]. VHF data are essential for retrieving soil moisture under vegetation canopies exceeding 20 kg/m^2 and to depths of 2 m or more, depending on the amount of moisture present. Data from low-frequency experimental systems such as the Microwave Observatory of Subcanopy and Subsurface (MOSS) tower radar [19] and actual airborne systems such as the NASA/JPL AIRSAR [18] have shown the practical and theoretical feasibility of obtaining reliable radar data and subsurface soil moisture products at low frequencies, legitimizing use of scattering models such as SPM, because this method assumes that roughness of the surfaces is small compared to the wavelength, which is a valid assumption at low frequencies. We should note that at least one of the higher frequencies (L-band or C-band) must be present for separating, characterizing, and removing the

3

contribution of the vegetation layer.

Study of sea ice is another motivation for development of electromagnetic models for rough surface scattering. Surface roughness, dielectric properties, and thickness of sea ice influence the signal received at the antenna, so the geophysical properties of sea ice can be retrieved using scattered field data.

Sea ice is important to the global climate because of its role in the mass balance and heat transfer between the ocean and the atmosphere [20, 21]. Sea ice modulates energy exchange between the ocean and the atmosphere, because its high albedo and insulation deflect solar radiation and prevents a significant amount of heat in the ocean from warming the polar atmosphere. Sea ice thickness determines the amounts of energy exchange between the air and the ocean. The thicker the ice cover, the more effective is the insulation between the cold polar air and the warm ocean. Sea ice also plays an important role in the surface radiation budget. Because of its high albedo, sea ice can reflect up to 90% of the solar radiation. On the other hand, the open ocean absorbs most of the solar energy (85–90%) due to its low albedo. Consequently, changes in sea ice extent over time can be an indicator of the energy being retained by the Earth. A negative change in the sea ice extent would indicate a global warming scenario.

The detection and classification of sea ice are important remote sensing applications. The distinct difference in backscatter between open water and that of sea ice—which is relatively much higher—helps in the detection of sea ice. The classification of sea ice, on the other hand, is more complex and is important for estimating ice thickness, hence amount of insulation provided by the sea ice cover. For remote sensing purposes, sea ice can be categorized into perennial multi-year ice, which is generally 3–6 m thick, and new first-year ice, which is relatively thin (1–2 m). It is important to distinguish between different ice ages, particularly first-year ice and multi-year ice. This is especially important in navigation, because multi-year ice is usually more dangerous to ships than first-year ice because of its greater thickness and the fact that it also has more ridges. Multi-year ice and first-year ice have distinct backscatter signatures, which allows us to distinguish them using remote sensing.

It is of extreme importance that we monitor the Earth's sea ice on a global scale. Sea ice is difficult to study directly, because it is in such remote locations. Ships and submarines

have been used to gather data for sea ice, and scientists have established field camps and deployed ocean buoys in the Arctic to study the movement of sea ice. The problem with these methods is that they only explain sea ice conditions in relatively small regions. The only way we can monitor sea ice globally is by remote sensing from satellites. As a result, global monitoring of sea ice with polarimetric radar remote sensing has drawn considerable interest [22–24]. Satellite and airborne instruments collect data that can be used to retrieve the area covered by sea ice, sea ice temperature, sea ice motion, and other variables.

Because of high albedo of snow and natural insulation of the underlying surface, snow mapping is also important for climate studies as well as for estimating spring runoff amounts for predicting water supply, hydroelectric energy production, and potential flooding. Given its large spatial extent and sensitivity to microwave electromagnetic radiation, microwave remote sensing is a useful tool for mapping snow. Contrast between the backscatter from soil, especially frozen soil, and that of snow is used to detect snow. Moreover, variations in scattered field at the same location can be used to detect seasonal transitions of landscapes. As soils and vegetation freeze with colder temperatures in the winter, surface roughness and dielectric constants decrease, leading to low backscatter values. Then, as snow begins to fall and accumulate over the landscape, backscatter values increase due to strong volume scattering of microwave energy within the snow pack, especially at higher frequencies. When winter ends and temperatures rise again, snow begins to melt and the presence of unabsorbed liquid water leads to rapid decreases in backscatter due to absorption. Lastly, as snow departs and soils and vegetation begin to thaw, backscatter values begin to rise again as absorbed moisture in the soils and vegetation increases their dielectric constants.

There exist other applications of rough surface scattering such as study of backscattering enhancement. Backscattering enhancement finds applications in the study of scattering phenomena from metallic surfaces with a dielectric coating and metallic coated papers. Backscattering enhancement is a phenomenon in rough surface scattering which manifests itself as a well-defined peak in the backscattering direction [25]. Both theoretical [26, 27] and experimental [28] research efforts have previously been made to study backscattering enhancement effect of rough surfaces due to surface plasmon resonance. Backscattering enhancement of surface plasmon waves is important in various applications, including surface

plasmon localization in rough-metal surfaces and ocean acoustic applications [25]. It is also an emerging area of interest in biological applications and has provided a new means to detect and image biological interfaces of thickness well below the diffraction limit [29].

The aforementioned areas are fraught with challenges. However, extensive studies have been devoted to these subjects [19, 30–32]. The challenge shared between these areas is development of appropriate forward and inverse rough surface scattering models. Soil dielectric properties and structural properties of multi-year sea ice and snow-covered lands legitimize modeling these media as layered structures. Soil dielectric profiles strongly depend on soil type, temperature profile, surface evaporation and moisture content. The real part of the dielectric constant at VHF ranges from 3 for dry soil to about 30 for wet soil [33]. Therefore, backscattering coefficients at this frequency band could vary significantly depending on the ground moisture regime. Along with a non-uniform soil moisture function in depth, soil consists of different subsurface layers that could be homogeneous, consist of arbitrarily varying continuous profiles, or represented by inhomogeneous media composed of various dispersive constituents. These layers are typically rough. Because of the presence of both inhomogeneous dielectric profiles as well as irregular soil layers, the need for a layered dielectric model with rough boundaries is a necessity in the development of scattering models at low frequencies. Similarly, multi-year ice is usually very deformed and rough at the surface due to wave-caused deterioration, ice-pack shearing, and melting/refreezing cycles that occur over time. First-year ice can also be somewhat rough due to ridging at the edges caused by wave action and collision with other bodies of ice. We may therefore model first-year ice as a one-layer rough surface structure whereas multi-year ice needs to be modeled as a layered structure with rough boundaries.

1.4 Dissertation overview

This dissertation has three main chapters along with the Introduction chapter and a conclusion statement.

Chapter 2 presents a solution to electromagnetic scattering from a three-dimensional (3D), layered dielectric structure with rough boundaries using SPM. The first-order spectral-

Figure 1.1: Layered soil is an example of layered structures with rough boundaries.

domain bistatic scattering coefficients of a two-layer structure is calculated. The amplitudes of the fields in all regions are obtained simultaneously. The solution is analytical and intrinsically takes into account multiple scattering processes between the boundaries. The solution is then extended to an arbitrary number of layers. The method is fast and appropriate for being used in inversion schemes. This chapter emphasizes the theoretical analysis of the problem; however, the primary intent of the solution is for remote sensing applications involving layered soils.

Chapter 3 addresses the region of validity of SPM for a two-layer structure. The scattered field is calculated for a two-dimensional (2D), two-layer rough surface structure using the Method of Moments (MoM). The MoM solver needed for deriving the region of validity should be fast to allow extensive sampling of the model parameters. Therefore, a fast solver known as UV Multilevel Partitioning Method (UV-MLP) is presented. It is shown that, contrary to expectation, for the matrix sizes of interest, this method is not faster than a solver such as LU factorization. Finally, a comparison between the backscattering coefficients of

Figure 1.2: Sea ice plays an important role in the mass balance and heat transfer between the ocean and the atmosphere.

a two-layer structure calculated via SPM and MoM is presented, and recommendations are made on the region of validity with respect to the dielectric properties of the layers and statistical properties of the boundaries.

Chapter 4 addresses retrieval of the subsurface parameters of a three-dimensional, two-layer structure using scattered field. The inverse scattering problem considered here can be regarded as a nonlinear parameter-estimation problem. The problem is formulated as an optimization problem that is solved using an enhanced Simulated Annealing method. A strategy is proposed to escape from local minima and is shown to be effective. The algorithm is shown to be capable of retrieving the layers dielectric constants, conductivities, and the mean separation between the layers. All of the model parameters are considered well retrieved in presence of noise.

Chapter 5 concludes this dissertation, summarizes its contributions, and presents recommendations on future work.

CHAPTER 2

Bistatic Scattering from Three-Dimensional Layered Rough Surfaces

An analytical method to calculate the bistatic scattering coefficients of a three-dimensional, layered dielectric structure with slightly-rough interfaces is presented. The interfaces are allowed to be statistically distinct, but possibly dependent. The waves in each region are represented as a superposition of an infinite number of up- and down-going spectral components whose amplitudes are found by simultaneously matching the boundary conditions at both interfaces. A small-perturbation formulation is used up to the first order, and the scattered fields are derived. The calculation intrinsically takes into account multiple scattering processes between the boundaries. The formulation is then validated against known solutions to special cases. New results are generated for several cases of two- and three-layer media, which will be directly applicable for modeling of the signals from radar systems and subsequent estimation of a layered medium subsurface properties such as moisture content and layer depths.

2.1   Introduction

The problem of scattering from random rough surfaces has been the subject of numerous studies dating back to the 1950's, starting with a single rough surface [1–3]. The interest in this problem stems from the fact that random roughness is a representative model for many naturally occurring surface and subsurface structures such as soil and multi-year ice.

Rough surfaces are also encountered frequently in smaller scales such as in manufactured optical components comprised of dielectrics with metal deposits. This chapter presents a solution to the bistatic scattering coefficients of a three-dimensional, layered dielectric structure with rough boundaries using the small perturbation approximation for each rough surface. No other approximations are involved, and all multiple scattering processes between the boundaries are intrinsically considered in the calculation. While this chapter emphasizes the theoretical analysis of the problem, the primary intent of the solution is for remote sensing applications involving layered soils, to ultimately estimate the variations of the complex dielectric constant, hence the subsurface layers moisture content, as a result of changes in environmental conditions. With the development of low-frequency experimental systems such as the Microwave Observatory of Subcanopy and Subsurface (MOSS) tower radar [19], which is meant for estimation of deep soil moisture, the need for an accurate and practical layered-soil scattering model has become evident. The solution presented here addresses this need.

Solutions to a single rough surface abound, and can be divided into two general categories of analytical and numerical approaches. The most common analytical method assumes a slightly rough surface where the random surface height is assumed to be a zero-mean random process with a small mean-square variance. This method, pioneered by Rice [34] in 1951, is often referred to as the Small Perturbation Method (SPM), and has been further evolved into more sophisticated and/or practical approximate solutions [35, 36], including higher-order expansions [37, 38]. The order of expansion is arbitrary, with the complexity of solutions increasing with increasing order. The numerical approaches can be divided into time-domain and frequency-domain methods, with the former typically using a differential equation formulation as in the finite-difference time-domain method [39, 40], and the latter using surface integral equation formulations [39], [41–43]. The numerical techniques have the advantage that they do not rely on simplifying approximations to the surface roughness, and are able to simulate the scattering process for any arbitrary distribution and roughness scale. However, the computational cost is typically high, given that many realizations of the random surface have to be simulated. This is in contrast to the low computational burden of analytical solutions, which are obtained at the cost of complex analysis and approximate

results.

The order of complexity of analytical solutions increases when more layers are involved. Therefore, work on the subject has had limiting assumptions such as a single rough interface on top of or embedded in a layered medium [44–46] or a rough boundary backed by a perfectly conducting plate [47]. High-order solutions for layered media are even more involved. Ignoring multiple scattering between the rough boundaries [31] and using the reduced Rayleigh equations to eliminate scattered fields inside the layered medium in the simplest case of two independent rough boundaries [48], have been ways of simplifying the analysis. Another example is a recent semi-analytical semi-numerical method based on the extended boundary conditions used to analyze layered rough surfaces [49]. While this method accounts for high orders of scattering, it is computationally expensive. Therefore, analytical methods are still more attractive for applying to practical solutions of inverse problems, where several evaluations of the forward problem are needed.

An alternative approach to the problem is presented here with some advantages over previous methods. This approach has the SPM at its core. Fields in each region are represented as the summation of up-going and down-going waves, with their amplitudes found by simultaneously matching the boundary conditions for the continuity of tangential electric and magnetic fields at each rough boundary. The boundary conditions are imposed up to the first order, as in any other first-order SPM. However, the resulting equations are solved in the far-field region without any further approximations. Consequently, in contrast to some of the above methods, this method intrinsically takes into account multiple scattering processes between the boundaries, all of which are considered rough simultaneously. This makes the presented SPM approach different from some of the previous methods in that it is suitable for being extended to higher orders, because it does not rely on the assumption that each rough boundary contributes to the solution independently of the other boundaries, which is only true in the first-order solution. Also, the solution here is presented for the general case where the rough surfaces are not statistically independent, in which case the cross-correlation functions of the random interfaces are taken into account for the calculation of bistatic scattering coefficients. Another strength of this approach, in contrast to some of the methods above, is that the amplitudes of the fields scattered into the inner media are

obtained simultaneously without further calculation. Moreover, the formulation presented here can be easily and systematically extended to cases where an arbitrary number of layers with rough boundaries are involved. The details of extending the formulation is presented for transition from two layers to three layers. The first-order solution is presented here. While higher-order solutions have many applications in optics and areas where coherent effects and surface waves are important, for the intended soil moisture application, the higher-order effects are expected to be small.

In the following sections, the focus will be on a two-layer medium. First, the definitions and notations are presented, and are followed by the analysis leading to the bistatic scattering coefficients for both horizontal and vertical polarizations. Extension to the three-layer case is presented afterward. The results are then validated against known solutions to special cases. Finally, various new results are generated for arbitrary cases of two- and three-layer media.

2.2 Problem Geometry and Definitions

2.2.1 Geometry

Consider the three-dimensional, two-layer isotropic dielectric structure shown in Fig. 2.1, where the top and bottom regions are half-spaces. The layers dielectric constants are ϵ_0, ϵ_1, and ϵ_2, which in general could have complex values. The permeability of all layers is assumed to be μ_0, although this assumption does not impact the analysis method. The boundaries are denoted by $z = \xi f_1(x, y)$ and $z = -d_1 + \xi f_2(x, y)$, where both $f_1(x, y)$ and $f_2(x, y)$ are zero-mean, stationary random processes with known, distinct, but possibly dependent statistical properties. The quantity d_1 is the mean separation between the boundaries and is referred to as the first-layer thickness. The quantity ξ is the small perturbation parameter used to match the boundary condition equations to specific orders. The quantities $\xi \sigma_{f_1}$ and $\xi \sigma_{f_2}$ are assumed to be small numbers compared to the wavelength, where σ_{f_1} and σ_{f_2} are the standard deviations of $f_1(x, y)$ and $f_2(x, y)$, respectively. An accurate mathematical statement about how small these numbers should be and what the limitations on the correlation lengths of
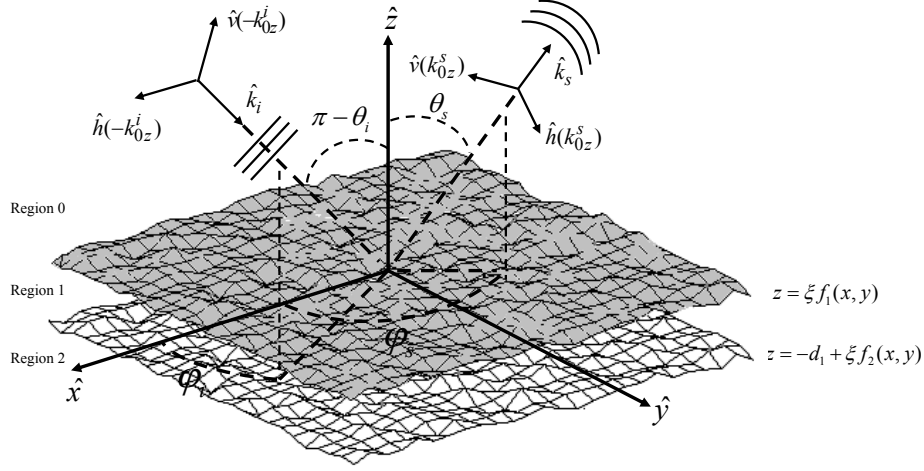
Figure 2.1: Geometry of the problem: a three-dimensional, two-layer isotropic dielectric structure with complex permittivities. The boundaries are zero-mean, stationary random processes with known, possibly dependent statistical properties. The first-layer thickness is d_1.

the surface heights are, requires an involved calculation that is out of the scope of this work.

2.2.2 Definitions

Assume the plane wave incident upon the structure is

$$\mathbf{E_i} = \mathbf{E_o} e^{i\mathbf{k_i} \cdot \mathbf{r}} \tag{2.1}$$

where $\mathbf{k_i} = k_x^i \hat{x} + k_y^i \hat{y} - k_{0z}^i \hat{z} = k_0 \hat{K}_0^i$, $\hat{K}_0^i$ is the incident direction, and k_0 is the wavenumber of the top layer (Region 0). Since $\mathbf{E_o} \cdot \mathbf{k_i} = 0$, the components of the incident electric field intensity can be decomposed into two perpendicular unit vectors in a plane perpendicular to the direction of propagation, i.e.,

$$\mathbf{E_o} = \mathbf{E_o} \cdot \hat{h}(-k_{0z}^i)\hat{h}(-k_{0z}^i) + \mathbf{E_o} \cdot \hat{v}(-k_{0z}^i)\hat{v}(-k_{0z}^i) \tag{2.2}$$

Due to the roughness of the interfaces, the scattered fields are no longer plane waves, but they can be expressed in spectral domain as the linear superposition of an infinite number of up- and down-going plane waves with coefficients to be found. Obviously, $\mathbf{E_2}$ has down-going

field components only. The electric field in each region can be written as

$$
\mathbf{E_0} = \int\limits_{-\infty}^{\infty}\int\limits_{-\infty}^{\infty} d\mathbf{k}_\perp \Big\{ \Big[A_h^+(\mathbf{k}_\perp)\hat{h}(k_{0z}) + A_v^+(\mathbf{k}_\perp)\hat{v}(k_{0z}) \Big] e^{ik_{0z}z}
$$
$$
+ \Big[A_h^-(\mathbf{k}_\perp)\hat{h}(-k_{0z}) + A_v^-(\mathbf{k}_\perp)\hat{v}(-k_{0z}) \Big] e^{-ik_{0z}z} \Big\} e^{i\mathbf{k}_\perp \cdot \mathbf{r}_\perp} \tag{2.3}
$$

$$
\mathbf{E_1} = \int\limits_{-\infty}^{\infty}\int\limits_{-\infty}^{\infty} d\mathbf{k}_\perp \Big\{ \Big[B_h^+(\mathbf{k}_\perp)\hat{h}(k_{1z}) + B_v^+(\mathbf{k}_\perp)\hat{v}(k_{1z}) \Big] e^{ik_{1z}z}
$$
$$
+ \Big[B_h^-(\mathbf{k}_\perp)\hat{h}(-k_{1z}) + B_v^-(\mathbf{k}_\perp)\hat{v}(-k_{1z}) \Big] e^{-ik_{1z}z} \Big\} e^{i\mathbf{k}_\perp \cdot \mathbf{r}_\perp} \tag{2.4}
$$

and

$$
\mathbf{E_2} = \int\limits_{-\infty}^{\infty}\int\limits_{-\infty}^{\infty} d\mathbf{k}_\perp \Big\{ \Big[C_h^-(\mathbf{k}_\perp)\hat{h}(-k_{2z}) + C_v^-(\mathbf{k}_\perp)\hat{v}(-k_{2z}) \Big] e^{-ik_{2z}z} \Big\} e^{i\mathbf{k}_\perp \cdot \mathbf{r}_\perp} \tag{2.5}
$$

where $\mathbf{k}_\perp = k_x\hat{x} + k_y\hat{y}$ and $d\mathbf{k}_\perp = dk_x dk_y$. Note that all integrals are in the form of inverse Fourier transforms and $\mathbf{k}_\perp$ is the Fourier transform variable. For definitions of $\hat{v}(\cdot)$ and $\hat{h}(\cdot)$, refer to Appendix A.1.

$A_h^-(\mathbf{k}_\perp)$ and $A_v^-(\mathbf{k}_\perp)$ are the known intensities of the incident electric field components and are given by

$$
A_h^-(\mathbf{k}_\perp) = \mathbf{E_o}\cdot \hat{h}(-k_{0z})\delta(\mathbf{k}_\perp - \mathbf{k}_\perp^{\mathbf{i}}) \tag{2.6}
$$

and

$$
A_v^-(\mathbf{k}_\perp) = \mathbf{E_o}\cdot \hat{v}(-k_{0z})\delta(\mathbf{k}_\perp - \mathbf{k}_\perp^{\mathbf{i}}) \tag{2.7}
$$

$A_{h,v}^+(\mathbf{k}_\perp)$, $B_{h,v}^\pm(\mathbf{k}_\perp)$, and $C_{h,v}^-(\mathbf{k}_\perp)$ are the unknown intensities of the scattered field components in different regions, and are to be determined. The superscripts '+' and '−' indicate whether the quantity corresponds to an up-going or a down-going plane wave. Once $A_{h,v}^+(\mathbf{k}_\perp)$ are known, from (2.3) the scattered field is known everywhere in the region of incidence. Subsequently, $B_{h,v}^\pm(\mathbf{k}_\perp)$ and $C_{h,v}^-(\mathbf{k}_\perp)$ can be calculated leading to the fields in all regions.

2.3   Analysis

The outline of the analysis is as follows: First, the fields are represented in spectral domain, as in (2.3)–(2.5), and the unknown coefficients are represented by their asymptotic expansions in ξ. The integrands are then expanded in ξ and the boundary conditions are applied afterward. The terms in the resulting equations are matched up to the first order. This matching will result in two systems of linear equations. Solving for the unknowns will lead to finding the bistatic scattering coefficients. Now, each step will be described in more detail.

To determine the unknown coefficients introduced in Section 2.2.2, SPM is applied. This method suggests that the unknown coefficients, i.e., $A_{h,v}^{+}(\mathbf{k}_\perp)$, $B_{h,v}^{\pm}(\mathbf{k}_\perp)$, and $C_{h,v}^{-}(\mathbf{k}_\perp)$, be represented by their asymptotic expansions in ξ with new unknown coefficients $a_{h,v}^{+(m)}(\mathbf{k}_\perp)$, $b_{h,v}^{\pm(m)}(\mathbf{k}_\perp)$, and $c_{h,v}^{-(m)}(\mathbf{k}_\perp)$, where the superscript (m) represents the order of the coefficients and should not be mistaken for the mth power.

$$A_{h,v}^{+}(\mathbf{k}_\perp) \sim \sum_{m=0}^{\infty} \frac{a_{h,v}^{+(m)}(\mathbf{k}_\perp)}{m!} \xi^m \tag{2.8}$$

$$B_{h,v}^{\pm}(\mathbf{k}_\perp) \sim \sum_{m=0}^{\infty} \frac{b_{h,v}^{\pm(m)}(\mathbf{k}_\perp)}{m!} \xi^m \tag{2.9}$$

$$C_{h,v}^{-}(\mathbf{k}_\perp) \sim \sum_{m=0}^{\infty} \frac{c_{h,v}^{-(m)}(\mathbf{k}_\perp)}{m!} \xi^m \tag{2.10}$$

as $\xi \to 0$.

2.3.1   Boundary-Condition Equations

To find the unknowns, the boundary conditions, which enforce the continuity of the tangential components of electric and magnetic fields at the boundaries, should be applied.

$$\hat{n}_1 \times \mathbf{E_0} = \hat{n}_1 \times \mathbf{E_1}\Big|_{z=\xi f_1(x,y)} \tag{2.11}$$

$$\hat{n}_1 \times \mathbf{H_0} = \hat{n}_1 \times \mathbf{H_1}\Big|_{z=\xi f_1(x,y)} \tag{2.12}$$

$$\hat{n}_2 \times \mathbf{E_1} = \hat{n}_2 \times \mathbf{E_2}\Big|_{z=-d_1+\xi f_2(x,y)} \tag{2.13}$$

$$\hat{n}_2 \times \mathbf{H_1} = \hat{n}_2 \times \mathbf{H_2}\Big|_{z=-d_1+\xi f_2(x,y)} \tag{2.14}$$

where $\hat{n}_1$ and $\hat{n}_2$ are vectors normal to the boundaries, and their expansions are presented in Appendix A.1. By virtue of imposing the boundary conditions simultaneously, all interactions between the rough boundaries are included in the solution. Note that the magnetic field in each region is easily determined from the relation $\mathbf{H_n^+} = \hat{k}_n \times \mathbf{E_n^+}/Z_n$ and $\mathbf{H_n^-} = \hat{K}_n \times \mathbf{E_n^-}/Z_n$, where $Z_n = \sqrt{\mu_0/\epsilon_n}$. The vectors $\hat{k}_n$ and $\hat{K}_n$ are defined in Appendix A.1. Noting that $(\hat{v}(\cdot), \hat{h}(\cdot), \hat{k})$ and $(\hat{v}(\cdot), \hat{h}(\cdot), \hat{K})$ are orthonormal systems, the magnetic field will be

$$\mathbf{H_0} = \frac{1}{Z_0} \int\limits_{-\infty}^{\infty}\int\limits_{-\infty}^{\infty} \mathrm{d}\mathbf{k}_\perp \bigg\{ \Big[-A_h^+(\mathbf{k}_\perp)\hat{v}(k_{0z}) + A_v^+(\mathbf{k}_\perp)\hat{h}(k_{0z}) \Big] e^{ik_{0z}z}$$
$$+ \Big[-A_h^-(\mathbf{k}_\perp)\hat{v}(-k_{0z}) + A_v^-(\mathbf{k}_\perp)\hat{h}(-k_{0z}) \Big] e^{-ik_{0z}z} \bigg\} e^{i\mathbf{k}_\perp \cdot \mathbf{r}_\perp} \tag{2.15}$$

$$\mathbf{H_1} = \frac{1}{Z_1} \int\limits_{-\infty}^{\infty}\int\limits_{-\infty}^{\infty} \mathrm{d}\mathbf{k}_\perp \bigg\{ \Big[-B_h^+(\mathbf{k}_\perp)\hat{v}(k_{1z}) + B_v^+(\mathbf{k}_\perp)\hat{h}(k_{1z}) \Big] e^{ik_{1z}z}$$
$$+ \Big[-B_h^-(\mathbf{k}_\perp)\hat{v}(-k_{1z}) + B_v^-(\mathbf{k}_\perp)\hat{h}(-k_{1z}) \Big] e^{-ik_{1z}z} \bigg\} e^{i\mathbf{k}_\perp \cdot \mathbf{r}_\perp} \tag{2.16}$$

and

$$\mathbf{H_2} = \frac{1}{Z_2} \int\limits_{-\infty}^{\infty}\int\limits_{-\infty}^{\infty} \mathrm{d}\mathbf{k}_\perp \bigg\{ \Big[-C_h^-(\mathbf{k}_\perp)\hat{v}(-k_{2z}) + C_v^-(\mathbf{k}_\perp)\hat{h}(-k_{2z}) \Big] e^{-ik_{2z}z} \bigg\} e^{i\mathbf{k}_\perp \cdot \mathbf{r}_\perp} \tag{2.17}$$

Applying the boundary conditions and using the expansions presented in Appendix A.1 will result in four equations. The boundary condition equations at the first boundary are as

follows.

$$\sum_{m=0}^{\infty}\sum_{n=0}^{m}\int_{-\infty}^{\infty}\int_{-\infty}^{\infty}d\mathbf{k}_\perp \frac{\left(\mathcal{A}(\mathbf{k}_\perp)a_h^{+(n)}+\mathcal{B}(k_{0z},f_1)a_v^{+(n)}\right)}{n!}\frac{(ik_{0z}f_1(x,y))^{m-n}}{(m-n)!}e^{i\mathbf{k}_\perp\cdot\mathbf{r}_\perp}\xi^m+$$

$$\left(\mathcal{A}(\mathbf{k^i}_\perp)E_o^h+\mathcal{B}(-k_{0z}^i,f_1)E_o^v\right)e^{i\mathbf{k^i}_\perp\cdot\mathbf{r}_\perp}\sum_{m=0}^{\infty}\frac{(-ik_{0z}^if_1(x,y))^m}{m!}\xi^m=$$

$$\sum_{m=0}^{\infty}\sum_{n=0}^{m}\int_{-\infty}^{\infty}\int_{-\infty}^{\infty}d\mathbf{k}_\perp\frac{\left(\mathcal{A}(\mathbf{k}_\perp)b_h^{+(n)}+\mathcal{B}(k_{1z},f_1)b_v^{+(n)}\right)}{n!}\frac{(ik_{1z}f_1(x,y))^{m-n}}{(m-n)!}e^{i\mathbf{k}_\perp\cdot\mathbf{r}_\perp}\xi^m+$$

$$\sum_{m=0}^{\infty}\sum_{n=0}^{m}\int_{-\infty}^{\infty}\int_{-\infty}^{\infty}d\mathbf{k}_\perp\frac{\left(\mathcal{A}(\mathbf{k}_\perp)b_h^{-(n)}+\mathcal{B}(-k_{1z},f_1)b_v^{-(n)}\right)}{n!}\frac{(-ik_{1z}f_1(x,y))^{m-n}}{(m-n)!}e^{i\mathbf{k}_\perp\cdot\mathbf{r}_\perp}\xi^m \quad (2.18)$$

$$\frac{1}{Z_0}\sum_{m=0}^{\infty}\sum_{n=0}^{m}\int_{-\infty}^{\infty}\int_{-\infty}^{\infty}d\mathbf{k}_\perp\frac{\left(-\mathcal{B}(k_{0z},f_1)a_h^{+(n)}+\mathcal{A}(\mathbf{k}_\perp)a_v^{+(n)}\right)}{n!}\frac{(ik_{0z}f_1(x,y))^{m-n}}{(m-n)!}e^{i\mathbf{k}_\perp\cdot\mathbf{r}_\perp}\xi^m+$$

$$\frac{1}{Z_0}\left(-\mathcal{B}(-k_{0z}^i,f_1)E_o^h+\mathcal{A}(\mathbf{k^i}_\perp)E_o^v\right)e^{i\mathbf{k^i}_\perp\cdot\mathbf{r}_\perp}\sum_{m=0}^{\infty}\frac{(-ik_{0z}^if_1(x,y))^m}{m!}\xi^m=$$

$$\frac{1}{Z_1}\sum_{m=0}^{\infty}\sum_{n=0}^{m}\int_{-\infty}^{\infty}\int_{-\infty}^{\infty}d\mathbf{k}_\perp\frac{\left(-\mathcal{B}(k_{1z},f_1)b_h^{+(n)}+\mathcal{A}(\mathbf{k}_\perp)b_v^{+(n)}\right)}{n!}\frac{(ik_{1z}f_1(x,y))^{m-n}}{(m-n)!}e^{i\mathbf{k}_\perp\cdot\mathbf{r}_\perp}\xi^m+$$

$$\frac{1}{Z_1}\sum_{m=0}^{\infty}\sum_{n=0}^{m}\int_{-\infty}^{\infty}\int_{-\infty}^{\infty}d\mathbf{k}_\perp\frac{\left(-\mathcal{B}(-k_{1z},f_1)b_h^{-(n)}+\mathcal{A}(\mathbf{k}_\perp)b_v^{-(n)}\right)}{n!}\frac{(-ik_{1z}f_1(x,y))^{m-n}}{(m-n)!}e^{i\mathbf{k}_\perp\cdot\mathbf{r}_\perp}\xi^m \quad (2.19)$$

The boundary condition equations at the second boundary are as follows.

$$\sum_{m=0}^{\infty}\sum_{n=0}^{m}\int_{-\infty}^{\infty}\int_{-\infty}^{\infty}d\mathbf{k}_\perp\frac{\left(\mathcal{A}(\mathbf{k}_\perp)b_h^{+(n)}+\mathcal{B}(k_{1z},f_2)b_v^{+(n)}\right)}{n!}\frac{(ik_{1z}f_2(x,y))^{m-n}}{(m-n)!}e^{i\mathbf{k}_\perp\cdot\mathbf{r}_\perp-ik_{1z}d_1}\xi^m+$$

$$\sum_{m=0}^{\infty}\sum_{n=0}^{m}\int_{-\infty}^{\infty}\int_{-\infty}^{\infty}d\mathbf{k}_\perp\frac{\left(\mathcal{A}(\mathbf{k}_\perp)b_h^{-(n)}+\mathcal{B}(-k_{1z},f_2)b_v^{-(n)}\right)}{n!}\frac{(-ik_{1z}f_2(x,y))^{m-n}}{(m-n)!}e^{i\mathbf{k}_\perp\cdot\mathbf{r}_\perp+ik_{1z}d_1}\xi^m=$$

$$\sum_{m=0}^{\infty}\sum_{n=0}^{m}\int_{-\infty}^{\infty}\int_{-\infty}^{\infty}d\mathbf{k}_\perp\frac{\left(\mathcal{A}(\mathbf{k}_\perp)c_h^{-(n)}+\mathcal{B}(-k_{2z},f_2)c_v^{-(n)}\right)}{n!}\frac{(-ik_{2z}f_2(x,y))^{m-n}}{(m-n)!}e^{i\mathbf{k}_\perp\cdot\mathbf{r}_\perp+ik_{2z}d_1}\xi^m \quad (2.20)$$

$$\frac{1}{Z_1}\sum_{m=0}^{\infty}\sum_{n=0}^{m}\int_{-\infty}^{\infty}\int_{-\infty}^{\infty}d\mathbf{k}_\perp\frac{\left(-\mathcal{B}(k_{1z},f_2)b_h^{+(n)}+\mathcal{A}(\mathbf{k}_\perp)b_v^{+(n)}\right)}{n!}\frac{(ik_{1z}f_2(x,y))^{m-n}}{(m-n)!}e^{i\mathbf{k}_\perp\cdot\mathbf{r}_\perp-ik_{1z}d_1}\xi^m+$$

$$\frac{1}{Z_1}\sum_{m=0}^{\infty}\sum_{n=0}^{m}\int_{-\infty}^{\infty}\int_{-\infty}^{\infty}d\mathbf{k}_\perp\frac{\left(-\mathcal{B}(-k_{1z},f_2)b_h^{-(n)}+\mathcal{A}(\mathbf{k}_\perp)b_v^{-(n)}\right)}{n!}\frac{(-ik_{1z}f_2(x,y))^{m-n}}{(m-n)!}e^{i\mathbf{k}_\perp\cdot\mathbf{r}_\perp+ik_{1z}d_1}\xi^m=$$

$$\frac{1}{Z_2}\sum_{m=0}^{\infty}\sum_{n=0}^{m}\int_{-\infty}^{\infty}\int_{-\infty}^{\infty}d\mathbf{k}_\perp\frac{\left(-\mathcal{B}(-k_{2z},f_2)c_h^{-(n)}+\mathcal{A}(\mathbf{k}_\perp)c_v^{-(n)}\right)}{n!}\frac{(-ik_{2z}f_2(x,y))^{m-n}}{(m-n)!}e^{i\mathbf{k}_\perp\cdot\mathbf{r}_\perp+ik_{2z}d_1}\xi^m \quad (2.21)$$

where

$$\mathcal{A}(\mathbf{k}_\perp):=\frac{k_x\hat{x}+k_y\hat{y}}{k_\rho} \quad (2.22)$$

17

$$\mathcal{B}(k_{nz}, f_i) := \frac{(-\xi f_{iy}k_\rho{}^2 + k_{nz}k_y)\hat{x} + (\xi f_{ix}k_\rho{}^2 - k_{nz}k_x)\hat{y}}{k_n k_\rho} \tag{2.23}$$

We can then match the $\hat{x}$ and $\hat{y}$ components of each of these equations separately to a specific order to derive, for each order, a system of eight linear equations with $a_{h,v}^{+(m)}(\mathbf{k}_\perp)$, $b_{h,v}^{\pm(m)}(\mathbf{k}_\perp)$, and $c_{h,v}^{-(m)}(\mathbf{k}_\perp)$ being the unknowns.

2.3.2 Zeroth-Order Solution

Matching the $\hat{x}$ components of (2.18) to the zeroth order results in

$$\int_{-\infty}^{\infty}\int_{-\infty}^{\infty} d\mathbf{k}_\perp \left(\frac{k_x}{k_\rho}a_h^{+(0)} + \frac{k_{0z}k_y}{k_0 k_\rho}a_v^{+(0)} \right) e^{i\mathbf{k}_\perp \cdot \mathbf{r}_\perp} + \left(\frac{k_x^i}{k_\rho^i}E_o^h - \frac{k_y^i k_{0z}^i}{k_0 k_\rho^i}E_o^v \right) e^{i\mathbf{k}_\perp^i \cdot \mathbf{r}_\perp} =$$
$$\int_{-\infty}^{\infty}\int_{-\infty}^{\infty} d\mathbf{k}_\perp \left(\frac{k_x}{k_\rho}b_h^{+(0)} + \frac{k_{1z}k_y}{k_1 k_\rho}b_v^{+(0)} \right) e^{i\mathbf{k}_\perp \cdot \mathbf{r}_\perp} + \int_{-\infty}^{\infty}\int_{-\infty}^{\infty} d\mathbf{k}_\perp \left(\frac{k_x}{k_\rho}b_h^{-(0)} - \frac{k_{1z}k_y}{k_1 k_\rho}b_v^{-(0)} \right) e^{i\mathbf{k}_\perp \cdot \mathbf{r}_\perp}$$
$$\tag{2.24}$$

As stated before, these integrals are in the form of inverse Fourier transform. We know that if $F(\mathbf{k}_\perp)$ is the Fourier transform of $f(x,y)$, then $F(\mathbf{k}_\perp - \mathbf{k}_\perp^i)$ will be the Fourier transform of $f(x,y)e^{i\mathbf{k}_\perp^i \cdot \mathbf{r}_\perp}$. Also the Fourier transform of $f(x,y) = 1$ is $\delta(\mathbf{k}_\perp)$. Therefore, (2.24) can be rewritten as

$$\frac{k_x}{k_\rho}a_h^{+(0)} + \frac{k_{0z}k_y}{k_0 k_\rho}a_v^{+(0)} - \frac{k_x}{k_\rho}b_h^{+(0)} - \frac{k_{1z}k_y}{k_1 k_\rho}b_v^{+(0)} - \frac{k_x}{k_\rho}b_h^{-(0)} + \frac{k_{1z}k_y}{k_1 k_\rho}b_v^{-(0)}$$
$$= -\left(\frac{k_x}{k_\rho}E_o^h - \frac{k_y k_{0z}}{k_0 k_\rho}E_o^v \right) \delta(\mathbf{k}_\perp - \mathbf{k}_\perp^i) \tag{2.25}$$

The other seven zeroth-order equations are

$$\frac{k_y}{k_\rho}a_h^{+(0)} - \frac{k_{0z}k_x}{k_0 k_\rho}a_v^{+(0)} - \frac{k_y}{k_\rho}b_h^{+(0)} + \frac{k_{1z}k_x}{k_1 k_\rho}b_v^{+(0)} - \frac{k_y}{k_\rho}b_h^{-(0)} - \frac{k_{1z}k_x}{k_1 k_\rho}b_v^{-(0)} =$$
$$-\left(\frac{k_y}{k_\rho}E_o^h + \frac{k_x k_{0z}}{k_0 k_\rho}E_o^v \right) \delta(\mathbf{k}_\perp - \mathbf{k}_\perp^i) \quad (2.26)$$

$$-\frac{1}{Z_0}\frac{k_{0z}k_y}{k_0 k_\rho}a_h^{+(0)} + \frac{1}{Z_0}\frac{k_x}{k_\rho}a_v^{+(0)} + \frac{1}{Z_1}\frac{k_{1z}k_y}{k_1 k_\rho}b_h^{+(0)}$$
$$-\frac{1}{Z_1}\frac{k_x}{k_\rho}b_v^{+(0)} - \frac{1}{Z_1}\frac{k_{1z}k_y}{k_1 k_\rho}b_h^{-(0)} - \frac{1}{Z_1}\frac{k_x}{k_\rho}b_v^{-(0)} =$$
$$-\frac{1}{Z_0}\left(\frac{k_{0z}k_y}{k_0 k_\rho}E_o^h + \frac{k_x}{k_\rho}E_o^v\right)\delta(\mathbf{k}_\perp - \mathbf{k}_\perp^{\mathbf{i}}) \quad (2.27)$$

$$\frac{1}{Z_0}\frac{k_{0z}k_x}{k_0 k_\rho}a_h^{+(0)} + \frac{1}{Z_0}\frac{k_y}{k_\rho}a_v^{+(0)} - \frac{1}{Z_1}\frac{k_{1z}k_x}{k_1 k_\rho}b_h^{+(0)}$$
$$-\frac{1}{Z_1}\frac{k_y}{k_\rho}b_v^{+(0)} + \frac{1}{Z_1}\frac{k_{1z}k_x}{k_1 k_\rho}b_h^{-(0)} - \frac{1}{Z_1}\frac{k_y}{k_\rho}b_v^{-(0)} =$$
$$\frac{1}{Z_0}\left(\frac{k_{0z}k_x}{k_0 k_\rho}E_o^h - \frac{k_y}{k_\rho}E_o^v\right)\delta(\mathbf{k}_\perp - \mathbf{k}_\perp^{\mathbf{i}}) \quad (2.28)$$

$$\left(\frac{k_x}{k_\rho}b_h^{+(0)} + \frac{k_{1z}k_y}{k_1 k_\rho}b_v^{+(0)}\right)e^{-ik_{1z}d_1} + \left(\frac{k_x}{k_\rho}b_h^{-(0)} - \frac{k_{1z}k_y}{k_1 k_\rho}b_v^{-(0)}\right)e^{ik_{1z}d_1}$$
$$-\left(\frac{k_x}{k_\rho}c_h^{-(0)} - \frac{k_{2z}k_y}{k_2 k_\rho}c_v^{-(0)}\right)e^{ik_{2z}d_1} = 0 \quad (2.29)$$

$$\left(\frac{k_y}{k_\rho}b_h^{+(0)} - \frac{k_{1z}k_x}{k_1 k_\rho}b_v^{+(0)}\right)e^{-ik_{1z}d_1} + \left(\frac{k_y}{k_\rho}b_h^{-(0)} + \frac{k_{1z}k_x}{k_1 k_\rho}b_v^{-(0)}\right)e^{ik_{1z}d_1}$$
$$-\left(\frac{k_y}{k_\rho}c_h^{-(0)} + \frac{k_{2z}k_y}{k_2 k_\rho}c_v^{-(0)}\right)e^{ik_{2z}d_1} = 0 \quad (2.30)$$

$$\frac{1}{Z_1}\left(-\frac{k_{1z}k_y}{k_1 k_\rho}b_h^{+(0)} + \frac{k_x}{k_\rho}b_v^{+(0)}\right)e^{-ik_{1z}d_1} + \frac{1}{Z_1}\left(\frac{k_{1z}k_y}{k_1 k_\rho}b_h^{-(0)} + \frac{k_x}{k_\rho}b_v^{-(0)}\right)e^{ik_{1z}d_1}$$
$$-\frac{1}{Z_2}\left(\frac{k_{2z}k_y}{k_2 k_\rho}c_h^{-(0)} + \frac{k_x}{k_\rho}c_v^{-(0)}\right)e^{ik_{2z}d_1} = 0 \quad (2.31)$$

and

$$\frac{1}{Z_1}\left(\frac{k_{1z}k_x}{k_1 k_\rho}b_h^{+(0)} + \frac{k_y}{k_\rho}b_v^{+(0)}\right)e^{-ik_{1z}d_1} + \frac{1}{Z_1}\left(-\frac{k_{1z}k_x}{k_1 k_\rho}b_h^{-(0)} + \frac{k_y}{k_\rho}b_v^{-(0)}\right)e^{ik_{1z}d_1}$$
$$-\frac{1}{Z_2}\left(-\frac{k_{2z}k_x}{k_2 k_\rho}c_h^{-(0)} + \frac{k_y}{k_\rho}c_v^{-(0)}\right)e^{ik_{2z}d_1} = 0 \quad (2.32)$$

This system of eight linear equations with the eight zeroth-order $(m = 0)$ unknowns can be represented as

$$[\mathbf{A}(\mathbf{k}_\perp)]_{8\times8} \cdot [\mathbf{x_0}(\mathbf{k}_\perp)]_{8\times1} = [\mathbf{b_0}(\mathbf{k}_\perp)]_{8\times1} \tag{2.33}$$

where $\mathbf{x_0}(\mathbf{k}_\perp) = [a_h^{+(0)} \ \ a_v^{+(0)} \ \ b_h^{+(0)} \ \ b_v^{+(0)} \ \ b_h^{-(0)} \ \ b_v^{-(0)} \ \ c_h^{-(0)} \ \ c_v^{-(0)}]^T$.

After solving this system of linear equations, the zeroth-order coefficients are found to be

$$a_h^{+(0)}(\mathbf{k}_\perp) = \frac{(k_{1z} + k_{2z})(k_{1z} - k_{0z}) - e^{i2k_{1z}d_1}(k_{1z} - k_{2z})(k_{1z} + k_{0z})}{e^{i2k_{1z}d_1}(k_{1z} - k_{2z})(k_{1z} - k_{0z}) - (k_{1z} + k_{2z})(k_{1z} + k_{0z})} E_o^h \delta(\mathbf{k}_\perp - \mathbf{k}_\perp^i) \tag{2.34}$$

$$a_v^{+(0)}(\mathbf{k}_\perp) = \frac{1 + e^{i2k_{1z}d_1}(1 - 2k_{2z}k_1^2/(k_{1z}k_2^2 + k_{2z}k_1^2)) - 2k_{1z}k_0^2/(k_{1z}k_0^2 + k_{0z}k_1^2)}{1 + e^{i2k_{1z}d_1}(1 - 2k_{2z}k_1^2/(k_{1z}k_2^2 + k_{2z}k_1^2))(1 - 2k_{1z}k_0^2/(k_{1z}k_0^2 + k_{0z}k_1^2))} E_o^v \delta(\mathbf{k}_\perp - \mathbf{k}_\perp^i) \tag{2.35}$$

$$b_h^{+(0)}(\mathbf{k}_\perp) = \frac{-2e^{i2k_{1z}d_1}(k_{1z} - k_{2z})k_{0z}}{e^{i2k_{1z}d_1}(k_{1z} - k_{2z})(k_{1z} - k_{0z}) - (k_{1z} + k_{2z})(k_{1z} + k_{0z})} E_o^h \delta(\mathbf{k}_\perp - \mathbf{k}_\perp^i) \tag{2.36}$$

$$b_v^{+(0)}(\mathbf{k}_\perp) = \frac{-2e^{i2k_{1z}d_1}k_0 k_1(-k_{1z}k_2^2 + k_{2z}k_1^2)k_{0z}}{-e^{i2k_{1z}d_1}(k_{1z}k_2^2 - k_{2z}k_1^2)(k_{1z}k_0^2 - k_{0z}k_1^2) + (k_{1z}k_2^2 + k_{2z}k_1^2)(k_{1z}k_0^2 + k_{0z}k_1^2)} E_o^v \delta(\mathbf{k}_\perp - \mathbf{k}_\perp^i) \tag{2.37}$$

$$b_h^{-(0)}(\mathbf{k}_\perp) = \frac{-2(k_{1z} + k_{2z})k_{0z}}{e^{i2k_{1z}d_1}(k_{1z} - k_{2z})(k_{1z} - k_{0z}) - (k_{1z} + k_{2z})(k_{1z} + k_{0z})} E_o^h \delta(\mathbf{k}_\perp - \mathbf{k}_\perp^i) \tag{2.38}$$

$$b_v^{-(0)}(\mathbf{k}_\perp) = \frac{2k_0 k_1(k_{1z}k_2^2 + k_{2z}k_1^2)k_{0z}}{-e^{i2k_{1z}d_1}(k_{1z}k_2^2 - k_{2z}k_1^2)(k_{1z}k_0^2 - k_{0z}k_1^2) + (k_{1z}k_2^2 + k_{2z}k_1^2)(k_{1z}k_0^2 + k_{0z}k_1^2)} E_o^v \delta(\mathbf{k}_\perp - \mathbf{k}_\perp^i) \tag{2.39}$$

$$c_h^{-(0)}(\mathbf{k}_\perp) = \frac{-4e^{i(k_{1z} - k_{2z})d_1}k_{1z}k_{0z}}{e^{i2k_{1z}d_1}(k_{1z} - k_{2z})(k_{1z} - k_{0z}) - (k_{1z} + k_{2z})(k_{1z} + k_{0z})} E_o^h \delta(\mathbf{k}_\perp - \mathbf{k}_\perp^i) \tag{2.40}$$

and

$$c_v^{-(0)}(\mathbf{k}_\perp) = \frac{-4e^{i(k_{1z} - k_{2z})d_1}k_0 k_1^2 k_2 k_{1z}k_{0z}}{e^{i2k_{1z}d_1}(k_{1z}k_2^2 - k_{2z}k_1^2)(k_{1z}k_0^2 - k_{0z}k_1^2) - (k_{1z}k_2^2 + k_{2z}k_1^2)(k_{1z}k_0^2 + k_{0z}k_1^2)} E_o^v \delta(\mathbf{k}_\perp - \mathbf{k}_\perp^i) \tag{2.41}$$

Analytical validation of the zeroth-order solution is presented in Appendix A.2.

2.3.3 First-Order Solution

Now, the terms in (2.18)–(2.21) can be matched to the first order. Matching the $\hat{x}$ components of (2.18) to the first order will result in

$$\int\limits_{-\infty}^{\infty}\int\limits_{-\infty}^{\infty} d\mathbf{k}_\perp \left[\frac{-f_{1y}k_\rho}{k_0} a_v^{+(0)} + \left(\frac{k_x}{k_\rho} a_h^{+(0)} + \frac{k_{0z}k_y}{k_0 k_\rho} a_v^{+(0)} \right) (ik_{0z}f_1(x,y)) + \frac{k_x}{k_\rho} a_h^{+(1)} + \frac{k_{0z}k_y}{k_0 k_\rho} a_v^{+(1)} \right] e^{i\mathbf{k}_\perp \cdot \mathbf{r}_\perp}$$

$$+ \left[-\frac{f_{1y}k_\rho^i}{k_0} E_o^v + \left(\frac{k_x^i}{k_\rho^i} E_o^h - \frac{k_{0z}^i k_y^i}{k_0 k_\rho^i} E_o^v \right) (-ik_{0z}^i f_1(x,y)) \right] e^{i\mathbf{k}_\perp^i \cdot \mathbf{r}_\perp} =$$

$$\int\limits_{-\infty}^{\infty}\int\limits_{-\infty}^{\infty} d\mathbf{k}_\perp \left[\frac{-f_{1y}k_\rho}{k_1} b_v^{+(0)} + \left(\frac{k_x}{k_\rho} b_h^{+(0)} + \frac{k_{1z}k_y}{k_1 k_\rho} b_v^{+(0)} \right) (ik_{1z}f_1(x,y)) + \frac{k_x}{k_\rho} b_h^{+(1)} + \frac{k_{1z}k_y}{k_1 k_\rho} b_v^{+(1)} \right] e^{i\mathbf{k}_\perp \cdot \mathbf{r}_\perp}$$

$$+ \int\limits_{-\infty}^{\infty}\int\limits_{-\infty}^{\infty} d\mathbf{k}_\perp \left[\frac{-f_{1y}k_\rho}{k_1} b_v^{-(0)} + \left(\frac{k_x}{k_\rho} b_h^{-(0)} - \frac{k_{1z}k_y}{k_1 k_\rho} b_v^{-(0)} \right) (-ik_{1z}f_1(x,y)) + \frac{k_x}{k_\rho} b_h^{-(1)} - \frac{k_{1z}k_y}{k_1 k_\rho} b_v^{-(1)} \right] e^{i\mathbf{k}_\perp \cdot \mathbf{r}_\perp} \quad (2.42)$$

Since the zeroth-order coefficients are linearly proportional to $\delta(\mathbf{k}_\perp - \mathbf{k}_\perp^i)$, parts of the integrals above can be evaluated before applying the Fourier transform on both sides. For example,

$$\int\limits_{-\infty}^{\infty}\int\limits_{-\infty}^{\infty} d\mathbf{k}_\perp \frac{-f_y k_\rho}{k_0} a_v^{+(0)}(\mathbf{k}_\perp) = \frac{-f_y k_\rho^i}{k_0} a_{v/\delta}^{+(0)}(\mathbf{k}_\perp^i) \quad (2.43)$$

where $a_{v/\delta}^{+(0)}(\mathbf{k}_\perp^i)$ means $a_v^{+(0)}(\mathbf{k}_\perp)$ given in (2.35) evaluated at $\mathbf{k}_\perp = \mathbf{k}_\perp^i$ with $\delta(\mathbf{k}_\perp - \mathbf{k}_\perp^i)$ suppressed. For ease of notation, from now on, $a_v^{+(0)}$ is used instead. Noting that the Fourier transform of $\partial f(x,y)/\partial y$ is $k_y F(\mathbf{k}_\perp)$, the following equation will result.

$$\frac{k_x}{k_\rho} a_h^{+(1)} + \frac{k_{0z}k_y}{k_0 k_\rho} a_v^{+(1)} - \frac{k_x}{k_\rho} b_h^{+(1)} - \frac{k_{1z}k_y}{k_1 k_\rho} b_v^{+(1)} - \frac{k_x}{k_\rho} b_h^{-(1)} + \frac{k_{1z}k_y}{k_1 k_\rho} b_v^{-(1)} =$$

$$\left[\left(-\frac{(k_{0z}^i)^2 k_y^i}{k_0 k_\rho^i} + \frac{(k_y - k_y^i)k_\rho^i}{k_0} \right) a_v^{+(0)} - \frac{k_{0z}^i k_x^i}{k_\rho^i} a_h^{+(0)} - \left(\frac{(k_y - k_y^i)k_\rho^i}{k_1} - \frac{(k_{1z}^i)^2 k_y^i}{k_1 k_\rho^i} \right) b_v^{+(0)} + \right.$$

$$\frac{k_{1z}^i k_x^i}{k_\rho^i} b_h^{+(0)} - \left(\frac{(k_y - k_y^i)k_\rho^i}{k_1} - \frac{(k_{1z}^i)^2 k_y^i}{k_1 k_\rho^i} \right) b_v^{-(0)} - \frac{k_{1z}^i k_x^i}{k_\rho^i} b_h^{-(0)} -$$

$$\left. \left(\frac{(k_{0z}^i)^2 k_y^i}{k_0 k_\rho^i} - \frac{(k_y - k_y^i)k_\rho^i}{k_0} \right) E_o^v + \frac{k_{0z}^i k_x^i}{k_\rho^i} E_o^h \right] (iF_1(\mathbf{k}_\perp - \mathbf{k}_\perp^i)) \quad (2.44)$$

The other seven first-order equations are

$$\frac{k_y}{k_\rho}a_h^{+(1)} - \frac{k_{0z}k_x}{k_0 k_\rho}a_v^{+(1)} - \frac{k_y}{k_\rho}b_h^{+(1)} + \frac{k_{1z}k_x}{k_1 k_\rho}b_v^{+(1)} - \frac{k_y}{k_\rho}b_h^{-(1)} - \frac{k_{1z}k_x}{k_1 k_\rho}b_v^{-(1)} =$$

$$\left[\left(\frac{(k_{0z}^i)^2 k_x^i}{k_0 k_\rho^i} - \frac{(k_x - k_x^i)k_\rho^i}{k_0} \right) a_v^{+(0)} - \frac{k_{0z}^i k_y^i}{k_\rho^i} a_h^{+(0)} + \left(\frac{(k_x - k_x^i)k_\rho^i}{k_1} - \frac{(k_{1z}^i)^2 k_x^i}{k_1 k_\rho^i} \right) b_v^{+(0)} \right.$$

$$+ \frac{k_{1z}^i k_y^i}{k_\rho^i} b_h^{+(0)} + \left(\frac{(k_x - k_x^i)k_\rho^i}{k_1} - \frac{(k_{1z}^i)^2 k_x^i}{k_1 k_\rho^i} \right) b_v^{-(0)} - \frac{k_{1z}^i k_y^i}{k_\rho^i} b_h^{-(0)}$$

$$\left. + \left(\frac{(k_{0z}^i)^2 k_x^i}{k_0 k_\rho^i} - \frac{(k_x - k_x^i)k_\rho^i}{k_0} \right) E_o^v + \frac{k_{0z}^i k_y^i}{k_\rho^i} E_o^h \right] \left(iF_1(\mathbf{k}_\perp - \mathbf{k}_\perp^i) \right) \quad (2.45)$$

$$-\frac{1}{Z_0}\frac{k_{0z}k_y}{k_0 k_\rho}a_h^{+(1)} + \frac{1}{Z_0}\frac{k_x}{k_\rho}a_v^{+(1)} + \frac{1}{Z_1}\frac{k_{1z}k_y}{k_1 k_\rho}b_h^{+(1)} - \frac{1}{Z_1}\frac{k_x}{k_\rho}b_v^{+(1)} - \frac{1}{Z_1}\frac{k_{1z}k_y}{k_1 k_\rho}b_h^{-(1)} - \frac{1}{Z_1}\frac{k_x}{k_\rho}b_v^{-(1)}$$

$$= \left[\frac{1}{Z_0} \left(\frac{(k_{0z}^i)^2 k_y^i}{k_0 k_\rho^i} - \frac{(k_y - k_y^i)k_\rho^i}{k_0} \right) a_h^{+(0)} - \frac{1}{Z_0}\frac{k_{0z}^i k_x^i}{k_\rho^i} a_v^{+(0)} + \frac{1}{Z_1} \left(\frac{(k_y - k_y^i)k_\rho^i}{k_1} - \frac{(k_{1z}^i)^2 k_y^i}{k_1 k_\rho^i} \right) b_h^{+(0)} \right.$$

$$+ \frac{1}{Z_1}\frac{k_{1z}^i k_x^i}{k_\rho^i} b_v^{+(0)} + \frac{1}{Z_1} \left(\frac{(k_y - k_y^i)k_\rho^i}{k_1} - \frac{(k_{1z}^i)^2 k_y^i}{k_1 k_\rho^i} \right) b_h^{-(0)} - \frac{1}{Z_1}\frac{k_{1z}^i k_x^i}{k_\rho^i} b_v^{-(0)}$$

$$\left. + \frac{1}{Z_0} \left(\frac{(k_{0z}^i)^2 k_y^i}{k_0 k_\rho^i} - \frac{(k_y - k_y^i)k_\rho^i}{k_0} \right) E_o^h + \frac{1}{Z_0}\frac{k_{0z}^i k_x^i}{k_\rho^i} E_o^v \right] \left(iF_1(\mathbf{k}_\perp - \mathbf{k}_\perp^i) \right) \quad (2.46)$$

$$\frac{1}{Z_0}\frac{k_{0z}k_x}{k_0 k_\rho}a_h^{+(1)} + \frac{1}{Z_0}\frac{k_y}{k_\rho}a_v^{+(1)} - \frac{1}{Z_1}\frac{k_{1z}k_x}{k_1 k_\rho}b_h^{+(1)} - \frac{1}{Z_1}\frac{k_y}{k_\rho}b_v^{+(1)} + \frac{1}{Z_1}\frac{k_{1z}k_x}{k_1 k_\rho}b_h^{-(1)} - \frac{1}{Z_1}\frac{k_y}{k_\rho}b_v^{-(1)}$$

$$= \left[\frac{1}{Z_0} \left(-\frac{(k_{0z}^i)^2 k_x^i}{k_0 k_\rho^i} + \frac{(k_x - k_x^i)k_\rho^i}{k_0} \right) a_h^{+(0)} - \frac{1}{Z_0}\frac{k_{0z}^i k_y^i}{k_\rho^i} a_v^{+(0)} + \frac{1}{Z_1} \left(-\frac{(k_x - k_x^i)k_\rho^i}{k_1} + \frac{(k_{1z}^i)^2 k_x^i}{k_1 k_\rho^i} \right) b_h^{+(0)} \right.$$

$$+ \frac{1}{Z_1}\frac{k_{1z}^i k_y^i}{k_\rho^i} b_v^{+(0)} + \frac{1}{Z_1} \left(-\frac{(k_x - k_x^i)k_\rho^i}{k_1} + \frac{(k_{1z}^i)^2 k_x^i}{k_1 k_\rho^i} \right) b_h^{-(0)} - \frac{1}{Z_1}\frac{k_{1z}^i k_y^i}{k_\rho^i} b_v^{-(0)}$$

$$\left. + \frac{1}{Z_0} \left(-\frac{(k_{0z}^i)^2 k_x^i}{k_0 k_\rho^i} + \frac{(k_x - k_x^i)k_\rho^i}{k_0} \right) E_o^h + \frac{1}{Z_0}\frac{k_{0z}^i k_y^i}{k_\rho^i} E_o^v \right] \left(iF_1(\mathbf{k}_\perp - \mathbf{k}_\perp^i) \right) \quad (2.47)$$

$$\frac{k_x}{k_\rho}e^{-ik_{1z}d_1}b_h^{+(1)}+\frac{k_{1z}k_y}{k_1k_\rho}e^{-ik_{1z}d_1}b_v^{+(1)}+\frac{k_x}{k_\rho}e^{ik_{1z}d_1}b_h^{-(1)}$$

$$-\frac{k_{1z}k_y}{k_1k_\rho}e^{ik_{1z}d_1}b_v^{-(1)}-\frac{k_x}{k_\rho}e^{ik_{2z}d_1}c_h^{-(1)}+\frac{k_{2z}k_y}{k_2k_\rho}e^{ik_{2z}d_1}c_v^{-(1)}$$

$$=\left[\left(-\frac{(k_{1z}^i)^2k_y^i}{k_1k_\rho^i}+\frac{(k_y-k_y^i)k_\rho^i}{k_1}\right)e^{-ik_{1z}^id_1}b_v^{+(0)}-\frac{k_{1z}^ik_x^i}{k_\rho^i}e^{-ik_{1z}^id_1}b_h^{+(0)}\right.$$

$$+\left(\frac{(k_y-k_y^i)k_\rho^i}{k_1}-\frac{(k_{1z}^i)^2k_y^i}{k_1k_\rho^i}\right)e^{ik_{1z}^id_1}b_v^{-(0)}+\frac{k_{1z}^ik_x^i}{k_\rho^i}e^{ik_{1z}^id_1}b_h^{-(0)}$$

$$\left.-\left(\frac{(k_y-k_y^i)k_\rho^i}{k_2}-\frac{(k_{2z}^i)^2k_y^i}{k_2k_\rho^i}\right)e^{ik_{2z}^id_1}c_v^{-(0)}-\frac{k_{2z}^ik_x^i}{k_\rho^i}e^{ik_{2z}^id_1}c_h^{-(0)}\right]\left(iF_2(\mathbf{k}_\perp-\mathbf{k}_\perp^\mathbf{i})\right)\quad(2.48)$$

$$\frac{k_y}{k_\rho}e^{-ik_{1z}d_1}b_h^{+(1)}-\frac{k_{1z}k_x}{k_1k_\rho}e^{-ik_{1z}d_1}b_v^{+(1)}+\frac{k_y}{k_\rho}e^{ik_{1z}d_1}b_h^{-(1)}$$

$$+\frac{k_{1z}k_x}{k_1k_\rho}e^{ik_{1z}d_1}b_v^{-(1)}-\frac{k_y}{k_\rho}e^{ik_{2z}d_1}c_h^{-(1)}-\frac{k_{2z}k_x}{k_2k_\rho}e^{ik_{2z}d_1}c_v^{-(1)}$$

$$=\left[\left(\frac{(k_{1z}^i)^2k_x^i}{k_1k_\rho^i}-\frac{(k_x-k_x^i)k_\rho^i}{k_1}\right)e^{-ik_{1z}^id_1}b_v^{+(0)}-\frac{k_{1z}^ik_y^i}{k_\rho^i}e^{-ik_{1z}^id_1}b_h^{+(0)}\right.$$

$$+\left(-\frac{(k_x-k_x^i)k_\rho^i}{k_1}+\frac{(k_{1z}^i)^2k_x^i}{k_1k_\rho^i}\right)e^{ik_{1z}^id_1}b_v^{-(0)}+\frac{k_{1z}^ik_y^i}{k_\rho^i}e^{ik_{1z}^id_1}b_h^{-(0)}$$

$$\left.+\left(\frac{(k_x-k_x^i)k_\rho^i}{k_2}-\frac{(k_{2z}^i)^2k_x^i}{k_2k_\rho^i}\right)e^{ik_{2z}^id_1}c_v^{-(0)}-\frac{k_{2z}^ik_y^i}{k_\rho^i}e^{ik_{2z}^id_1}c_h^{-(0)}\right]\left(iF_2(\mathbf{k}_\perp-\mathbf{k}_\perp^\mathbf{i})\right)\quad(2.49)$$

$$-\frac{1}{Z_1}\frac{k_{1z}k_y}{k_1k_\rho}e^{-ik_{1z}d_1}b_h^{+(1)}+\frac{1}{Z_1}\frac{k_x}{k_\rho}e^{-ik_{1z}d_1}b_v^{+(1)}+\frac{1}{Z_1}\frac{k_{1z}k_y}{k_1k_\rho}e^{ik_{1z}d_1}b_h^{-(1)}$$

$$+\frac{1}{Z_1}\frac{k_x}{k_\rho}e^{ik_{1z}d_1}b_v^{-(1)}-\frac{1}{Z_2}\frac{k_{2z}k_y}{k_2k_\rho}e^{ik_{2z}d_1}c_h^{-(1)}-\frac{1}{Z_2}\frac{k_x}{k_\rho}e^{ik_{2z}d_1}c_v^{-(1)}$$

$$=\left[\frac{1}{Z_1}\left(\frac{(k_{1z}^i)^2k_y^i}{k_1k_\rho^i}-\frac{(k_y-k_y^i)k_\rho^i}{k_1}\right)e^{-ik_{1z}^id_1}b_h^{+(0)}-\frac{1}{Z_1}\frac{k_{1z}^ik_x^i}{k_\rho^i}e^{-ik_{1z}^id_1}b_v^{+(0)}+\frac{1}{Z_1}\left(-\frac{(k_y-k_y^i)k_\rho^i}{k_1}+\frac{(k_{1z}^i)^2k_y^i}{k_1k_\rho^i}\right)e^{ik_{1z}^id_1}b_h^{-(0)}\right.$$

$$+\frac{1}{Z_1}\frac{k_{1z}^ik_x^i}{k_\rho^i}e^{ik_{1z}^id_1}b_v^{-(0)}+\frac{1}{Z_2}\left(\frac{(k_y-k_y^i)k_\rho^i}{k_2}-\frac{(k_{2z}^i)^2k_y^i}{k_2k_\rho^i}\right)e^{ik_{2z}^id_1}c_h^{-(0)}$$

$$\left.-\frac{1}{Z_2}\frac{k_{2z}^ik_x^i}{k_\rho^i}e^{ik_{2z}^id_1}c_v^{-(0)}\right]\left(iF_2(\mathbf{k}_\perp-\mathbf{k}_\perp^\mathbf{i})\right)\quad(2.50)$$

and

$$\frac{1}{Z_1}\frac{k_{1z}k_x}{k_1 k_\rho}e^{-ik_{1z}d_1}b_h^{+(1)} + \frac{1}{Z_1}\frac{k_y}{k_\rho}e^{-ik_{1z}d_1}b_v^{+(1)} - \frac{1}{Z_1}\frac{k_{1z}k_x}{k_1 k_\rho}e^{ik_{1z}d_1}b_h^{-(1)}$$

$$+\frac{1}{Z_1}\frac{k_y}{k_\rho}e^{ik_{1z}d_1}b_v^{-(1)} + \frac{1}{Z_2}\frac{k_{2z}k_x}{k_2 k_\rho}e^{ik_{2z}d_1}c_h^{-(1)} - \frac{1}{Z_2}\frac{k_y}{k_\rho}e^{ik_{2z}d_1}c_v^{-(1)}$$

$$= \left[\frac{1}{Z_1}\left(-\frac{(k_{1z}^i)^2 k_x^i}{k_1 k_\rho^i} + \frac{(k_x - k_x^i)k_\rho^i}{k_1}\right)e^{-ik_{1z}^i d_1}b_h^{+(0)} - \frac{1}{Z_1}\frac{k_{1z}^i k_y^i}{k_\rho^i}e^{-ik_{1z}^i d_1}b_v^{+(0)} + \frac{1}{Z_1}\left(\frac{(k_x - k_x^i)k_\rho^i}{k_1} - \frac{(k_{1z}^i)^2 k_x^i}{k_1 k_\rho^i}\right)e^{ik_{1z}^i d_1}b_h^{-(0)} \right.$$

$$+ \frac{1}{Z_1}\frac{k_{1z}^i k_y^i}{k_\rho^i}e^{ik_{1z}^i d_1}b_v^{-(0)} + \frac{1}{Z_2}\left(-\frac{(k_x - k_x^i)k_\rho^i}{k_2} + \frac{(k_{2z}^i)^2 k_x^i}{k_2 k_\rho^i}\right)e^{ik_{2z}^i d_1}c_h^{-(0)}$$

$$\left. - \frac{1}{Z_2}\frac{k_{2z}^i k_y^i}{k_\rho^i}e^{ik_{2z}^i d_1}c_v^{-(0)} \right]\left(iF_2(\mathbf{k}_\perp - \mathbf{k}_\perp^i)\right) \quad (2.51)$$

This system of eight linear equations with the eight first-order $(m = 1)$ unknowns can be represented as

$$[\mathbf{A}(\mathbf{k}_\perp)]_{8\times 8} \cdot [\mathbf{x_1}(\mathbf{k}_\perp)]_{8\times 1} = [\mathbf{b_1}(\mathbf{k}_\perp)]_{8\times 1} \quad (2.52)$$

where $\mathbf{x_1}(\mathbf{k}_\perp) = [a_h^{+(1)} \ a_v^{+(1)} \ b_h^{+(1)} \ b_v^{+(1)} \ b_h^{-(1)} \ b_v^{-(1)} \ c_h^{-(1)} \ c_v^{-(1)}]^T$. It should be noted that the same matrix of coefficients appeared in (2.33), the zeroth-order system of equations. In fact, it can be seen that $\mathbf{A}(\mathbf{k}_\perp)$ is the matrix of coefficients for all orders. Analytical validation of the first-order solution is presented in Appendix A.2.

The coefficients that contribute to the first-order scattered field are $a_{h,v}^{+(1)}(\mathbf{k}_\perp)$. It can be shown that

$$a_h^{+(1)}(\mathbf{k}_\perp) = \alpha_h^{f_1}(\mathbf{k}_\perp)F_1(\mathbf{k}_\perp - \mathbf{k}_\perp^i) + \alpha_h^{f_2}(\mathbf{k}_\perp)F_2(\mathbf{k}_\perp - \mathbf{k}_\perp^i) \quad (2.53)$$

$$a_v^{+(1)}(\mathbf{k}_\perp) = \alpha_v^{f_1}(\mathbf{k}_\perp)F_1(\mathbf{k}_\perp - \mathbf{k}_\perp^i) + \alpha_v^{f_2}(\mathbf{k}_\perp)F_2(\mathbf{k}_\perp - \mathbf{k}_\perp^i) \quad (2.54)$$

where $F_1(\mathbf{k}_\perp)$ and $F_2(\mathbf{k}_\perp)$ are the Fourier transforms of $f_1(x, y)$ and $f_2(x, y)$, respectively. Calculation of the coefficients $\alpha_h^{f_1}(\mathbf{k}_\perp)$, $\alpha_h^{f_2}(\mathbf{k}_\perp)$, $\alpha_v^{f_1}(\mathbf{k}_\perp)$, and $\alpha_v^{f_2}(\mathbf{k}_\perp)$ is as follows.

From (2.44)–(2.51), it can be seen that the first four elements of $\mathbf{b_1}(\mathbf{k}_\perp)$ are linearly proportional to $F_1(\mathbf{k}_\perp - \mathbf{k}_\perp^i)$ and the last four elements are linearly proportional to $F_2(\mathbf{k}_\perp - \mathbf{k}_\perp^i)$. Inverting $\mathbf{A}(\mathbf{k}_\perp)$ and solving for the first two elements of $\mathbf{x_1}(\mathbf{k}_\perp)$, i.e., $a_{h,v}^{+(1)}(\mathbf{k}_\perp)$, will result in solutions in the form of linear superpositions of $F_1(\mathbf{k}_\perp - \mathbf{k}_\perp^i)$ and $F_2(\mathbf{k}_\perp - \mathbf{k}_\perp^i)$. The corresponding coefficients are named $\alpha_h^{f_1}(\mathbf{k}_\perp), \alpha_h^{f_2}(\mathbf{k}_\perp)$, $\alpha_v^{f_1}(\mathbf{k}_\perp)$, and $\alpha_v^{f_2}(\mathbf{k}_\perp)$, which can be

easily computed. To be more specific,

$$a_h^{+(1)}(\mathbf{k}_\perp) = \sum_{j=1}^{4} y_{1j} b_{1,j} + \sum_{j=5}^{8} y_{1j} b_{1,j} \tag{2.55}$$

where y_{1j} is the jth element of the first row of $\mathbf{Y}(\mathbf{k}_\perp)$, the inverse of $\mathbf{A}(\mathbf{k}_\perp)$, and $b_{1,j}$ is the jth element of $\mathbf{b_1}(\mathbf{k}_\perp)$. This relation can be rewritten as

$$a_h^{+(1)}(\mathbf{k}_\perp) = \left(\sum_{j=1}^{4} y_{1j} \frac{b_{1,j}}{F_1(\mathbf{k}_\perp - \mathbf{k}_\perp^i)} \right) \times F_1(\mathbf{k}_\perp - \mathbf{k}_\perp^i) \tag{2.56}$$

$$+ \left(\sum_{j=5}^{8} y_{1j} \frac{b_{1,j}}{F_2(\mathbf{k}_\perp - \mathbf{k}_\perp^i)} \right) \times F_2(\mathbf{k}_\perp - \mathbf{k}_\perp^i) \tag{2.57}$$

Therefore,

$$\alpha_h^{f_1}(\mathbf{k}_\perp) := \sum_{j=1}^{4} y_{1j} \frac{b_{1,j}}{F_1(\mathbf{k}_\perp - \mathbf{k}_\perp^i)} \tag{2.58}$$

and

$$\alpha_h^{f_2}(\mathbf{k}_\perp) := \sum_{j=5}^{8} y_{1j} \frac{b_{1,j}}{F_2(\mathbf{k}_\perp - \mathbf{k}_\perp^i)} \tag{2.59}$$

Similarly,

$$\alpha_v^{f_1}(\mathbf{k}_\perp) := \sum_{j=1}^{4} y_{2j} \frac{b_{1,j}}{F_1(\mathbf{k}_\perp - \mathbf{k}_\perp^i)} \tag{2.60}$$

and

$$\alpha_v^{f_2}(\mathbf{k}_\perp) := \sum_{j=5}^{8} y_{2j} \frac{b_{1,j}}{F_2(\mathbf{k}_\perp - \mathbf{k}_\perp^i)} \tag{2.61}$$

2.3.4 Scattering Coefficients

The first-order scattered field is

$$\mathbf{E_s^{(1)}}(\mathbf{r}) = \xi \int_{-\infty}^{\infty} \int_{-\infty}^{\infty} d\mathbf{k}_\perp \left[a_h^{+(1)}(\mathbf{k}_\perp) \hat{h}(k_{0z}) + a_v^{+(1)}(\mathbf{k}_\perp) \hat{v}(k_{0z}) \right] e^{ik_{0z}z} e^{i\mathbf{k}_\perp \cdot \mathbf{r}_\perp} \tag{2.62}$$

It should be noted that $\mathbf{E_s^{(1)}}(\mathbf{r})$ has a zero-mean and does not modify the coherent solution. The reason is that $a_{h,v}^{+(1)}(\mathbf{k}_\perp)$ are linearly proportional to $F_1(\mathbf{k}_\perp - \mathbf{k}_\perp^i)$ and $F_2(\mathbf{k}_\perp - \mathbf{k}_\perp^i)$.

Noting that

$$\langle F_{1,2}(\mathbf{k}_\perp - \mathbf{k}_\perp^i)\rangle = \frac{1}{(2\pi)^2} \int\limits_{-\infty}^{\infty}\int\limits_{-\infty}^{\infty} d\mathbf{r}_\perp e^{-i(\mathbf{k}_\perp - \mathbf{k}_\perp^i)\cdot\mathbf{r}_\perp} \langle f_{1,2}(x,y)\rangle = 0 \qquad (2.63)$$

it will be obvious that $\langle \mathbf{E}_s^{(1)}(\mathbf{r})\rangle = 0$. Therefore, we would need to calculate the second-order solution to modify the coherent scattered field.

If $\mathbf{k_0}\cdot\mathbf{r}$ is large, (2.62) can be expanded asymptotically using the stationary phase method; it can be shown that [50]

$$\mathbf{E}_s^{(1)}(\mathbf{r}) \simeq -i\xi 2\pi k_0 \cos\theta_s \frac{e^{ik_0 r}}{r}\left(a_h^{+(1)}(\mathbf{k}_\perp^s)\hat{h}(k_{0z}^s) + a_v^{+(1)}(\mathbf{k}_\perp^s)\hat{v}(k_{0z}^s)\right) \qquad (2.64)$$

where $k_{0z}^s = \sqrt{k_0^2 - (k_x^s)^2 - (k_y^s)^2}$, $k_x^s = k_0\sin\theta_s\cos\phi_s$, and $k_y^s = k_0\sin\theta_s\sin\phi_s$. The sub/superscript 's' refers to the scattered (observation) direction.

The scattering coefficient σ_{pq}^o is defined as

$$\sigma_{pq}^o := \lim_{r\to\infty}\lim_{A\to\infty}\frac{4\pi r^2}{A}\langle|\mathbf{E}_s^{(1)}(\mathbf{r})\cdot\hat{p}(k_{0z}^s)|^2\rangle, \qquad p,q \in \{v,h\} \qquad (2.65)$$

with A being the illuminated area and the incident field being $\hat{q}(-k_{0z}^i)$. Inserting (2.64) into (2.65), while using (2.53)–(2.54), will lead to

$$\sigma_{pq}^o = 4\pi k_0^2 \cos^2\theta_s\xi^2\left(|\alpha_{pq}^{f_1}(\mathbf{k}_\perp^s)|^2 W_{f_1}(\mathbf{k}_\perp^s-\mathbf{k}_\perp^i)+2\Re\{\alpha_{pq}^{f_1}(\mathbf{k}_\perp^s)\alpha_{pq}^{f_2*}(\mathbf{k}_\perp^s)\}W_{f_1f_2}(\mathbf{k}_\perp^s-\mathbf{k}_\perp^i)+|\alpha_{pq}^{f_2}(\mathbf{k}_\perp^s)|^2 W_{f_2}(\mathbf{k}_\perp^s-\mathbf{k}_\perp^i)\right)$$
$$(2.66)$$

where $\alpha_{pq}^{f_i}(\mathbf{k}_\perp^s) = \alpha_p^{f_i}(\mathbf{k}_\perp^s)$ with the incident field being $\hat{q}(-k_{0z}^i)$. $W_{f_1}(\mathbf{k}_\perp)$ and $W_{f_2}(\mathbf{k}_\perp)$ are the power spectral densities of the rough boundaries, whose joint spectral density is denoted by $W_{f_1f_2}(\mathbf{k}_\perp)$. For a brief note on power spectral density, refer to Appendix A.3.

The above equations express the first-order bistatic scattering coefficients in terms of spectral densities of the two surfaces and the coefficients $\alpha_{h,v}^{f_i}$, which include the first-order rough surface effects and all orders of interactions between the two boundaries. We note that as far as the first-order scattered field is considered, there is no depolarization in the backscattering direction, a well-established fact in the case of a single rough interface [37].

To have the continuity of the electric field satisfied at $z = \xi f_1(x, y)$, this should be true for the transmitted field in Region 1 as well. By means of ray tracing, we can conclude that the cross-polarized components of the scattered field in Region 0 in the backscattering direction will be zero. If this analysis was carried out to the second order, the cross-polarized components of the backscattered field would not be zero.

2.4   Extension to More Layers

The analysis of the two-layer case can be extended to more layers. Extension from two layers to three layers is somewhat tricky, but once the three-layer analysis is complete, extension to more layers is straightforward.

Consider a three-layer dielectric structure as in Fig. 2.2 with a geometry similar to that of the two-layer structure, and assume the boundaries are denoted by $z = \xi f_1(x, y)$, $z = -d_1 + \xi f_2(x, y)$, and $z = -d_2 + \xi f_3(x, y)$. Assumptions are similar to those for the two-layer case, i.e., the boundaries are zero-mean, stationary random processes, and their roughnesses are small compared to the wavelength. The new unknown amplitudes are $A_{h,v}^+(\mathbf{k}_\perp)$, $B_{h,v}^\pm(\mathbf{k}_\perp)$, $C_{h,v}^\pm(\mathbf{k}_\perp)$, and $D_{h,v}^-(\mathbf{k}_\perp)$.
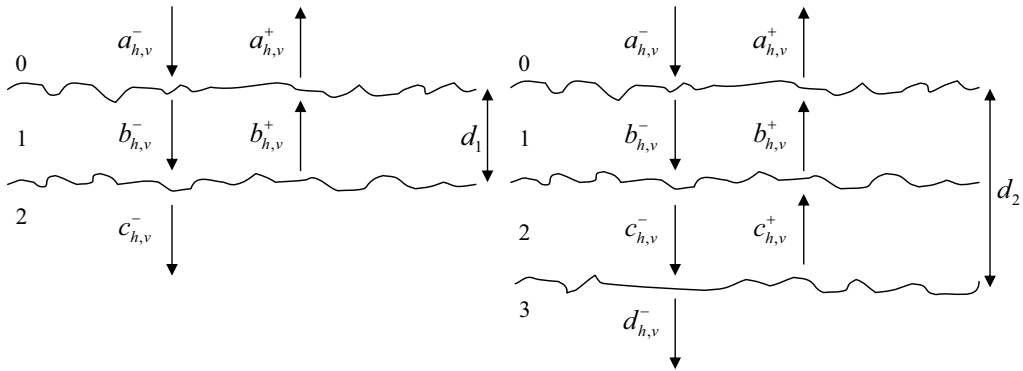
Figure 2.2: Two-layer structure versus three-layer structure. The figure shows thicknesses, and amplitudes of the up- and down-going waves.

To derive the two 12×12 systems of linear equations for the zeroth- and first-order solutions, note that for any order, the first four equations in the case of a two-layer medium, i.e., (2.25)–(2.28) and (2.44)–(2.47), which result from the boundary conditions at $z =$

$\xi f_1(x, y)$, do not change, because in both cases of two- and three-layer structures, these equations correspond to the same boundary, media, and unknowns. The last four equations in the case of a two-layer medium, i.e., (2.29)–(2.32) and (2.48)–(2.51), which result from the boundary conditions at $z = -d_1 + \xi f_2(x, y)$, can be used for the three-layer case as well after we apply the following changes in order: $c \to d$, $b \to c$, $2 \to 3$, $1 \to 2$, $f_2 \to f_3$ and $d_1 \to d_2$. The resulting equations correspond to the boundary conditions at $z = -d_2 + \xi f_3(x, y)$ for a three-layer structure.

Derivation of the boundary-condition equations at $z = -d_1 + \xi f_2(x, y)$ for the three-layer structure needs specific attention. Note that apart from the indices, the up-going (or down-going) amplitudes on both sides of an interface appear analogously on both sides of the corresponding boundary conditions. These terms, however, will be analogous up to sign when the equations are formed, because now all unknowns appear on one side of each equation. Therefore, Fig. 2.2 suggests that, for each order, we take the four boundary-condition equations at $z = -d_1 + \xi f_2(x, y)$ in the case of a two-layer medium, i.e., (2.29)–(2.32) and (2.48)–(2.51), and add to each equation terms that account for the up-going amplitudes $c_{h,v}^+$. These terms are the negative of the terms containing $b_{h,v}^+$ at the same boundary, except we should apply the following changes to the new terms: $b \to c$ and $1 \to 2$. The reader should note that in this case, the index change only applies to terms that are dielectric-constant dependent. For example, (2.48) should be changed to

$$
\frac{k_x}{k_\rho} e^{-ik_{1z}d_1} b_h^{+(1)} + \frac{k_{1z}k_y}{k_1 k_\rho} e^{-ik_{1z}d_1} b_v^{+(1)} + \frac{k_x}{k_\rho} e^{ik_{1z}d_1} b_h^{-(1)} - \frac{k_{1z}k_y}{k_1 k_\rho} e^{ik_{1z}d_1} b_v^{-(1)}
$$

$$
- \frac{k_x}{k_\rho} e^{-ik_{2z}d_1} c_h^{+(1)} - \frac{k_{2z}k_y}{k_2 k_\rho} e^{-ik_{2z}d_1} c_v^{+(1)} - \frac{k_x}{k_\rho} e^{ik_{2z}d_1} c_h^{-(1)} + \frac{k_{2z}k_y}{k_2 k_\rho} e^{ik_{2z}d_1} c_v^{-(1)}
$$

$$
= \left[\left(-\frac{(k_{1z}^i)^2 k_y^i}{k_1 k_\rho^i} + \frac{(k_y - k_y^i)k_\rho^i}{k_1} \right) e^{-ik_{1z}^i d_1} b_v^{+(0)} - \frac{k_{1z}^i k_x^i}{k_\rho^i} e^{-ik_{1z}^i d_1} b_h^{+(0)} \right.
$$

$$
+ \left(\frac{(k_y - k_y^i)k_\rho^i}{k_1} - \frac{(k_{1z}^i)^2 k_y^i}{k_1 k_\rho^i} \right) e^{ik_{1z}^i d_1} b_v^{-(0)} + \frac{k_{1z}^i k_x^i}{k_\rho^i} e^{ik_{1z}^i d_1} b_h^{-(0)}
$$

$$
- \left(-\frac{(k_{2z}^i)^2 k_y^i}{k_2 k_\rho^i} + \frac{(k_y - k_y^i)k_\rho^i}{k_2} \right) e^{-ik_{2z}^i d_1} c_v^{+(0)} + \frac{k_{2z}^i k_x^i}{k_\rho^i} e^{-ik_{2z}^i d_1} c_h^{+(0)}
$$

$$
\left. - \left(\frac{(k_y - k_y^i)k_\rho^i}{k_2} - \frac{(k_{2z}^i)^2 k_y^i}{k_2 k_\rho^i} \right) e^{ik_{2z}^i d_1} c_v^{-(0)} - \frac{k_{2z}^i k_x^i}{k_\rho^i} e^{ik_{2z}^i d_1} c_h^{-(0)} \right] \left(iF_2(\mathbf{k}_\perp - \mathbf{k}_\perp^i) \right) \quad (2.67)
$$

Now, similar to the two-layer case, it can be shown that

$$a_h^{+(1)}(\mathbf{k}_\perp) = \alpha_h^{f_1}(\mathbf{k}_\perp)F_1(\mathbf{k}_\perp - \mathbf{k}_\perp^i) + \alpha_h^{f_2}(\mathbf{k}_\perp)F_2(\mathbf{k}_\perp - \mathbf{k}_\perp^i) + \alpha_h^{f_3}(\mathbf{k}_\perp)F_3(\mathbf{k}_\perp - \mathbf{k}_\perp^i) \qquad (2.68)$$

and

$$a_v^{+(1)}(\mathbf{k}_\perp) = \alpha_v^{f_1}(\mathbf{k}_\perp)F_1(\mathbf{k}_\perp - \mathbf{k}_\perp^i) + \alpha_v^{f_2}(\mathbf{k}_\perp)F_2(\mathbf{k}_\perp - \mathbf{k}_\perp^i) + \alpha_v^{f_3}(\mathbf{k}_\perp)F_3(\mathbf{k}_\perp - \mathbf{k}_\perp^i) \qquad (2.69)$$

Therefore, the bistatic scattering coefficients are

$$\sigma_{pq}^o = 4\pi k_0^2 \cos^2\theta_s \xi^2 \left(|\alpha_{pq}^{f_1}(\mathbf{k}_\perp^s)|^2 W_{f_1}(\mathbf{k}_\perp^s - \mathbf{k}_\perp^i) + |\alpha_{pq}^{f_2}(\mathbf{k}_\perp^s)|^2 W_{f_2}(\mathbf{k}_\perp^s - \mathbf{k}_\perp^i) + |\alpha_{pq}^{f_3}(\mathbf{k}_\perp^s)|^2 W_{f_3}(\mathbf{k}_\perp^s - \mathbf{k}_\perp^i) \right) \qquad (2.70)$$

where it is assumed that the boundaries are independent random processes.

An interesting special case is when the bottom medium is a perfect conductor. One way of simulating a good conductor is assigning a large value to the imaginary part of the third layer dielectric constant. Alternatively, a perfect conductor can be simulated by modifying the boundary-condition equations, because the boundary condition equation that is analogous to (2.21), which results from continuity of the tangential magnetic field at $z = -d_2 + \xi f_3(x, y)$, does not hold when Region 3 is a perfect conductor. Therefore, the last two equations, which correspond to the $\hat{x}$ and $\hat{y}$ components of the equation analogous to (2.21), should be eliminated. Moreover, since no field exists in a perfect conductor, $d_{h,v}^{-(m)}(\mathbf{k}_\perp)$ are zero, and therefore, the two columns corresponding to these two unknowns should be eliminated from the 12×12 system of equation. The resulting 10×10 system of equations gives the solution to this special case. The bistatic scattering coefficients will have the same form as (2.70), with $\alpha_{pq}^{f_i}(\mathbf{k}_\perp^s)$ having different numerical values.

2.5 Validation and Numerical Results

2.5.1 Validation

The first-order coefficients depend on the zeroth-order solution, and by validating the final formulation, we are actually validating the zeroth-order coefficients, too. Regardless, we can easily validate the zeroth-order solution to the two-layer problem by showing that $a_{h,v}^{+(0)}(\mathbf{k}_\perp)$ can be represented as the well-known reflection coefficients of a two-layer dielectric structure, which can be found in the literature [51]. Appendix A.2 shows the detail. To validate the first-order coefficients, some special cases to which known solutions exist are considered: (1) single rough interface and (2) one flat and one rough interface. In Appendix A.2, an analytical validation has been presented.

2.5.2 Numerical Results

Some numerical results are presented in this part. In all of the cases below, a Gaussian correlation function for the boundaries is assumed, that is $C(\mathbf{r}_\perp) = e^{-|\mathbf{r}_\perp|^2/l^2}$, which results in a spectral density of the form $W(\mathbf{k}_\perp) = \frac{\sigma^2 l^2}{4\pi} e^{-|\mathbf{k}_\perp|^2 l^2/4}$, where l and σ are the correlation length and standard deviation of the surface height, respectively.

Fig. 2.3 shows the effect of the second interface roughness on backscattering coefficients. It is observed that as the roughness increases, the backscattered power also increases, as expected. The reason is that the second interface itself produces more non-specular scattered power, part of which is now available to be backscattered into the region of incidence. For this case, $\epsilon_{1r} = 5$, $\epsilon_{2r} = 10$, $d_1 = \lambda_1$, $k_0 l_{f_1} = k_0 l_{f_2} = 3.0$, and $k_0 \sigma_{f_1} = 0.3$.

The effect of loss on backscattering coefficients is shown in Fig. 2.4. All parameters are the same as those of the previous case except that $k_0 \sigma_{f_2} = 0.1$ and loss has been added to both dielectric constants. Both Region 1 and Region 2 are assumed to have identical loss tangents denoted by $\tan \delta$. By adding loss, we are actually adding more contrast between the region of incidence and Region 1. This will cause more backscattered power. However, for the total scattered wave in Region 0, this contrast could be counteracted by the power loss in Region 1. In other words, the loss in Region 1 masks the second interface roughness,

therefore less scattered power will be observed. There is a compromise between these two effects. In this case, contrast is dominating power loss.

Fig. 2.5 shows the effect of the second interface roughness on bistatic scattering coefficients. Note the Brewster-like effect in the vertical polarization. There is a distinction between this case and the case of flat interfaces. When both interfaces are flat, and with a fixed incidence angle, power is only scattered in the specular direction, which may or may not correspond to the Brewster angle. However, in the case of rough interfaces with a fixed incidence angle, this effect is being observed in a direction which is not necessarily the specular direction. An increase in the scattering coefficient as the roughness increases is observed again. Here, it is assumed that $\epsilon_{1r} = 5$, $\epsilon_{2r} = 10$, $d_1 = \lambda_1$, $k_0 l_{f_1} = k_0 l_{f_2} = 1.5$, $k_0 \sigma_{f_1} = 0.15$, and $\theta_i = 135°$.

In all of the above cases, $d_1 = \lambda_1$, the wavelength inside the middle layer. The effect of the middle layer thickness on backscattering coefficients is shown in Fig. 2.6. The oscillatory behavior is attributed to pseudo-resonance effects between the two boundaries. A similar phenomenon is observed when one of the boundaries is flat. For this case, $\epsilon_{1r} = 5$, $\epsilon_{2r} = 10$, $k_0 l_{f_1} = k_0 l_{f_2} = 1.5$, and $k_0 \sigma_{f_1} = k_0 \sigma_{f_2} = 0.15$.

Fig. 2.7 shows the effect of the third interface roughness (a) and the third layer dielectric constant (b) on backscattering coefficients. As expected, more backscattered power is observed when roughness or dielectric constant increase. When the third layer is a perfect conductor, the increase in backscattered power is more pronounced. Here, it is assumed that $\epsilon_{1r} = 2$, $\epsilon_{2r} = 5$, $2d_1 = d_2 = 1$ m, $k_0 l_{f_1} = k_0 l_{f_2} = k_0 l_{f_3} = 1$, and $k_0 \sigma_{f_1} = 1.5 k_0 \sigma_{f_2} = 0.3$. In (a), $\epsilon_{3r} = 8$ and in (b), $k_0 \sigma_{f_3} = 0.1$

2.6   Summary and Conclusion

An analytical method to calculate the bistatic scattering coefficients of two- and three-layer dielectric structures with rough interfaces has been developed and validated. Several new results were reported for various combinations of parameters. The assumption of independence of the rough interfaces was removed for the general case. The analysis is based on the Small Perturbation Method (SPM), where the boundary conditions at all interfaces are
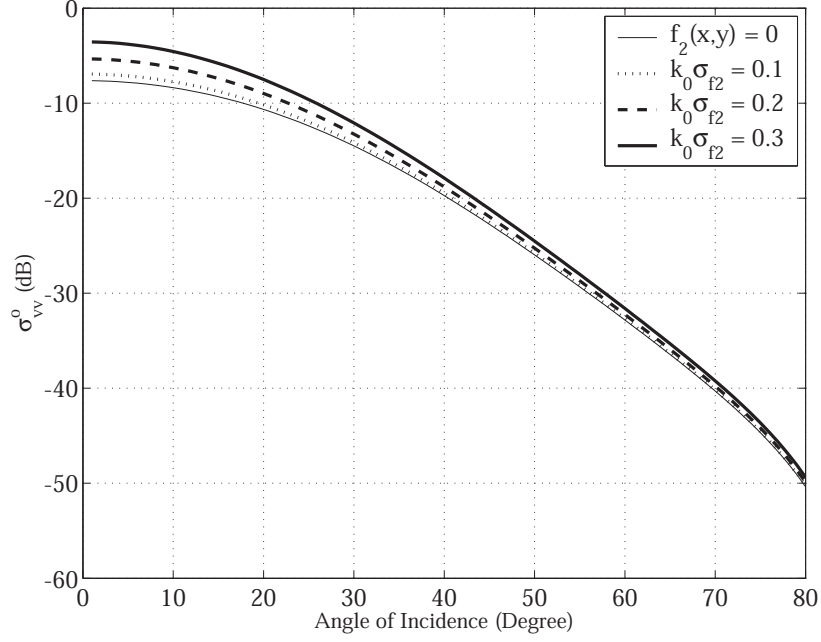
(a)
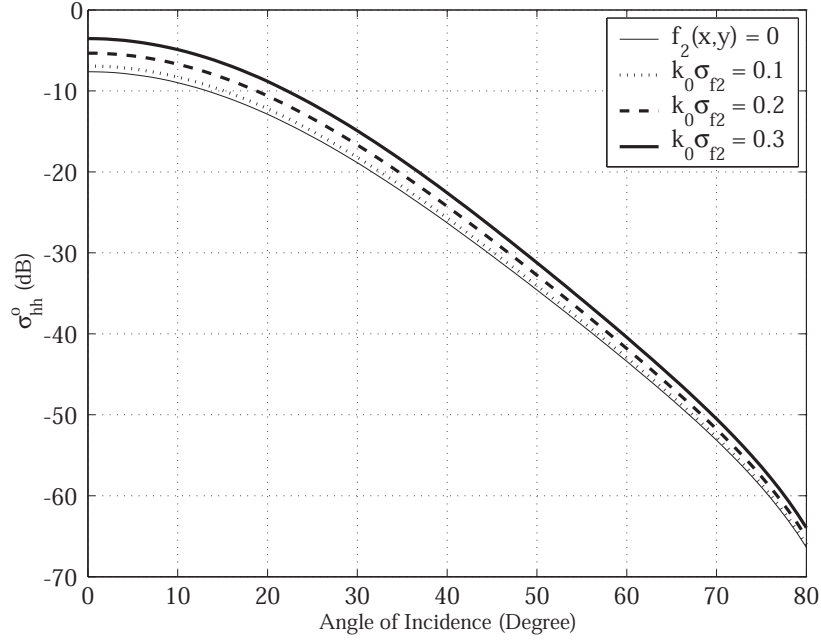
(b)

Figure 2.3: Two layers: the effect of the second interface roughness on backscattering coefficients for (a) VV and (b) HH polarizations. It is observed that as the roughness increases, the backscattered power also increases. Parameters: $\epsilon_{1r} = 5$, $\epsilon_{2r} = 10$, $d_1 = \lambda_1$, $k_0 l_{f_1} = k_0 l_{f_2} = 3.0$, and $k_0 \sigma_{f_1} = 0.3$.
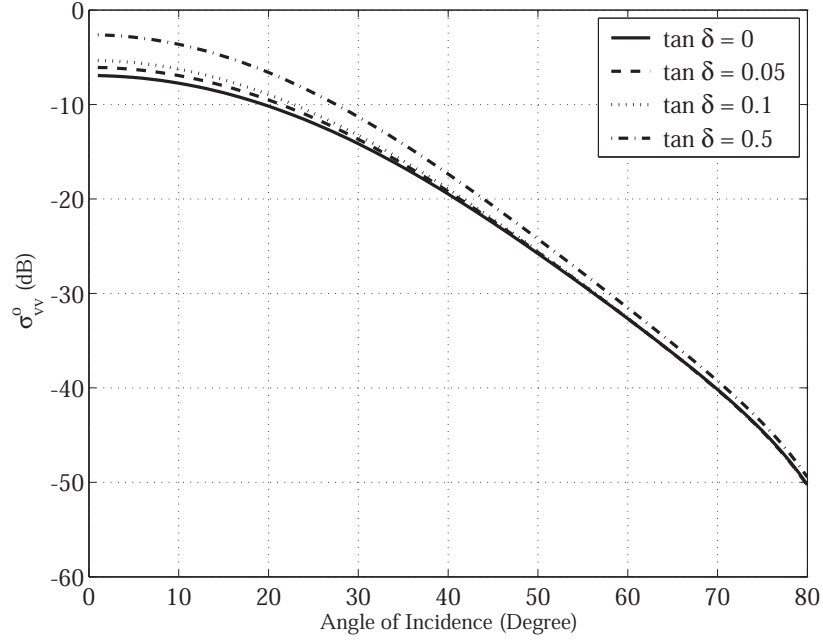
(a)
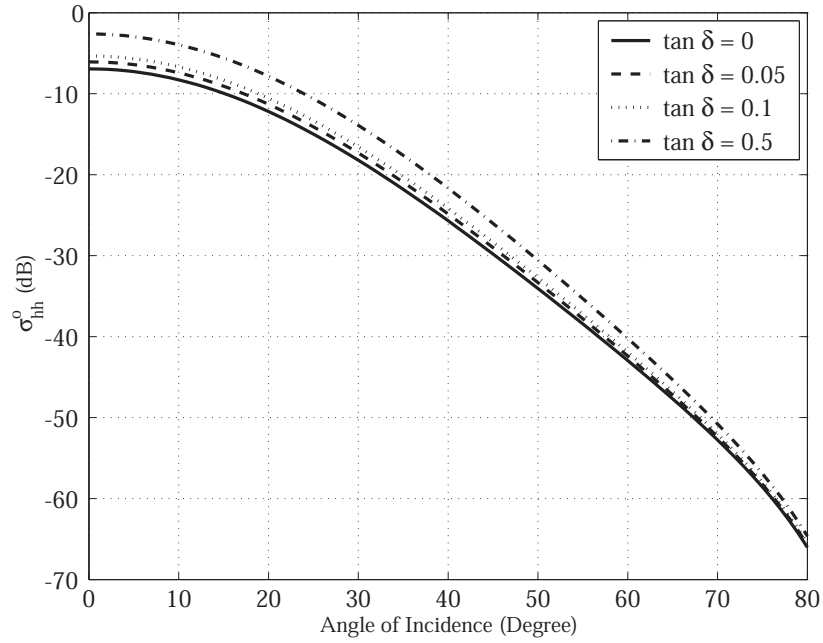
(b)

Figure 2.4: Two layers: the effect of loss on backscattering coefficients for (a) VV and (b) HH polarizations. Both Region 1 and Region 2 are assumed to have identical loss tangents denoted by $\tan\delta$. By adding loss, we are actually adding more contrast between the region of incidence and Region 1. This will cause more backscattered power. Parameters: $\epsilon'_{1r} = 5$, $\epsilon'_{2r} = 10$, $d_1 = \lambda_1$, $k_0 l_{f_1} = k_0 l_{f_2} = 3.0$, and $k_0 \sigma_{f_1} = 3k_0 \sigma_{f_2} = 0.3$.
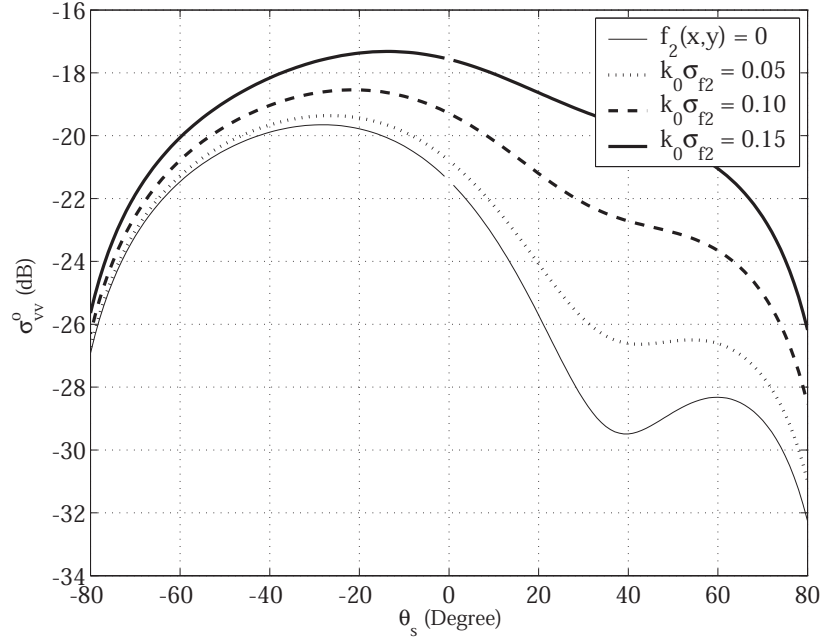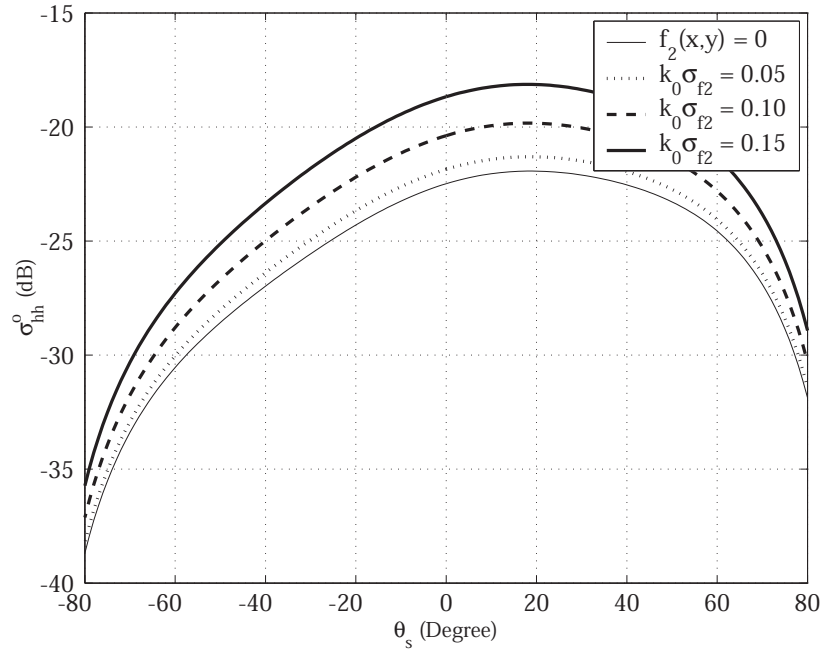
Figure 2.5: Two layers: the effect of the second interface roughness on bistatic scattering coefficients for (a) VV and (b) HH polarizations. Note the Brewster-like effect in VV polarization. Parameters: $\epsilon_{1r} = 5$, $\epsilon_{2r} = 10$, $d_1 = \lambda_1$, $k_0 l_{f_1} = k_0 l_{f_2} = 1.5$, $k_0 \sigma_{f_1} = 0.15$, and $\theta_i = 135°$.
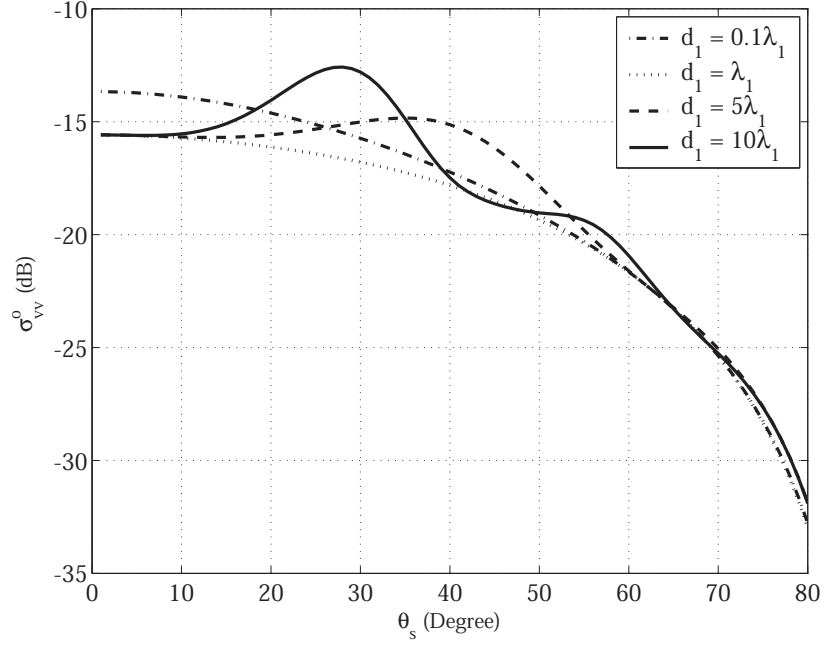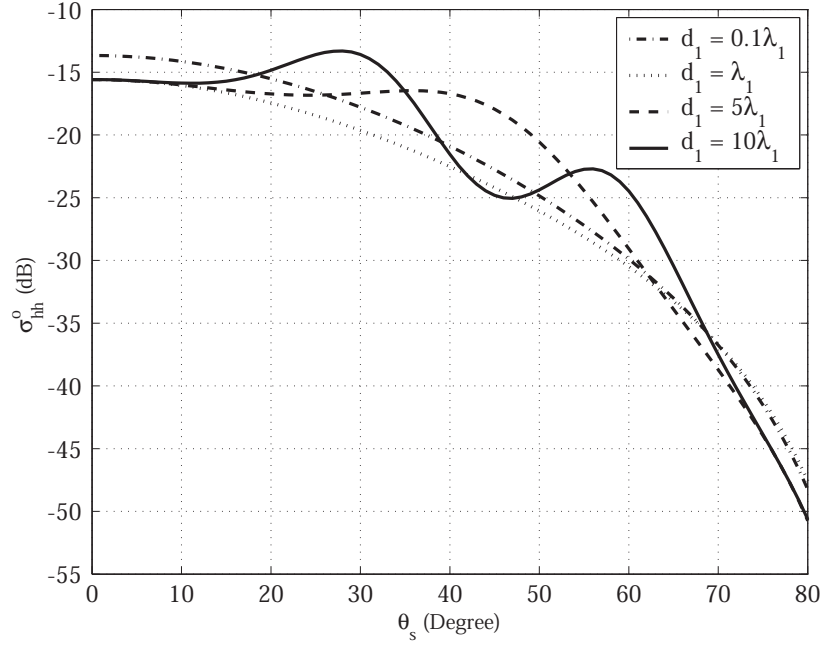
Figure 2.6: Two layers: the effect of the first layer thickness on backscattering coefficients for (a) VV and (b) HH polarizations. The oscillatory behavior is attributed to pseudo-resonance effects between the two boundaries. Parameters: $\epsilon_{1r} = 5$, $\epsilon_{2r} = 10$, $k_0 l_{f_1} = k_0 l_{f_2} = 1.5$, and $k_0 \sigma_{f_1} = k_0 \sigma_{f_2} = 0.15$.
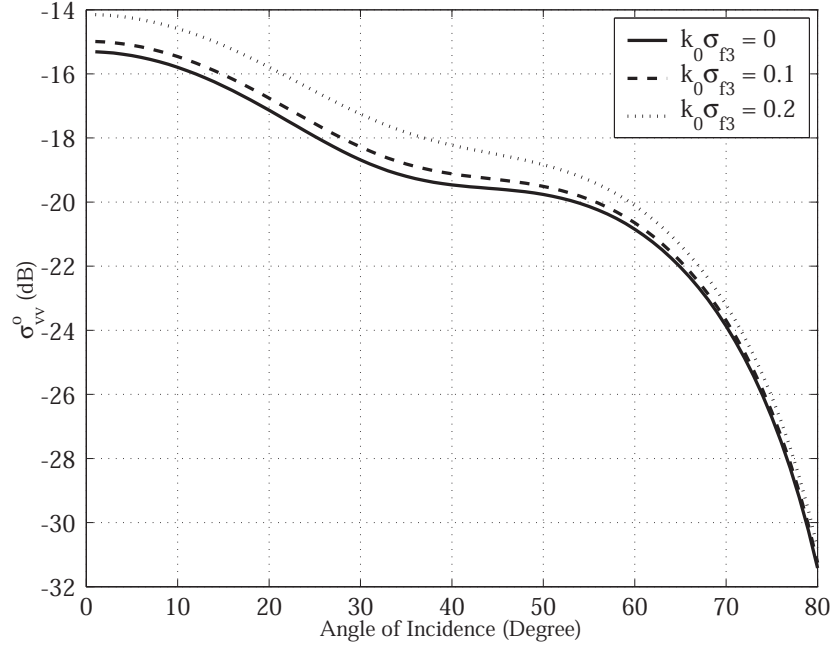
(a)
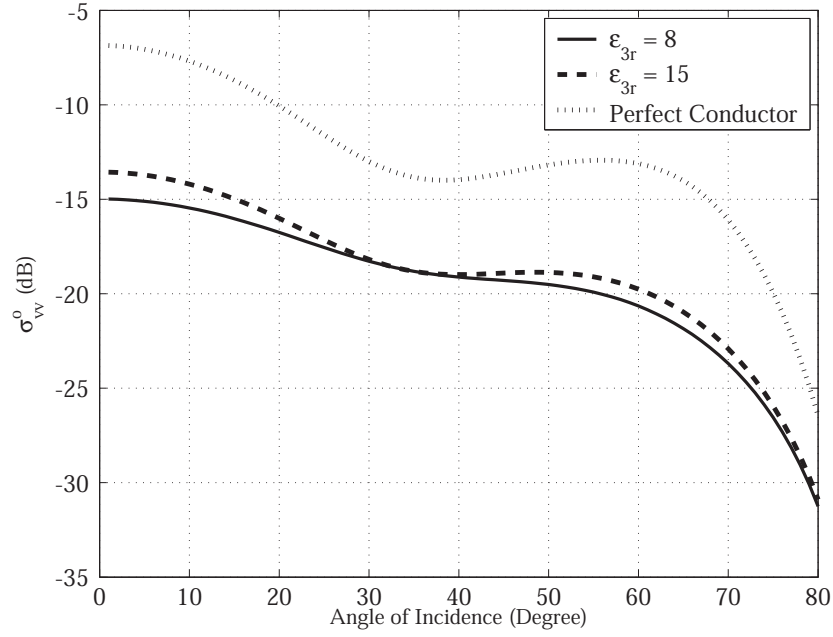
(b)

Figure 2.7: Three layers: the effect of the third layer (a) roughness and (b) dielectric constant on backscattering coefficients for VV polarization. Parameters: $\epsilon_{1r} = 2$, $\epsilon_{2r} = 5$, $2d_1 = d_2 = 1$ m, $k_0 l_{f_1} = k_0 l_{f_2} = k_0 l_{f_3} = 1$, and $k_0 \sigma_{f_1} = 1.5 k_0 \sigma_{f_2} = 0.3$. In (a), $\epsilon_{3r} = 8$ and in (b), $k_0 \sigma_{f_3} = 0.1$.

matched to the first order. The method intrinsically takes into account multiple scattering processes between boundaries which are considered rough simultaneously, hence making the method suitable for extension to higher orders. The formulation was also shown to be easily extended to more layers. These are main distinguishing factors of this work compared to some of the previous studies.

The proposed method provides an efficient analytical means for solving the layered rough-surface problem. Although the solution is valid for slightly rough boundaries only, it is well suited for its intended purpose, which is mainly the remote sensing of layered subsurfaces using low-frequency radars. The computational cost of numerical techniques is rather high given that many realizations of each of the randomly-rough interfaces have to be simulated. The present solution, instead, presents a very practical and realistic alternative with negligible computational overhead. Furthermore, the assumption of slight roughness is a valid one for this type of application, because to collect discernible data from the subsurface, lower frequency signals, e.g., in the VHF and UHF range, need to be used to achieve reasonable penetration depths. In turn, at these frequencies, most surfaces of interest appear only slightly rough. Therefore, even if the SPM assumptions are removed, gains in accuracy are expected to be minimal. This method is well suited for developing fast, near-real-time inversion/estimation techniques needed in many scientific and operational applications including inversion of subsurface soil-layer properties.

CHAPTER 3

Derivation of Validity Region of SPM Simulation of One-Dimensional Two-Layer Rough Surfaces

In the previous chapter, the bistatic scattering coefficients of a three-dimensional, two-layer dielectric structure with slightly rough boundaries were derived. Use of the Small Perturbation Method (SPM) raises the question about its region of validity. In this work, the region of validity pertains to the conditions on each layer's roughness, slope, and permittivity for which the first-order SPM is accurate within a specified error bound. To this end, the SPM solution needs to be compared to a solution derived using a method that does not impose roughness restrictions. Analytical solutions are almost always approximate, and therefore, our inquiry should be numerical. In this chapter, a PMCHWT-based[1] integral equation [52–54] is used to analyze scattering from a large ensemble of two-layer structures. The emphasis here is more on developing a systematic comparison between the analytic and numerical solution rather than the numerical technique itself. To accelerate the numerical solver, the off-diagonal blocks in the Method of Moments (MoM) interaction matrix are approximated in terms of low-rank products [55]. Simulations are performed for 1D rough surfaces represented by zero-mean stationary random processes, separating homogeneous dielectric layers.

---

[1]PMCHWT stands for Poggio-Miller-Chang-Harrington-Wu-Tsai.

3.1 Introduction

The problem of scattering from a random rough surface is a challenging problem with no exact analytical solutions, and therefore, we are forced to use approximation schemes to calculate the scattered wave. The oldest and most widely used approximations are SPM [34] and the Kirchhoff approximation [56]. Several rough surface scattering models have been developed over the past decades to increase the accuracy of the old models over various parameters of the rough surface, but SPM and the Kirchhoff approximation are the most common among the schemes that have been proposed recently.

A clear understanding of the region of validity of the approximate solutions is necessary in order to use them properly. SPM is generally valid when the root-mean-square of the surface height is 'small' compared to the wavelength. Moreover, in many treatments of the perturbation theory, the root-mean-square of the surface slope has also been assumed to be small compared to the wavelength. However, the precise range of applicability of SPM and the connection between the small slope approximation and the validity of SPM is not fully understood.

To find the region of validity of a scattering model, its solution should be compared with a solution that does not impose any restriction on the rough surface properties. A numerical method is therefore used to solve the scattering problem for an ensemble of realizations of the rough surface. The most widely used numerical method, which is also used in this chapter, is the Method of Moments (MoM) [57]. The comparison between the approximate and numerical solutions needs to be made for many samples of the model parameters of interest such as correlation length and standard deviation of the rough surface. Since numerical solutions are computationally expensive, dense sampling of points from the model space is the major difficulty in deriving regions of validity for rough surface scattering models.

There have been many quantitative studies on the region of validity of different approximations for scattering from single rough surfaces [58–60]. These studies have been restricted to one-dimensional perfectly conductive random rough surfaces that are Gaussian. Improvements in computational power over the years have allowed denser sampling of the model parameters than was possible before [61].

When scattering from layered rough surfaces is considered, the assumption of slight roughness is often valid when probing the layered structure using low-frequency radars. Indeed, at low frequencies, most surfaces of interest are only slightly rough such that even if the structure is analyzed using an exact method without making this assumption, gains in accuracy are expected to be minimal. Therefore, it is imperative to investigate the conditions on surface roughness and slope for which the first-order SPM is accurate within a specified error bound.

This chapter presents a study of the region of validity of SPM for a one-dimensional, two-layer dielectric structure with Gaussian height distribution and Gaussian autocorrelation function. Numerical simulations for one-dimensional surfaces give a quantitative understanding of the validity region of various approximations, which are assumed to be accurate as well when applied to two-dimensional surfaces. Most of the previous studies have used surfaces with Gaussian height distribution and Gaussian autocorrelation function, because such surfaces are simplest to describe statistically and can be described fully by the surface height standard deviation and correlation length. Moreover, such surfaces are more amenable to numerical computation, although many surfaces in nature may have other statistical properties. Region of validity is expressed as a function of standard deviation and correlation length of the rough surface. The effect of incidence angle on the region of validity is not studied here, because MoM fails for large incidence angles. We should note that the scattering problem in the case of near grazing incidence or scattered angle is of much interest in applications such as shipborne and airborne radar backscatter from land and sea. The region of validity of SPM for a perfectly conductive single rough surface in the case of near grazing incidence angle has been studied by means of numerical simulations that work for grazing angles as small as $0.1°$ [62]. The effect of the material property on the region of validity of the first-order perturbation theory has also been studied [63]. All of these studies have considered a one-dimensional Gaussian random rough surface.

In the next section, the problem geometry is introduced and the PMCHWT equations are derived from the boundary conditions using the equivalence principle. The MoM formulation is presented in Section 3.3. The fast solver is discussed in Section 3.6 followed by numerical results. Section 3.8 addresses the region of validity of SPM for a two-layer rough surface

structure.

3.2 Problem Geometry and Formulation

The same problem geometry as in Chapter 2 is used except that the rough surfaces are considered one dimensional in this chapter. Consider the two-dimensional, two-layer isotropic dielectric structure shown in Fig. 3.1. The top and bottom regions are half-spaces and the layers dielectric constants are ϵ_0, ϵ_1, and ϵ_2. The permeability of all layers is assumed to be μ_0. The boundaries are denoted by $y_1 = f_1(x)$ and $y_2 = -d + f_2(x)$, where both $f_1(x)$ and $f_2(x)$ are zero-mean, stationary random processes with known, distinct statistical properties. The numerical generation of such boundaries is presented in Appendix B.1.
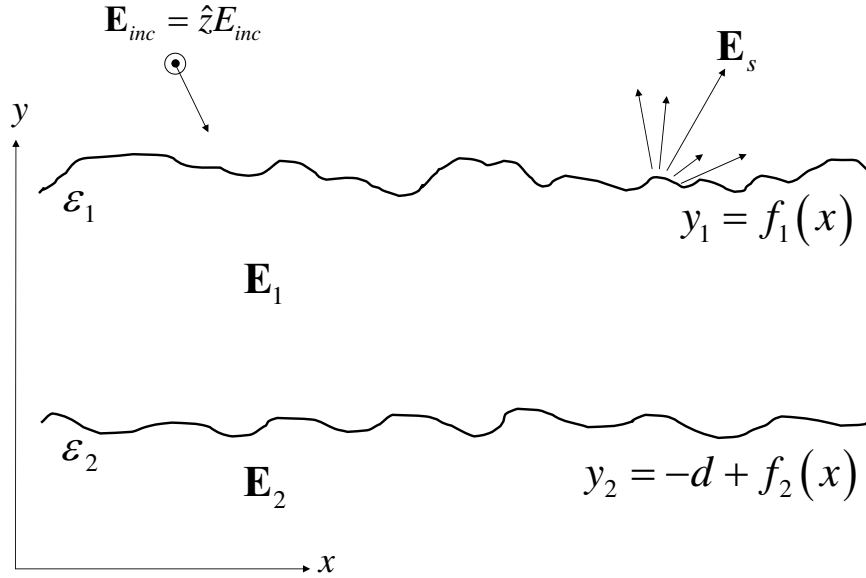
Figure 3.1: Geometry of the problem: a 2D double layer rough surface structure with homogeneous layers.

To solve the scattering problem, i.e., to find the scattered wave, surface equivalence principle is used to form surface integral equations. The three equivalent problems along with the corresponding fields and equivalent current sources are shown in Fig. 3.2. The

equivalent currents and their signs are determined from the boundary conditions.
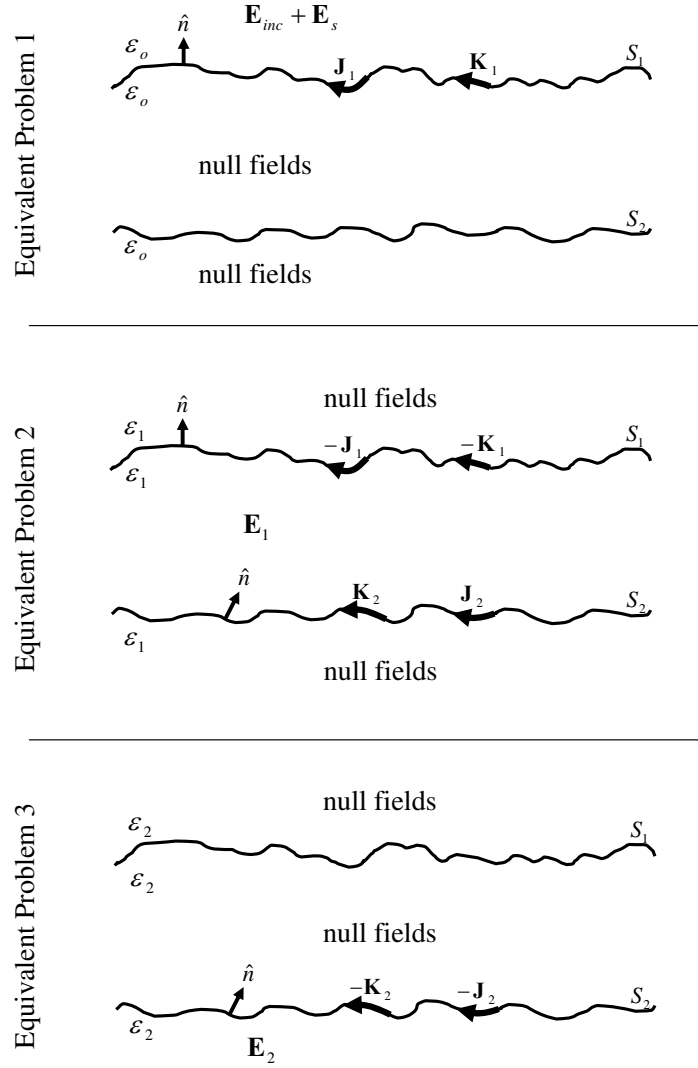
Figure 3.2: The three problems formulated based on the equivalence principle. Each equivalent problem gives the field in a different region, but the problems are solved simultaneously to find the surface currents.

The boundary conditions on S_1 state that

$$\hat{n} \times \mathbf{E}_{inc} = -\mathbf{K_1} - \hat{n} \times \mathbf{E}_s \qquad (3.1)$$

$$\mathbf{0} = \mathbf{K_1} + \hat{n} \times \mathbf{E}_1 \qquad (3.2)$$

$$\hat{n} \times \mathbf{H}_{inc} = \mathbf{J_1} - \hat{n} \times \mathbf{H}_s \qquad (3.3)$$

$$\mathbf{0} = -\mathbf{J_1} + \hat{n} \times \mathbf{H}_1 \qquad (3.4)$$

where $\mathbf{J_1}$ and $\mathbf{K_1}$ are, respectively, the equivalent electric and magnetic currents on S_1. Similarly, the boundary conditions on S_2 state that

$$\mathbf{0} = -\mathbf{K_2} - \hat{n} \times \mathbf{E}_1 \qquad (3.5)$$

$$\mathbf{0} = \mathbf{K_2} + \hat{n} \times \mathbf{E}_2 \qquad (3.6)$$

$$\mathbf{0} = \mathbf{J_2} - \hat{n} \times \mathbf{H}_1 \qquad (3.7)$$

$$\mathbf{0} = -\mathbf{J_2} + \hat{n} \times \mathbf{H}_2 \qquad (3.8)$$

where $\mathbf{J_2}$ and $\mathbf{K_2}$ are, respectively, the equivalent electric and magnetic currents on S_2. Note that (3.1) and (3.3) result from the first equivalent problem where the equivalent currents on S_1 produce the scattered field in the region of incidence and produce null fields in other regions. Likewise, (3.6) and (3.8) result from the third equivalent problem where the currents on S_2 produce $\mathbf{E_2}$ and $\mathbf{H_2}$ in Region 2 and produce null fields in other regions. Finally, (3.2), (3.4), (3.5), and (3.7) result from the second equivalent problem where the currents on S_1 and S_2 produce $\mathbf{E_1}$ and $\mathbf{H_1}$ in Region 1 and produce null fields in other regions.

We can find the unknown currents from either the electric or magnetic field boundary conditions. However, combining (3.1) with (3.2), (3.3) with (3.4), (3.5) with (3.6), and (3.7) with (3.8) will eliminate the interior resonance in the integral equations and will produce

more accurate results. The resulting set of equations is

$$\hat{n} \times \mathbf{E}_{inc} = -\hat{n} \times \mathbf{E}_s + \hat{n} \times \mathbf{E_1} \tag{3.9}$$

$$\hat{n} \times \mathbf{H}_{inc} = -\hat{n} \times \mathbf{H}_s + \hat{n} \times \mathbf{H_1} \tag{3.10}$$

$$\mathbf{0} = -\hat{n} \times \mathbf{E_1} + \hat{n} \times \mathbf{E_2} \tag{3.11}$$

$$\mathbf{0} = -\hat{n} \times \mathbf{H_1} + \hat{n} \times \mathbf{H_2} \tag{3.12}$$

These equations are known as the PMCHWT equations and have been applied to dielectric bodies previously.

3.3 Method of Moment Formulation

Mixed potential formulation is used to find the fields in each region, i.e.,

$$\mathbf{E} = i\omega\mu_o\mathbf{A} - \nabla\Phi_e - \nabla \times \mathbf{F} \tag{3.13}$$

$$\mathbf{H} = \nabla \times \mathbf{A} + i\omega\epsilon\mathbf{F} - \nabla\Phi_m \tag{3.14}$$

where, assuming that the boundaries are parameterized in t,

$$\mathbf{A} = \frac{i}{4} \int \mathbf{J}(t') H_0^{(1)}(kR) dt' \tag{3.15}$$

$$\mathbf{F} = \frac{i}{4} \int \mathbf{K}(t') H_0^{(1)}(kR) dt' \tag{3.16}$$

$$\Phi_e = \frac{i}{4} \int \frac{\rho_e(t')}{\epsilon} H_0^{(1)}(kR) dt' \tag{3.17}$$

$$\Phi_m = \frac{i}{4} \int \frac{\rho_m(t')}{\mu_o} H_0^{(1)}(kR) dt' \tag{3.18}$$

where $\mathbf{J}$ and $\mathbf{K}$ are the corresponding equivalent surface currents radiating in an unbounded, homogeneous space whose wave number is k. The function $H_0^{(1)}$ is the zeroth order Hankel function of the first kind and R is the distance between observation and integration points.

The quantities ρ_e and ρ_m are the equivalent surface charges related to the surface currents through the continuity equations

$$\nabla_s \cdot \mathbf{J} = i\omega\rho_e \qquad (3.19)$$

$$\nabla_s \cdot \mathbf{K} = i\omega\rho_m \qquad (3.20)$$

Assume that the incident field polarization is transverse magnetic to z (TM$_z$), i.e.,

$$\mathbf{E}_{inc} = \hat{z}E_{inc} = \hat{z}\exp[i\mathbf{k}_{inc} \cdot \boldsymbol{\rho}] \qquad (3.21)$$

where

$$\mathbf{k}_{inc} = k_0\left(\hat{x}\cos\phi_{inc} + \hat{y}\sin\phi_{inc}\right) \qquad (3.22)$$

where k_0 is the incidence region wavenumber and ϕ_{inc} is the incidence angle shown in Fig. 3.3. This figure also shows the vectors tangential and normal to the surface profiles. Noting that,
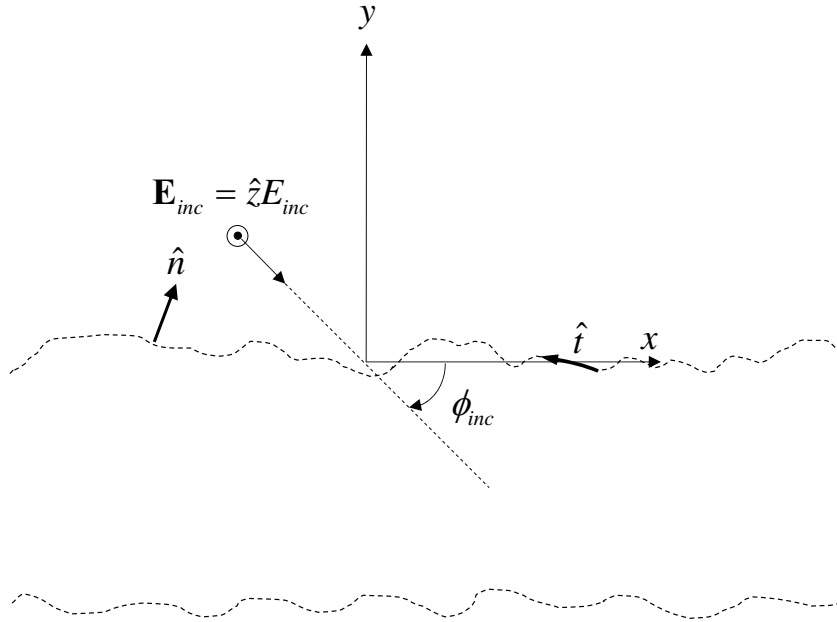
Figure 3.3: Geometry of the problem and the convention for incidence angle, tangential vector $\hat{t}$, and normal vector $\hat{n}$.

on the boundary, $-\hat{t} \cdot (\hat{n} \times \mathbf{E}) = E^z$ and $\hat{z} \cdot (\hat{n} \times \mathbf{H}) = H^t$, Equations (3.9)–(3.12) reduce to

$$E^z_{inc} = -E^z_s + E^z_1 \tag{3.23}$$

$$H^t_{inc} = -H^t_s + H^t_1 \tag{3.24}$$

$$0 = -E^z_1 + E^z_2 \tag{3.25}$$

$$0 = -H^t_1 + H^t_2 \tag{3.26}$$

which, using (3.15)–(3.18) and noting that $\hat{z} \cdot \nabla\Phi_e = 0$ in a z-invariant problem, can be written as

$$
\begin{aligned}
E^z_{inc} &= -ik_0\eta_0 A^z_0 + \hat{z} \cdot \nabla \times \mathbf{F}_0 \\
&+ ik_1\eta_1 A^z_1 - \hat{z} \cdot \nabla \times \mathbf{F}_1
\end{aligned}
\tag{3.27}
$$

$$
\begin{aligned}
-H^t_{inc} &= \hat{t} \cdot (\nabla \times \mathbf{A}_0 + i\omega\epsilon_0\mathbf{F}_0 - \nabla\Phi_{m0}) \\
&- \hat{t} \cdot (\nabla \times \mathbf{A}_1 + i\omega\epsilon_1\mathbf{F}_1 - \nabla\Phi_{m1})
\end{aligned}
\tag{3.28}
$$

$$
\begin{aligned}
0 &= -ik_1\eta_1 A^z_1 + \hat{z} \cdot \nabla \times \mathbf{F}_1 \\
&+ ik_2\eta_2 A^z_2 - \hat{z} \cdot \nabla \times \mathbf{F}_2
\end{aligned}
\tag{3.29}
$$

$$
\begin{aligned}
0 &= \hat{t} \cdot (\nabla \times \mathbf{A}_1 + i\omega\epsilon_1\mathbf{F}_1 - \nabla\Phi_{m1}) \\
&- \hat{t} \cdot (\nabla \times \mathbf{A}_2 + i\omega\epsilon_2\mathbf{F}_2 - \nabla\Phi_{m2})
\end{aligned}
\tag{3.30}
$$

The potential functions $\mathbf{A}_0$, $\mathbf{A}_1$, $\mathbf{A}_2$, $\mathbf{F}_0$, $\mathbf{F}_1$, $\mathbf{F}_2$, Φ_{m0}, Φ_{m1}, and Φ_{m2} are presented in Appendix B.2.

To solve (3.27)–(3.30) for the unknown currents using MoM, the boundaries should be discretized. To enforce the integral equations, testing functions will then be applied on (3.27)–(3.30). Pulse and triangle basis functions, as shown in Fig. (3.4), are used for electric
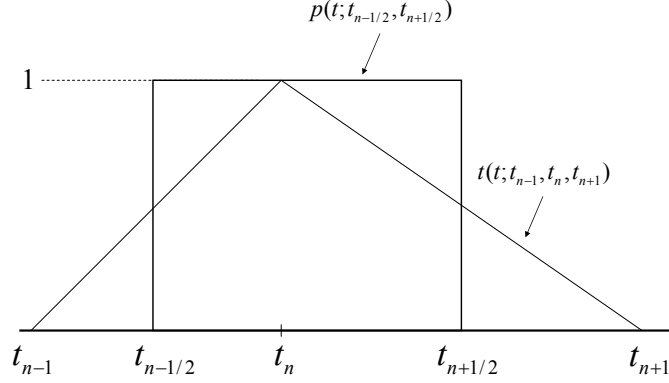
Figure 3.4: Pulse (p) and triangle (t) basis functions used to represent electric current J and magnetic current K, respectively.

and magnetic currents, respectively.

$$J_z(t) = \sum_{n=1}^{N} j_n p(t; t_{n-\frac{1}{2}}, t_{n+\frac{1}{2}}) \tag{3.31}$$

$$K_t(t) = \sum_{n=1}^{N} k_n t(t; t_{n-1}, t_n, t_{n+1}) \tag{3.32}$$

where N is the number of cells on the corresponding boundary. (Assume that the first and second boundaries are discretized using N_1 and N_2 cells, respectively.) It is apparent from the boundary conditions (3.9)–(3.12) and (3.21) that J_z and K_t are the only non-zero components of the electric and magnetic currents.

The derivation of the MoM formulation is presented below.

3.3.1 Derivation of the MoM Formulation

The formulation presented here is for a general medium and a general number of segments, denoted by N. Therefore, the terms in (3.27)–(3.30) can be expanded as follows.

The A^z terms in (3.27) and (3.29) can be written as

$$\int_S J_z(t')H_0^{(1)}(kR)dt' = \sum_{n=1}^{N} j_n I_n(t) \tag{3.33}$$

where

$$R = \sqrt{(x(t) - x(t'))^2 + (y(t) - y(t'))^2} \tag{3.34}$$

and

$$I_n(t) = \int_{t_{n-\frac{1}{2}}}^{t_{n+\frac{1}{2}}} H_0^{(1)}(kR)dt' \tag{3.35}$$

which can be written as

$$I_n(t) = I_{n1}(t) + I_{n2}(t) \tag{3.36}$$

where

$$I_{n1}(t) = \int_{t_{n-\frac{1}{2}}}^{t_n} H_0^{(1)}(kR)dt' \tag{3.37}$$

and

$$I_{n2}(t) = \int_{t_n}^{t_{n+\frac{1}{2}}} H_0^{(1)}(kR)dt' \tag{3.38}$$

Applying pulse testing functions on (3.33) would result in

$$\int_{t_{m-\frac{1}{2}}}^{t_{m+\frac{1}{2}}} \int_S J_z(t')H_0^{(1)}(kR)dt'dt \simeq \left(t_{m+\frac{1}{2}} - t_m\right) \sum_{n=1}^{N} j_n I_n(t_{m+\frac{1}{4}})$$

$$+ \left(t_m - t_{m-\frac{1}{2}}\right) \sum_{n=1}^{N} j_n I_n(t_{m-\frac{1}{4}}) \tag{3.39}$$

Note that $I_{n1}(t_{m-\frac{1}{4}})$ and $I_{n2}(t_{m+\frac{1}{4}})$ are singular integrals if $m = n$; it can be shown that as the cell length approaches 0,

$$I_{m1}(t_{m-\frac{1}{4}}) \sim (t_m - t_{m-\frac{1}{2}}) \left(1 + i\frac{2}{\pi}\left[\ln\left(\gamma k(t_m - t_{m-\frac{1}{2}})/4\right) - 1\right]\right) + O\left((t_m - t_{m-\frac{1}{2}})^3\right) \tag{3.40}$$

and

$$I_{m2}(t_{m+\frac{1}{4}}) \sim (t_{m+\frac{1}{2}} - t_m) \left(1 + i\frac{2}{\pi}\left[\ln\left(\gamma k(t_{m+\frac{1}{2}} - t_m)/4\right) - 1\right]\right) + O\left((t_{m+\frac{1}{2}} - t_m)^3\right) \tag{3.41}$$

48

where $\gamma = 1.781072418....$

Likewise, the $\hat{t} \cdot \nabla \times \mathbf{A}$ terms in (3.28) and (3.30) can be written as

$$
\begin{aligned}
-\hat{t} \cdot \nabla \times \int_S \mathbf{J}(t') H_0^{(1)}(kR) dt' &= -k \int_S J_z(t') \left(\cos \phi(t) \frac{\Delta x}{R} + \sin \phi(t) \frac{\Delta y}{R} \right) H_1^{(1)}(kR) dt' \\
&= -k \sum_{n=1}^{N} j_n I_n(t)
\end{aligned}
\tag{3.42}
$$

where

$$
I_n(t) = \int_{t_{n-\frac{1}{2}}}^{t_{n+\frac{1}{2}}} dt' \left(\cos \phi(t) \frac{\Delta x}{R} + \sin \phi(t) \frac{\Delta y}{R} \right) H_1^{(1)}(kR)
\tag{3.43}
$$

which can be written as

$$
I_n(t) = I_{n1}(t) + I_{n2}(t)
\tag{3.44}
$$

where

$$
I_{n1}(t) = \int_{t_{n-\frac{1}{2}}}^{t_n} dt' \left(\cos \phi(t) \frac{\Delta x}{R} + \sin \phi(t) \frac{\Delta y}{R} \right) H_1^{(1)}(kR)
\tag{3.45}
$$

and

$$
I_{n2}(t) = \int_{t_n}^{t_{n+\frac{1}{2}}} dt' \left(\cos \phi(t) \frac{\Delta x}{R} + \sin \phi(t) \frac{\Delta y}{R} \right) H_1^{(1)}(kR)
\tag{3.46}
$$

Note that $\hat{t} = -\hat{x} \sin \phi(t) + \hat{y} \cos \phi(t)$ where the quantity $\phi(t)$ describes the orientation of the tangential vector $\hat{t}$ as shown in Fig. 3.5.

Applying pulse testing functions on (3.42) would result in

$$
\begin{aligned}
\int_{t_{m-\frac{1}{2}}}^{t_{m+\frac{1}{2}}} \hat{t} \cdot \nabla \times \int_S \mathbf{J}(t') H_0^{(1)}(kR) dt' dt &\simeq \left(t_m - t_{m-\frac{1}{2}} \right) k \sum_{n=1}^{N} j_n I_n(t_{m-\frac{1}{4}}) \\
&+ \left(t_{m+\frac{1}{2}} - t_m \right) k \sum_{n=1}^{N} j_n I_n(t_{m+\frac{1}{4}})
\end{aligned}
\tag{3.47}
$$

Note that $I_{n1}(t_{m-\frac{1}{4}})$ and $I_{n2}(t_{m+\frac{1}{4}})$ are singular integrals if $m = n$; it can be shown that $-(ik/4)I_{m1}(t) \rightarrow -1/2$ and $-(ik/4)I_{m2}(t) \rightarrow -1/2$ as $t \rightarrow t_{m-\frac{1}{4}}$ and $t \rightarrow t_{m+\frac{1}{4}}$, respectively.

The $\hat{z} \cdot \nabla \times \mathbf{F}$ terms in (3.27) and (3.29) can be written as
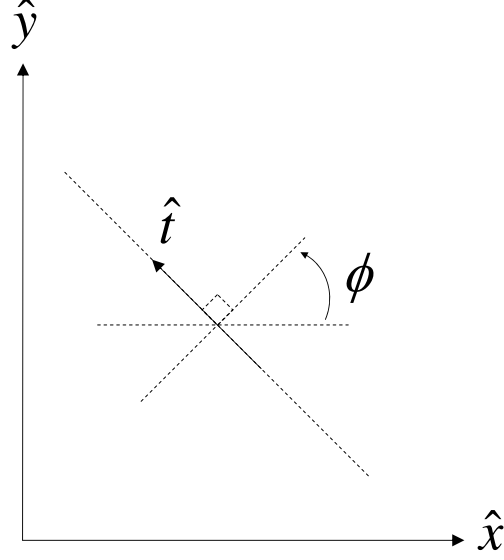
Figure 3.5: Orientation of a tangential vector is represented by the angle ϕ.

$$
\begin{aligned}
\hat{z} \cdot \nabla \times \int_S \mathbf{K}(t') H_0^{(1)}(kR) dt' &= -k \int K_t(t') \left(\cos\phi(t') \frac{\Delta x}{R} + \sin\phi(t') \frac{\Delta y}{R} \right) H_1^{(1)}(kR) dt' \\
&= -k \sum_{n=1}^{N} k_n I_n(t) \quad\quad (3.48)
\end{aligned}
$$

where $\Delta x = x(t) - x(t')$, $\Delta y = y(t) - y(t')$, and

$$
\begin{aligned}
I_n(t) &= \int_{t_{n-1}}^{t_{n+1}} dt' \left(\cos\phi(t') \frac{\Delta x}{R} + \sin\phi(t') \frac{\Delta y}{R} \right) t(t'; t_{n-1}, t_n, t_{n+1}) H_1^{(1)}(kR) \quad (3.49) \\
&= \int_{t_{n-1}}^{t_n} dt' \left(\cos\phi(t') \frac{\Delta x}{R} + \sin\phi(t') \frac{\Delta y}{R} \right) t(t'; t_{n-1}, t_n, t_{n+1}) H_1^{(1)}(kR) \\
&+ \int_{t_n}^{t_{n+1}} dt' \left(\cos\phi(t') \frac{\Delta x}{R} + \sin\phi(t') \frac{\Delta y}{R} \right) t(t'; t_{n-1}, t_n, t_{n+1}) H_1^{(1)}(kR)
\end{aligned}
$$

which can be approximated as

$$
I_n(t) \simeq I_{n1}(t) + I_{n2}(t) \quad\quad (3.50)
$$

where

$$I_{n1}(t) = \int_{t_{n-\frac{1}{2}}}^{t_n} dt' \left(\cos\phi(t') \frac{\Delta x}{R} + \sin\phi(t') \frac{\Delta y}{R} \right) H_1^{(1)}(k_i R) \qquad (3.51)$$

and

$$I_{n2}(t) = \int_{t_n}^{t_{n+\frac{1}{2}}} dt' \left(\cos\phi(t') \frac{\Delta x}{R} + \sin\phi(t') \frac{\Delta y}{R} \right) H_1^{(1)}(k_i R) \qquad (3.52)$$

Applying pulse testing functions on (3.48) would result in

$$\int_{t_{m-\frac{1}{2}}}^{t_{m+\frac{1}{2}}} \hat{z} \cdot \nabla \times \int_S \mathbf{K}(t') H_0^{(1)}(kR) dt' dt \simeq -\left(t_m - t_{m-\frac{1}{2}} \right) k \sum_{n=1}^{N} k_n I_n(t_{m-\frac{1}{4}})$$

$$-\left(t_{m+\frac{1}{2}} - t_m \right) k \sum_{n=1}^{N} k_n I_n(t_{m+\frac{1}{4}}) \qquad (3.53)$$

Note that $I_{n1}(t_{m-\frac{1}{4}})$ and $I_{n2}(t_{m+\frac{1}{4}})$ are singular integrals if $m = n$; it can be shown that $-(ik/4)I_{m1}(t) \to -1/2$ and $-(ik/4)I_{m2}(t) \to -1/2$ as $t \to t_{m-\frac{1}{4}}$ and $t \to t_{m+\frac{1}{4}}$, respectively. Similarly, it can be shown that the $\hat{t} \cdot \mathbf{F}$ terms in (3.28) and (3.30) can be written as

$$\hat{t} \cdot \int_S \mathbf{K}(t') H_0^{(1)}(kR) dt' = \int_S \cos(\phi(t) - \phi(t')) K_t(t') H_0^{(1)}(kR) dt' = \sum_{n=1}^{N} k_n I_n(t) \qquad (3.54)$$

where

$$\begin{aligned} I_n(t) &= \int_{t_{n-1}}^{t_{n+1}} \cos(\phi(t) - \phi(t')) t(t'; t_{n-1}, t_n, t_{n+1}) H_0^{(1)}(kR) dt' \qquad (3.55) \\ &= \int_{t_{n-1}}^{t_n} \cos(\phi(t) - \phi(t')) t(t'; t_{n-1}, t_n, t_{n+1}) H_0^{(1)}(kR) dt' \\ &+ \int_{t_n}^{t_{n+1}} \cos(\phi(t) - \phi(t')) t(t'; t_{n-1}, t_n, t_{n+1}) H_0^{(1)}(kR) dt' \end{aligned}$$

which can be approximated as

$$I_n(t) \simeq I_{n1}(t) + I_{n2}(t) \qquad (3.56)$$

where

$$I_{n1}(t) = \int_{t_{n-\frac{1}{2}}}^{t_n} \cos(\phi(t) - \phi(t')) H_0^{(1)}(kR) dt' \qquad (3.57)$$

and

$$I_{n2}(t) = \int_{t_n}^{t_{n+\frac{1}{2}}} \cos(\phi(t) - \phi(t')) H_0^{(1)}(kR) dt' \tag{3.58}$$

Applying pulse testing function on (3.54) would result in

$$\int_{t_{m-\frac{1}{2}}}^{t_{m+\frac{1}{2}}} \hat{t} \cdot \int_S \mathbf{K}(t') H_0^{(1)}(kR) dt' dt \simeq \left(t_m - t_{m-\frac{1}{2}}\right) \sum_{n=1}^{N} k_n I_n\left(t_{m-\frac{1}{4}}\right)$$
$$+ \left(t_{m+\frac{1}{2}} - t_m\right) \sum_{n=1}^{N} k_n I_n\left(t_{m+\frac{1}{4}}\right) \tag{3.59}$$

Note that $I_{n1}(t_{m-\frac{1}{4}})$ and $I_{n2}(t_{m+\frac{1}{4}})$ are singular integrals if $m = n$; it can be shown that

$$I_{m1}(t_{m-\frac{1}{4}}) \sim (t_m - t_{m-\frac{1}{2}})\left(1 + i\frac{2}{\pi}\left[\ln\left(\gamma k(t_m - t_{m-\frac{1}{2}})/4\right) - 1\right]\right) + O\left((t_m - t_{m-\frac{1}{2}})^3\right) \tag{3.60}$$

and

$$I_{m2}(t_{m+\frac{1}{4}}) \sim (t_{m+\frac{1}{2}} - t_m)\left(1 + i\frac{2}{\pi}\left[\ln\left(\gamma k(t_{m+\frac{1}{2}} - t_m)/4\right) - 1\right]\right) + O\left((t_{m+\frac{1}{2}} - t_m)^3\right) \tag{3.61}$$

where $\gamma = 1.781072418....$

Finally, the $\hat{t} \cdot \nabla \Phi_m$ terms in (3.28) and (3.30) can be written as

$$\hat{t} \cdot \nabla \Phi_m = \frac{\partial \Phi_m}{\partial t} \tag{3.62}$$

Therefore, applying pulse testing function on (3.62) would result in

$$\int_{t_{m-\frac{1}{2}}}^{t_{m+\frac{1}{2}}} \hat{t} \cdot \nabla \Phi_m dt' = \Phi_m(t_{m+\frac{1}{2}}) - \Phi_m(t_{m-\frac{1}{2}}) \tag{3.63}$$

Assuming
$$\Phi_m(t) = \frac{i}{4} \int_S \frac{\rho_m(t')}{\mu_0} H_0^{(1)}(kR) dt' = \frac{1}{4\omega\mu_0} \int_S \frac{dK_t}{dt'} H_0^{(1)}(kR) dt' \tag{3.64}$$

and noting that, from (3.32),

$$\frac{dK_t}{dt} = \sum_{n=1}^{N} k_n \left(\frac{p(t; t_{n-1}, t_n)}{t_n - t_{n-1}} - \frac{p(t; t_n, t_{n+1})}{t_{n+1} - t_n}\right) \tag{3.65}$$

we will have

$$\Phi_m(t) = \frac{1}{4\omega\mu_0} \sum_{n=1}^{N} k_n \left[\frac{1}{t_n - t_{n-1}} \int_{t_{n-1}}^{t_n} H_0^{(1)}(kR)dt' - \frac{1}{t_{n+1} - t_n} \int_{t_n}^{t_{n+1}} H_0^{(1)}(kR)dt' \right] \quad (3.66)$$

Note that $\Phi_m(t_{m-\frac{1}{2}})$ and $\Phi_m(t_{m+\frac{1}{2}})$ include singular integrals when $m = n$. These singular integrals are handled similar to (3.40), (3.41), (3.60), and (3.61).

Applying the testing functions on E_{inc}^z and H_{inc}^t is simple and is done via numerical integration.

After completing the discretization and testing the equation, the system of equations can be expressed as a $2(N_1 + N_2) \times 2(N_1 + N_2)$ matrix equation.

$$\mathbf{Z} \begin{bmatrix} \mathbf{J}_{1z} \\ \mathbf{K}_{1t} \\ \mathbf{J}_{2z} \\ \mathbf{K}_{2t} \end{bmatrix} = \begin{bmatrix} \mathbf{E}_{inc}^z \\ \mathbf{H}_{inc}^t \\ \mathbf{0} \\ \mathbf{0} \end{bmatrix} \quad (3.67)$$

where the mth elements of $\mathbf{E}_{inc}^z$ and $\mathbf{H}_{inc}^t$ are respectively found by testing (3.27) and (3.28) with $p(t; t_{m-\frac{1}{2}}, t_{m+\frac{1}{2}})$. The elements of the vectors $\mathbf{J}_{1z}$, $\mathbf{K}_{1t}$, $\mathbf{J}_{2z}$, and $\mathbf{K}_{2t}$ are the electric and magnetic currents on the corresponding cell. The matrix $\mathbf{Z}$ denotes the impedance matrix.

Once the surface currents are found, they are used to calculate the scattering coefficients of the rough surface structure. In numerical simulations, the rough surfaces are finite, and if the surface currents suddenly change from non-zero to zero at the end points of the rough surfaces, artificial reflections occur. Therefore, a tapered incident wave is used so that the incident wave would decay to zero gradually [64]. A possible choice for tapered incident wave is [58]

$$E_{inc}^z = \exp\left(ik_0\left(x\cos\phi_{inc} + y\sin\phi_{inc}\right)(1 + w(\boldsymbol{\rho}))\right)\exp\left(-\frac{(x - y\cot\phi_{inc})^2}{g^2}\right) \quad (3.68)$$

where g is the tapering parameter and is usually between $L/4$ and $L/10$ depending on the

incidence angle. The incident wave vector is given by (3.22). The choice of $w(\boldsymbol{\rho})$ is

$$w(\boldsymbol{\rho}) = \frac{\left[2\dfrac{(x - y \cot \phi_{inc})^2}{g^2} - 1\right]}{(k_0 g \sin \phi_{inc})^2} \tag{3.69}$$

The bistatic scattering coefficient of the rough surface structure is given by [64]

$$\sigma(\phi_s) = \frac{\dfrac{1}{2\eta_0} \dfrac{1}{8\pi k_0} \left|\psi_s^{(N)}(\phi_s)\right|^2}{P_{inc}} \tag{3.70}$$

where, for TM incidence, $\psi_s^{(N)}(\phi_s)$ can be shown to be

$$\psi_s^{(N)}(\phi_s) = -\int_{S_1} ds \left(ik_0\eta_0 J_{1z} + ik_0 K_{1t}\frac{f'(x)\cos\phi_s - \sin\phi_s}{\sqrt{1 + f'(x)^2}}\right)$$
$$\times \exp\left[-ik_0\left(x\cos\phi_s + f(x)\sin\phi_s\right)\right] \tag{3.71}$$

P_{inc} is defined as

$$P_{inc} = -\int_{S_1} dx \mathbf{S}_{inc} \cdot \hat{y} \tag{3.72}$$

where $\mathbf{S}_{inc}$ is the incident Poynting vector. If the incident wave is tapered, it can be shown that

$$\sigma(\phi_s) = -\frac{\left|\psi_s^{(N)}(\phi_s)\right|^2}{8\pi k_0 g\sqrt{\dfrac{\pi}{2}}\sin\phi_{inc}\left[1 - \dfrac{1 + 2\cot^2\phi_{inc}}{2k_0^2 g^2 \sin^2\phi_{inc}}\right]} \tag{3.73}$$

Appendix B.3 describes in detail how (3.71) is derived.

3.4 Relation Between Bistatic Scattering Coefficients from 2D SPM and 2D MoM

Let's first investigate how 3D SPM formulation can be used to calculate the bistatic scattering coefficient of a 2D rough surface structure. The formulation presented here is in fact the 2D version of the formulation presented in Chapter 2.

3.4.1 Use of 3D SPM Formulation in a 2D Scattering Problem

The power spectral density of $f(x)$, representing a 1D random rough surface, is defined as

$$W(k_x) := \sigma^2 \mathscr{F}\{C(x)\} = \frac{\sigma^2}{2\pi} \int_{-\infty}^{+\infty} C(x) \exp\left(-ik_x x\right) dx \tag{3.74}$$

where $C(x)$ is defined in Appendix B.1 and $f(x)$ is assumed to have all of the properties mentioned in Appendix B.1. It can be shown that

$$W(k_x) = 2\pi \lim_{L\to\infty} \frac{\left\langle |F(k_x)|^2 \right\rangle}{L} \tag{3.75}$$

where

$$F(k_x) = \int_{-L/2}^{L/2} f(x) \exp\left[-ik_x x\right] dx \tag{3.76}$$

Since the formulation presented here is the 2D version of the formulation presented in Chapter 2, we assume the plane of incidence is the x-z plane. Therefore, the 2D version of (2.62) can be written as

$$\mathbf{E}_{\mathbf{s}}^{(\mathbf{1})}(\boldsymbol{\rho}) = \xi \int dk_x \left[a_h^{+(1)}(k_x)\hat{h}(k_{0z}) + a_v^{+(1)}(k_x)\hat{v}(k_{0z}) \right] e^{i\mathbf{k}\cdot\boldsymbol{\rho}} \tag{3.77}$$

where $\mathbf{k} \cdot \boldsymbol{\rho} = k_{0z}z + k_x x$. The asymptotic expansion of the integral as $\mathbf{k} \cdot \boldsymbol{\rho} \to \infty$ (far-field region) is found using the stationary phase method. The stationary point can be found by solving

$$\frac{\partial \mathbf{k} \cdot \boldsymbol{\rho}}{\partial k_x} = \frac{\partial\left(k_x x + k_{0z}z\right)}{\partial k_x} = 0 \tag{3.78}$$

The solution to (3.78) is $k_x^s = k_0 \cos\phi_s$, where ϕ_s is the observation (scattering) direction. Therefore,

$$\mathbf{k} \cdot \boldsymbol{\rho} \simeq k_0\rho - \frac{\rho}{2k_0 \sin^2\phi_s}\left(k_x - k_x^s\right)^2 \tag{3.79}$$

The electric field in (3.77) can then be expanded as

$$\mathbf{E_s^{(1)}}(\boldsymbol{\rho}) \sim \xi \left(a_h^{+(1)}(k_x^s)\hat{h}(k_{0z}^s) + a_v^{+(1)}(k_x^s)\hat{v}(k_{0z}^s) \right) e^{ik_0\rho}$$
$$\times \int_{-\infty}^{\infty} \exp\left[-i\frac{\rho}{2k_0 \sin^2\phi_s}(k_x - k_x^s)^2 \right] dk_x \tag{3.80}$$

It can easily be shown that

$$\mathbf{E_s^{(1)}}(\boldsymbol{\rho}) \sim \xi\sqrt{2\pi k_0}e^{-i\frac{\pi}{4}} \left(a_h^{+(1)}(k_x^s)\hat{h}(k_{0z}^s) + a_v^{+(1)}(k_x^s)\hat{v}(k_{0z}^s) \right) \sin\phi_s \frac{e^{ik_0\rho}}{\sqrt{\rho}} \tag{3.81}$$

The bistatic scattering coefficient for 1D rough surfaces is defined as

$$\gamma_{pq}^{2D}(\hat{k}_i, \hat{k}_s) = -\lim_{L\to\infty} \lim_{\rho\to\infty} \frac{2\pi\rho}{L\cos\theta_i} \left\langle \left| \mathbf{E_s^{(1)}}(\boldsymbol{\rho}) \cdot \hat{p}(k_{0z}^s) \right|^2 \right\rangle \tag{3.82}$$

where $p, q \in \{v, h\}$ and the incident field is assumed to be $\hat{q}(-k_{0z}^i)$. The incidence angle θ_i is defined according to the convention in Chapter 2. See Fig. 2.1.

Similar to the 2D rough surface case,

$$a_h^{+(1)}(k_x) = \alpha_h^{f_1}(k_x)F_1(k_x - k_x^i) + \alpha_h^{f_2}(k_x)F_2(k_x - k_x^i) \tag{3.83}$$

$$a_v^{+(1)}(k_x) = \alpha_v^{f_1}(k_x)F_1(k_x - k_x^i) + \alpha_v^{f_2}(k_x)F_2(k_x - k_x^i) \tag{3.84}$$

Inserting (3.83) and (3.84) in (3.81) and using (3.75), the bistatic scattering coefficient given by (3.82) will reduce to

$$\gamma_{pq}^{2D}(\hat{k}_i, \hat{k}_s) = 2\pi k_0 \frac{\sin^2\phi_s}{|\sin\phi_{inc}|}\xi^2 \sum_{i=1}^{2} \left| \alpha_{pq}^{f_i}(k_x^s) \right|^2 W_{f_i}(k_x^s - k_x^i) \tag{3.85}$$

where $\alpha_{pq}(k_x^s) = \alpha_p(k_x^s)|_{\mathbf{E}_i=\hat{q}(-k_{0z}^i)}$. These coefficients can be calculated by setting $k_y^i = k_y^s = 0$ in the calculation of $\alpha_{pq}(\mathbf{k}_\perp^s)$ in 3D SPM. Therefore, by comparing (3.85) with (2.66) and assuming that the two rough surfaces are not correlated,

$$\gamma_{pq}^{2D}(\hat{k}_i, \hat{k}_s) = \frac{1}{2k_0}\gamma_{pq}^{3D}(\hat{k}_i, \hat{k}_s)|_{k_y^i=0, k_y^s=0} \tag{3.86}$$

where, assuming Gaussian correlation functions for the 1D and 2D cases, $W(\mathbf{k}_\perp)$ in (2.66) has been replaced by $\frac{2\sqrt{\pi}}{l}W(\mathbf{k}_\perp)$. Note that in the 3D problem, the incidence direction is described by θ_i and in the 2D problem, the incidence direction is described by ϕ_{inc}, which is a negative number. It is clear that $-\phi_{inc} = \theta_i - \frac{\pi}{2}$. We should also note the difference between σ^o_{pq} in (2.66) and γ^{3D}_{pq} in (3.86). Conventionally, $\sigma^o_{pq} = -\gamma^{3D}_{pq}\cos\theta_i = -\gamma^{3D}_{pq}\sin\phi_{inc}$.

We should now investigate the relation between the bistatic scattering coefficient calculated by (3.73) and (3.86). This relation is necessary in order to compare the numerical result with the analytical solution. To see how (3.73) (or equivalently (3.70)) and (3.86) (or equivalently (3.82)) are related, the incident wave is assumed to be a plane wave.

$$\mathbf{E}_{inc} = \hat{z}E_{inc} = \hat{z}\exp[i\mathbf{k}_{inc}\cdot\boldsymbol{\rho}] \tag{3.87}$$

where

$$\mathbf{k}_{inc} = k_0\left(\hat{x}\cos\phi_{inc} + \hat{y}\sin\phi_{inc}\right) \tag{3.88}$$

where k_0 is the incidence region wavenumber and ϕ_{inc} is the incidence angle shown in Fig. 3.3. Therefore,

$$S_{inc} = \frac{1}{2\eta_0} \tag{3.89}$$

where S_{inc} is the magnitude of the incident Poynting vector. According to (3.72) the incident power is

$$P_{inc} = -\int_{-\infty}^{\infty} dx\frac{1}{2\eta_0}\sin\phi_{inc} = -\lim_{L\to\infty}S_{inc}L\sin\phi_{inc} \tag{3.90}$$

The bistatic scattering coefficient, as determined by (3.70), is

$$\sigma(\phi_s) = -\lim_{L\to\infty}\frac{\frac{1}{2\eta_0}\frac{1}{8\pi k_0}\left|\psi_s^{(N)}(\phi_s)\right|^2}{S_{inc}L\sin\phi_{inc}} \tag{3.91}$$

Since, according to [64], the scattered Poynting vector in the far-field region is

$$\mathbf{S}_s = \frac{\hat{\boldsymbol{\rho}}}{2\eta_0}\left(\frac{1}{8\pi k_0\rho}\right)\left|\psi_s^{(N)}(\phi_s)\right|^2 \tag{3.92}$$

we can rewrite (3.91) as

$$\sigma(\phi_s) = \lim_{\rho \to \infty} \lim_{L \to \infty} \frac{1}{2\pi} \frac{2\pi\rho}{L |\sin \phi_{inc}|} \frac{S_s}{S_{inc}} \qquad (3.93)$$

Comparing (3.93) with (3.82) would lead to

$$\sigma(\phi_s) = \frac{\gamma_{pq}^{2D}}{2\pi} \qquad (3.94)$$

3.5 MoM Numerical Results

To validate the MoM solution, the solution of (3.67) is compared with the solution found from Chapter 2. Consider a two-layer dielectric structure with the model parameters shown in Table 3.1 where N_1 and N_2 denote the number of cells on the first and second boundary, respectively, and f denotes the frequency. Note that all of the parameters are in SI units. Fig. 3.6 shows comparisons between SPM and MoM solutions. It is clear from the plots that for very smooth surfaces (Case 1), the MoM and SPM solutions agree well while when the second boundary becomes rougher (Case 2), these solution do not agree.

Table 3.1: The model parameters of the structures simulated with SPM and MoM. The results of simulations are shown in Fig. 3.6.

	ϵ'_{1r}	ϵ'_{2r}	d	l_{f_1}	σ_{f_1}	l_{f_2}	σ_{f_2}	N_1	N_2	f (MHz)
Case 1	$2.0 + i0.01$	$4.0 + i0.02$	0.3	0.2	0.01	0.2	0.01	750	1000	300
Case 2	$2.0 + i0.01$	$4.0 + i0.02$	0.3	0.2	0.01	0.2	0.05	750	1000	300

The significant discrepancy between the MoM and SPM solutions for scattering angles around the specular direction is due to the fact that the first order SPM solution is incoherent and does not include the specular peak. The disagreement between the MoM and SPM solutions in the backscattering direction in Fig. 3.6(b) implies that we should study the region of validity of the SPM for a two-layer structure. To derive the region of validity of the SPM formulation of Chapter 2, we need to systematically compare the SPM solution to the numerical solution derived above. To this end, we need a fast solver of the matrix equation (3.67). In what follows, the fast solver employed in this chapter is described.
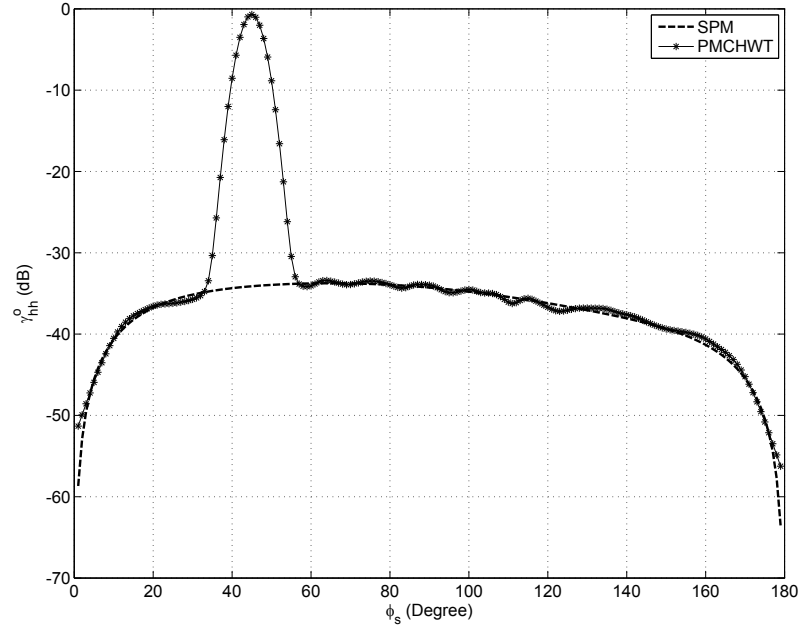
(a) $\sigma_{f_2} = 0.01$
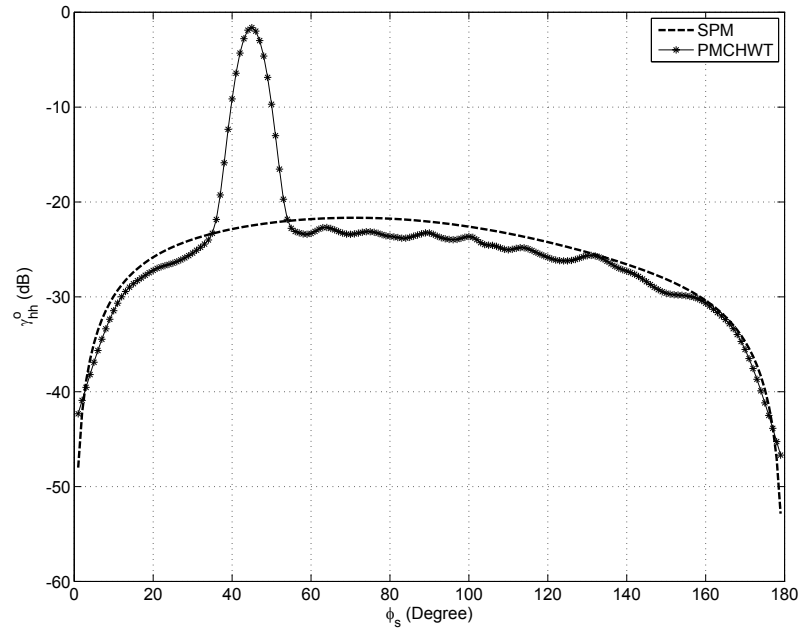
(b) $\sigma_{f_2} = 0.05$

Figure 3.6: Comparison between SPM and MoM solutions for two cases presented in Table 3.1. When both surfaces are smooth, the SPM and MoM solutions show good agreements, but when one or both of the surfaces become rough, these solutions do not agree.

3.6 Fast Solver

The idea behind a fast solver of a matrix equation such as (3.67) is to accelerate the product of a matrix and a vector. The fast solver employed in this work is based on the UV Multilevel Partitioning Method (UV-MLP) [55]. In a UV decomposition, an N by N matrix is decomposed as

$$\mathbf{A} = \mathbf{U} \times \mathbf{V} \tag{3.95}$$

where $\mathbf{U}$ is an N by r and $\mathbf{V}$ is an r by N matrix. The quantity r is the rank of $\mathbf{A}$. The computational cost of the direct product of $\mathbf{A}$ and a vector is $O(N^2)$, but if we multiply a vector by $\mathbf{V}$ and multiply the result by $\mathbf{U}$, the computational cost will be $O(2rN)$. Therefore, if $r \ll N$, the computational cost reduces significantly.

In the following subsections, the theory of UV decomposition of a matrix and the Multilevel Partitioning Method are presented.

3.6.1 UV Decomposition

Assume that the rank of an N by N matrix $\mathbf{A}$ is r and denote the independent columns of $\mathbf{A}$ by $\bar{u}_l$ where $1 \leq l \leq r$. These columns form an N by r matrix $\mathbf{U}$ with elements u_{il}.

$$u_{il} = (\bar{u}_l)_i \tag{3.96}$$

where $1 \leq i \leq N$. The quantity $(\bar{u}_l)_i$ is the ith element of the column vector $\bar{u}_l$. Since $\{\bar{u}_l\}$ are independent, any column of $\mathbf{A}$ can be written as a linear combination of $\{\bar{u}_l\}$ as

$$\bar{a}_j = \sum_{l=1}^{r} v_{lj} \bar{u}_l \tag{3.97}$$

Equivalently,

$$a_{ij} = \sum_{l=1}^{r} u_{il} v_{lj} \tag{3.98}$$

Equation (3.98) can be reformulated as

$$\mathbf{A} = \mathbf{U} \times \mathbf{V} \tag{3.99}$$

where $\mathbf{V}$ is an r by N matrix with elements v_{lj} introduced in (3.97). To find $\mathbf{V}$, note that according to (3.98),

$$\bar{a}_i = \sum_{l=1}^{r} u_{il} \bar{v}_l \tag{3.100}$$

where $\bar{a}_i$ is the ith row of $\mathbf{A}$ and $\bar{v}_l$ is the lth row of $\mathbf{V}$. Assuming the r independent rows of $\mathbf{A}$ form a matrix $\widetilde{\mathbf{V}}$, the ith row of $\widetilde{\mathbf{V}}$, denoted by $\bar{\tilde{v}}_i$, can be presented as

$$\bar{\tilde{v}}_i = \sum_{l=1}^{r} u_{m(i)l} \bar{v}_l \tag{3.101}$$

where $1 \le i \le r$ and $m(i)$ maps the row index i of $\widetilde{\mathbf{V}}$ to the corresponding row index of $\mathbf{A}$ according to (3.100). For example, if the fifth row of $\mathbf{A}$ is the third row of $\widetilde{\mathbf{V}}$, then $m(3) = 5$. Equation (3.101) can equivalently be written as

$$\widetilde{v}_{ij} = \sum_{l=1}^{r} u_{m(i)l} v_{lj} \tag{3.102}$$

which can be reformulated as

$$\widetilde{\mathbf{V}} = \mathbf{W} \times \mathbf{V} \tag{3.103}$$

where the r by r matrix $\mathbf{W}$ can be thought of as the intersection of $\mathbf{U}$ and $\widetilde{\mathbf{V}}$. Finally, from (3.99),

$$\mathbf{A} = \mathbf{U}\mathbf{V} = \mathbf{U}\mathbf{W}^{-1}\widetilde{\mathbf{V}} \tag{3.104}$$

To summarize the process, if the rank of $\mathbf{A}_{N \times N}$ is r, the independent columns form $\mathbf{U}_{N \times r}$ and the independent rows form $\widetilde{\mathbf{V}}_{r \times N}$. If $\mathbf{W}_{r \times r}$ is the intersection of these two matrices, $\mathbf{A}$ can be decomposed as in (3.104). Fig. 3.7 visualizes the process.
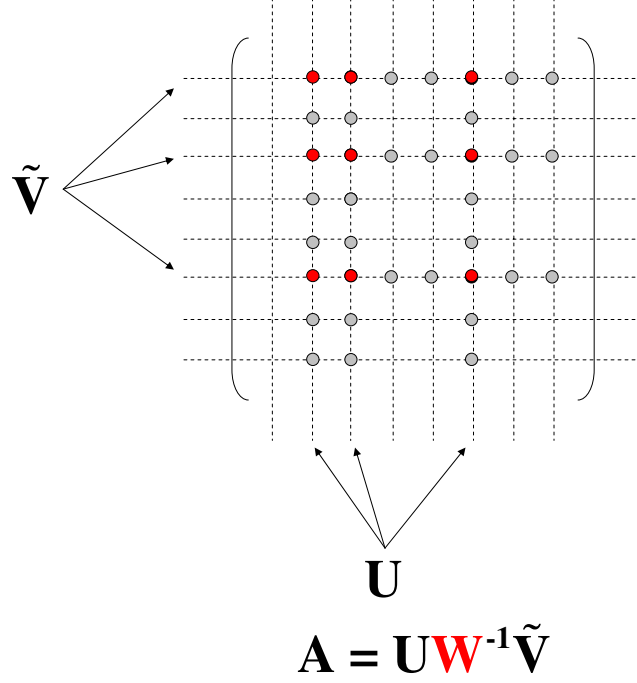
Figure 3.7: UV decomposition of a matrix. The red elements form the intersection matrix **W**.

3.6.2 Multilevel Partitioning

In UV-MLP, a matrix is decomposed to multilevel blocks as shown in Fig. 3.8. Block size is smaller for the blocks closer to the diagonal. Each of the blocks, except for the diagonal blocks, which are full-rank matrices, is decomposed to a **UV** product using the method mentioned in the previous subsection. The algorithm that is used in this chapter to determine the rank of a block is as follows.

Let's start with r_o as an initial guess at the rank of the block. The block rows and columns are sampled to form the intersection matrix **W**. The rank of **W**, denoted by r, is determined using the singular value decomposition (SVD) of **W**. To determine the rank of an N by N matrix using SVD, assume the singular values of the matrix are σ_1, $\sigma_2, \ldots, \sigma_N$ where $\sigma_1 \geq \sigma_2 \geq \ldots \geq \sigma_N$. The rank of the matrix is determined to be r if

$$\frac{\sigma_{r+1}}{\sigma_1} < \varepsilon \tag{3.105}$$
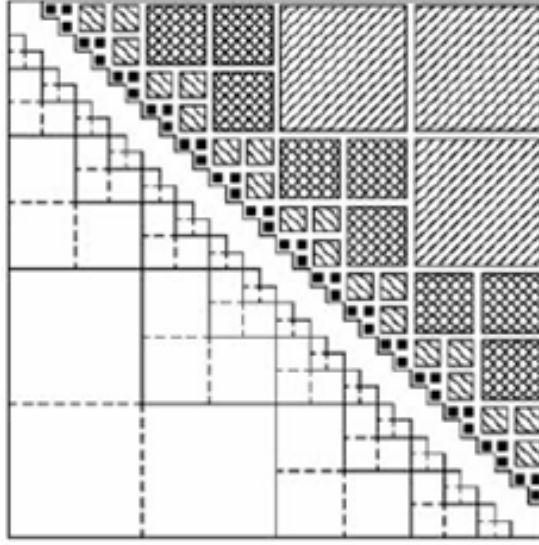
Figure 3.8: Multilevel partitioning of a matrix [55].

where ε is the accuracy used to determine the rank. The above process is repeated N_{r_o} times and the largest rank r is called r_m. Three cases might happen:

1- If r_m and r_o are equal, it means that there might be more independent rows and columns that have not been sampled. So we increase r_o by 1, i.e., $r_o = r_o + 1$, and repeat the above process with the new r_o.

2- If $r_m = r_o - 1$, we determine the rank of the block as r_m.

3- If $r_m < r_o - 1$, it means that so many rows and columns have been sampled. So we decrease r_o by 1, i.e., $r_o = r_o - 1$, and repeat the above process with the new r_o.

According to (3.9)–(3.12), the matrix equation (3.67) can also be presented as

$$
\begin{bmatrix}
\mathbf{Z}_{ej_1}^{s_1} & \mathbf{Z}_{ek_1}^{s_1} & \mathbf{Z}_{ej_2}^{s_1} & \mathbf{Z}_{ek_2}^{s_1} \\
\mathbf{Z}_{hj_1}^{s_1} & \mathbf{Z}_{hk_1}^{s_1} & \mathbf{Z}_{hj_2}^{s_1} & \mathbf{Z}_{hk_2}^{s_1} \\
\mathbf{Z}_{ej_1}^{s_2} & \mathbf{Z}_{ek_1}^{s_2} & \mathbf{Z}_{ej_2}^{s_2} & \mathbf{Z}_{ek_2}^{s_2} \\
\mathbf{Z}_{hj_1}^{s_2} & \mathbf{Z}_{hk_1}^{s_2} & \mathbf{Z}_{hj_2}^{s_2} & \mathbf{Z}_{hk_2}^{s_2}
\end{bmatrix}
\begin{bmatrix}
\mathbf{J}_{1z} \\
\mathbf{K}_{1t} \\
\mathbf{J}_{2z} \\
\mathbf{K}_{2t}
\end{bmatrix}
=
\begin{bmatrix}
\mathbf{E}_{inc}^z \\
\mathbf{H}_{inc}^t \\
\mathbf{0} \\
\mathbf{0}
\end{bmatrix}
\tag{3.106}
$$

This presentation shows the boundary, the boundary condition, and the current to which each element of the impedance matrix corresponds. For example, the submatrix $\mathbf{Z}_{ek_1}^{s_2}$ represents the contribution of the magnetic current on the first boundary to the electric field on the

second boundary. Each of the submatrices in (3.106) can be partitioned to multilevel blocks as shown in Fig. 3.9.

$\mathbf{Z}_{ej_1}^{s_1}$
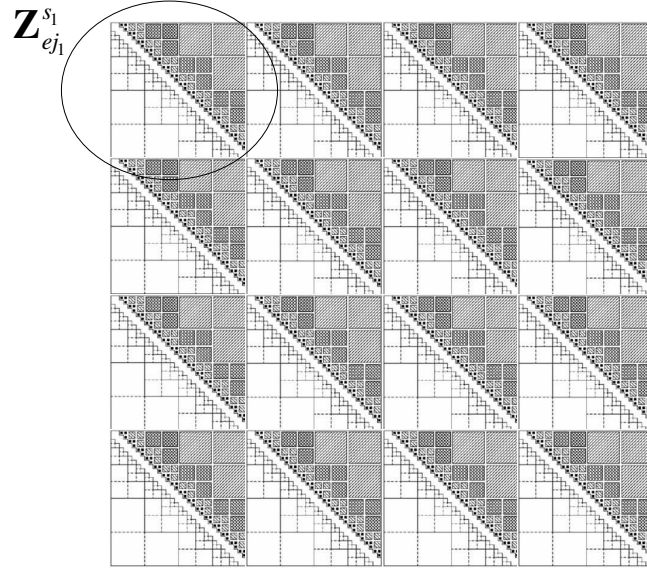
Figure 3.9: Multilevel partitioning of the submatrices of the impedance matrix in (3.67).

The distribution used in this chapter for sampling of the rows and columns of a block in a submatrix is uniform, because this distribution was found to lead to more accurate results for the problem considered here. See Appendix B.4 for another possible distribution.

3.7 Fast Solver Numerical Results

To check the performance of the fast solver, let's first consider a one-layer problem where the impedance matrix can be decomposed as in Fig. 3.10. The equations for the one-layer case can easily be derived from (3.106) and are shown below.

$$\begin{bmatrix} \mathbf{Z}_{ej_1}^{s_1} & \mathbf{Z}_{ek_1}^{s_1} \\ \mathbf{Z}_{hj_1}^{s_1} & \mathbf{Z}_{hk_1}^{s_1} \end{bmatrix} \begin{bmatrix} \mathbf{J}_{1z} \\ \mathbf{K}_{1t} \end{bmatrix} = \begin{bmatrix} \mathbf{E}_{inc}^z \\ \mathbf{H}_{inc}^t \end{bmatrix} \tag{3.107}$$
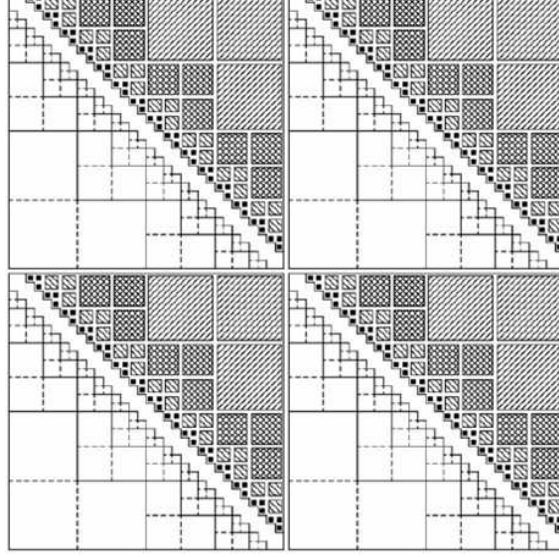
Figure 3.10: Multilevel partitioning of the submatrices of the impedance matrix in (3.107).

The matrix equation is solved using two different methods: LU decomposition to invert the full matrix and UV-MLP method along with an iterative solver called Transpose-Free Quasi-Minimal Residual (TFQMR) algorithm [65]. When solving the matrix equation $\mathbf{Ax} = \mathbf{b}$, the stopping criteria is

$$\frac{\|\mathbf{b} - \mathbf{Ax}\|}{\|\mathbf{b}\|} < \varepsilon \tag{3.108}$$

It is assumed that $\varepsilon = 10^{-3}$ throughout this chapter. For comparison purposes, only one realization of the random rough surface is considered. We should note that the iterative solver can be used for the full matrix inversion as well, but it has been observed that for the matrix sizes considered in this chapter, LU decomposition is faster.

The first simulated case is a one-layer structure where $\epsilon_{1r} = 8.0 + i0.05$, $\sigma_{f_1} = 1$ cm and $l_{f_1} = 20$ cm. The frequency is 300 MHz and the incidence angle is 45°. The number of cells used to discretize the rough surface is 1600 and the length of the rough surface is $L = 50\lambda_o$. The tapering factor is $g = L/10$. Fig. 3.11 shows the bistatic scattering coefficient calculated with both methods. Remember that the precision used for determining the rank of $\mathbf{W}$ is

assumed to be 10^{-10} throughout this chapter. It is also assumed that $N_{r_o} = 1$. Table 3.2 compares the computational cost of both methods assuming the size of the smallest block (represented by M) in the UV-MLP implementation is 50 by 50. According to Table 3.2, the computational cost of UV-MLP is obviously more than that of full-matrix handling. When UV-MLP is used, 'matrix filling' in this table refers to UV decomposition of the blocks, but refers to element by element calculation in the case of full-matrix handling. 'Linear system solver' refers to matrix inversion using LU decomposition in the case of full-matrix handling and refers to TFQMR algorithm when UV-MLP is used. Solving the linear system is faster using the iterative solver assuming the UV decompositions of the blocks are already available—the iterative solver takes about 40% less time. However, the total computational cost is larger when UV-MLP is used.
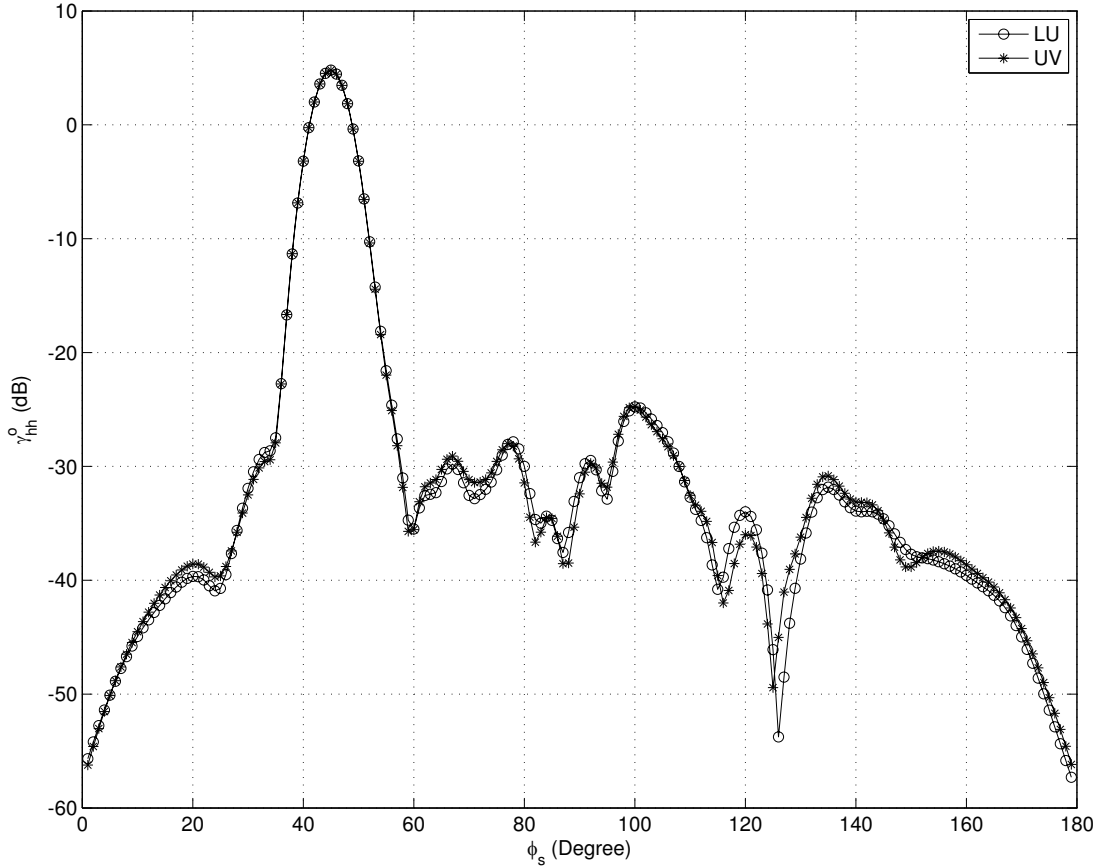
Figure 3.11: Bistatic scattering coefficient calculated with MoM using full-matrix solver and UV-MLP. Parameters: $\epsilon_{1r} = 8.0 + i0.05$, $N_1 = 1600$, $M = 50$.

Let's consider a larger problem where $\epsilon_{1r} = 16.0 + i0.05$ and where the number of cells

Table 3.2: Computation time for one realization of the MoM solver for full matrix and sampled matrix.

CPU: Pentium 4 (3.00 GHz), $N_1 = 1600$, $M = 50$, $N_{r_o} = 1$		
	Full Matrix	Sampled Matrix
Matrix Filling (Minutes)	14.7	44.1
Linear System Solver (Minutes)	1.5	0.9

used to discretize the rough surface is 2000. Other model and simulation parameters are the same except that $M = 125$. Fig. 3.12 shows the bistatic scattering coefficient for horizontal polarization. Table 3.3 compares the computational cost of both methods assuming the size of the smallest block in the UV-MLP implementation is 125 by 125. The computational cost of UV-MLP is still more than that of full matrix handling.
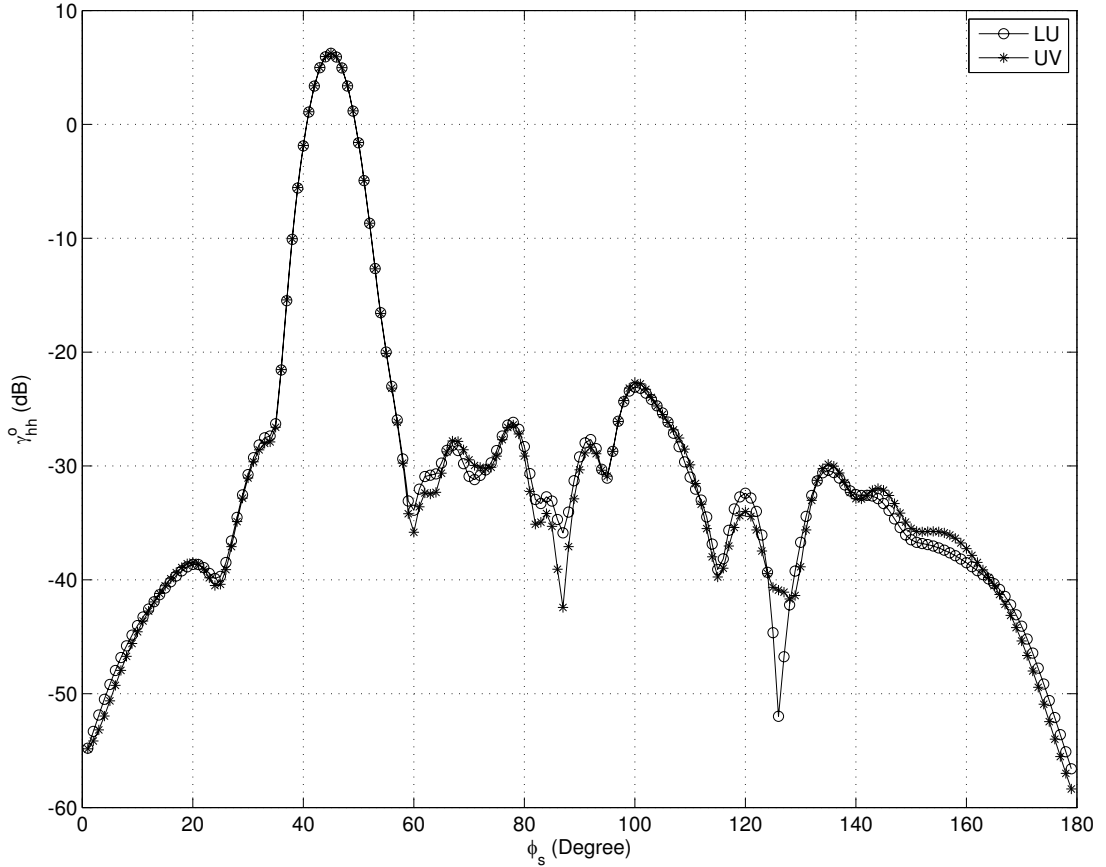
Figure 3.12: Bistatic scattering coefficient calculated with MoM using full-matrix solver and UV-MLP. Parameters: $\epsilon_{1r} = 16.0 + i0.05$, $N_1 = 2000$, $M = 125$.

Let's consider a larger matrix size where $\epsilon_{1r} = 16.0 + i0.05$ and where the number of cells

67

Table 3.3: Computation time for one realization of the MoM solver for full matrix and sampled matrix.

CPU: Pentium 4 (3.00 GHz), $N_1 = 2000$, $M = 125$, $N_{r_o} = 1$		
	Full Matrix	Sampled Matrix
Matrix Filling (Minutes)	22.4	41.2
Linear System Solver (Minutes)	2.8	1.3

used to discretize the rough surface is 2400. Other model and simulation parameters are the same except that $M = 75$. Fig. 3.13 shows the bistatic scattering coefficient for horizontal polarization. Table 3.4 compares the computation time for both methods assuming the size of the smallest block in the UV-MLP implementation is 75 by 75. Similar observation is made here. The computational cost of UV-MLP is still more than that of full matrix handling.
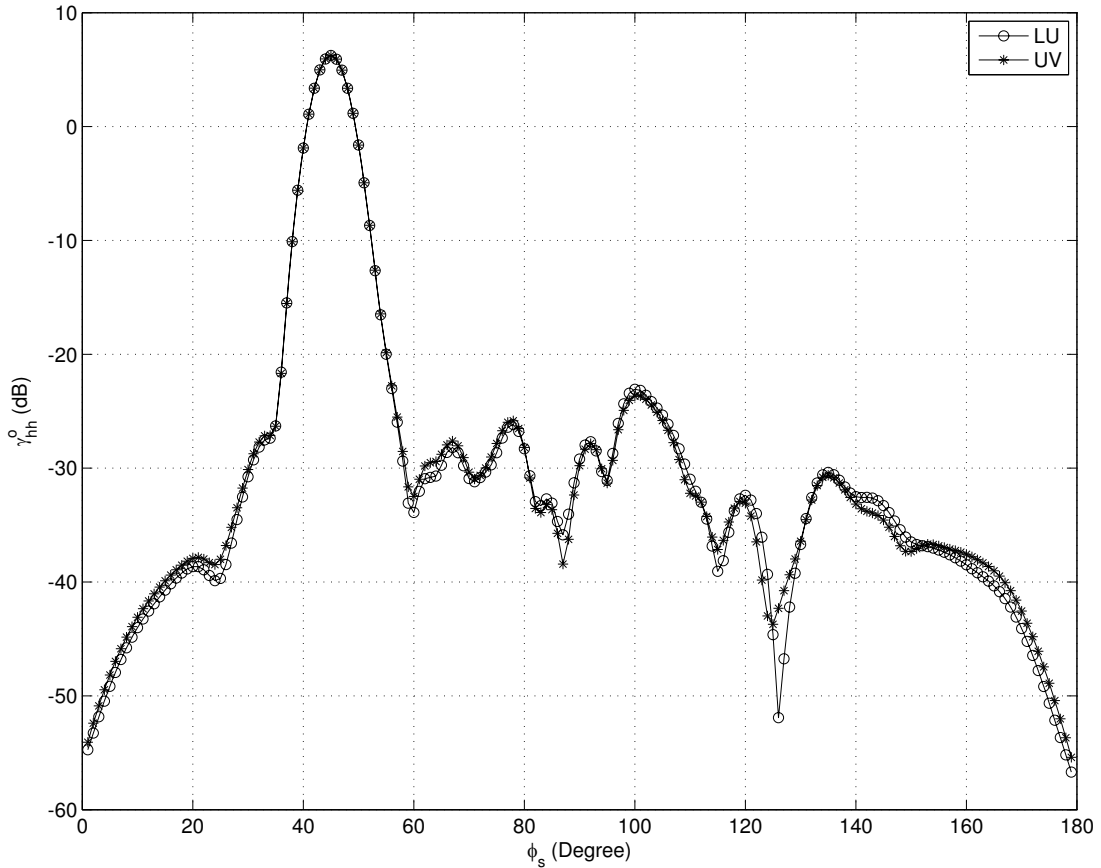
Figure 3.13: Bistatic scattering coefficient calculated with MoM using full-matrix solver and UV-MLP. Parameters: $\epsilon_{1r} = 16.0 + i0.05$, $N_1 = 2400$, $M = 75$, $N_{r_o} = 1$.

We should note that to increase the accuracy of the UV-MLP, we may increase N_{r_o},

Table 3.4: Computation time for one realization of the MoM solver for full matrix and sampled matrix.

CPU: Pentium 4 (3.00 GHz) , $N_1 = 2400$, $M = 75$, $N_{r_o} = 1$		
	Full Matrix	Sampled Matrix
Matrix Filling (Minutes)	32.0	63.7
Linear System Solver (Minutes)	4.9	2.0

which increases the computational cost of the method. To verify this fact, let's consider the same problem where $\epsilon_{1r} = 16.0 + i0.05$ and where the number of cells used to discretize the rough surface is 2400. Other model and simulation parameters are the same except that $N_{r_o} = 3$. Fig. 3.14 shows the result. Table 3.5 compares the computational cost of both methods assuming the size of the smallest block in the UV-MLP implementation is 75 by 75. It is observed that the accuracy has increased but the computational cost of UV-MLP has increased as well.

Table 3.5: Computation time for one realization of the MoM solver for full matrix and sampled matrix.

CPU: Pentium 4 (3.00 GHz), $N_1 = 2400$, $M = 75$, $N_{r_o} = 3$		
	Full Matrix	Sampled Matrix
Matrix Filling (Minutes)	32.0	226.6
Linear System Solver (Minutes)	4.9	1.9

For the matrix sizes considered in this chapter, the computational cost of the UV-MLP is more than that of a full-matrix solver. Therefore, to systematically compare the solution of SPM and MoM, we may focus our attention on using a full-matrix solver such as the one used in this chapter.

3.8   Region of Validity

Let's consider 5 different cases.

- Case 1: $\epsilon_{1r} = 2.0 + i0.01$, $\epsilon_{2r} = 4.0 + i0.02$, $d = 30$ cm, $l_{f_1} = 20$ cm, $\sigma_{f_1} = 1$ cm. The quantity l_{f_2} is varied between 1 cm and 20 cm. The quantity σ_{f_2} is varied between 1 cm and 5 cm. (100 cases)
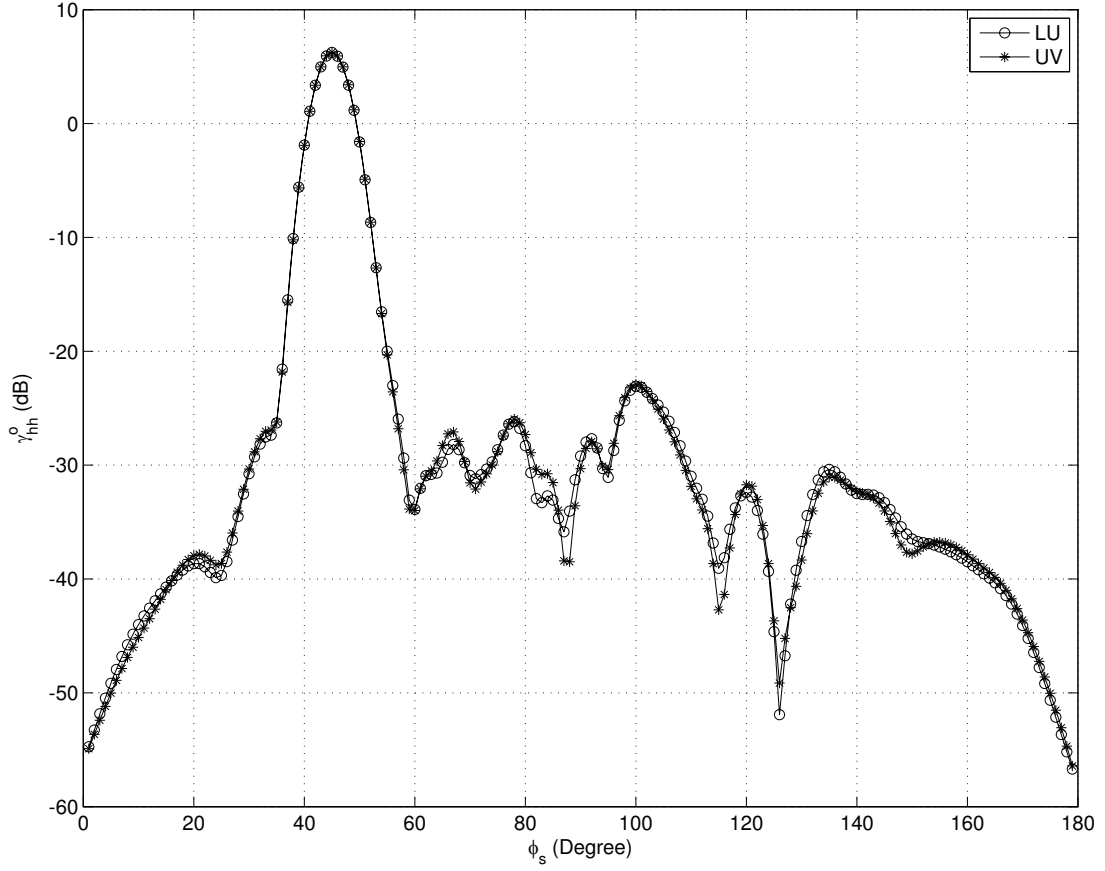
Figure 3.14: Bistatic scattering coefficient calculated with MoM using full-matrix solver and UV-MLP. Parameters: $\epsilon_{1r} = 16.0 + i0.05$, $N_1 = 2400$, $M = 75$, $N_{r_o} = 3$.

- Case 2: $\epsilon_{1r} = 2.0 + i0.01$, $\epsilon_{2r} = 4.0 + i0.02$, $d = 30$ cm, $l_{f_2} = 20$ cm, $\sigma_{f_2} = 1$ cm. The quantity l_{f_1} is varied between 1 cm and 20 cm. The quantity σ_{f_1} is varied between 1 cm and 5 cm. (100 cases)

- Case 3: $\epsilon_{1r} = 4.0 + i0.01$, $\epsilon_{2r} = 8.0 + i0.02$, $d = 30$ cm, $l_{f_1} = 20$ cm, $\sigma_{f_1} = 1$ cm. The quantity l_{f_2} is varied between 1 cm and 20 cm. The quantity σ_{f_2} is varied between 1 cm and 5 cm. (100 cases)

- Case 4: $\epsilon_{1r} = 4.0 + i0.01$, $\epsilon_{2r} = 8.0 + i0.02$, $d = 30$ cm, $l_{f_2} = 20$ cm, $\sigma_{f_2} = 1$ cm. The quantity l_{f_1} is varied between 1 cm and 20 cm. The quantity σ_{f_1} is varied between 1 cm and 5 cm. (100 cases)

- Case 5: $\epsilon_{1r} = 4.0 + i0.01$, $\epsilon_{2r} = 8.0 + i0.02$, $d = 15$ cm, $l_{f_1} = 20$ cm, $\sigma_{f_1} = 1$ cm. The quantity l_{f_2} is varied between 1 cm and 20 cm. The quantity σ_{f_2} is varied between 1 cm and 5 cm. (100 cases)

These cases help understand the effects of dielectric constants of the layers and the statistical properties of the interfaces on accuracy of SPM solution. Case 5 is considered in order to observe how the thickness would change the accuracy of the SPM solution.

Fig. 3.15 through Fig. 3.19 show $|\gamma_{\mathrm{MoM}} - \gamma_{\mathrm{SPM}}|$ versus $k\sigma$ and kl, where k is the wavenumber of the medium with the varying statistical properties. For example, in Fig. 3.15, which corresponds to Case 1, the contours are plotted versus $k_2\sigma_2$ and k_2l_2. Both of the parameters γ_{MoM} and γ_{SPM} are expressed in dB.

The immediate conclusion is that σ_f/λ and l_f/λ are not the only parameters that would determine the region of validity, because despite the fact that the contours are plotted versus $k\sigma_f$ and kl_f, we observe different regions of validity in each case. This fact is confirmed when we compare Fig. 3.15 and Fig. 3.17 or Fig. 3.16 and Fig. 3.18. These figures suggest that the region of validity is also a function of dielectric constants of both layers. Therefore, even if we are able to accurately determine the region of validity for a set of dielectric constants, care is needed when using SPM in an inversion algorithm, because as we will see in Chapter 4, the forward model is assumed to be accurate in a range of values of the dielectric constants and other model parameters. So the recommendations we make must take into account the need for a region of validity that is accurate for a range of values of the dielectric constants. This task is not easy as apparent from the plots. We should add that the region of validity is also a function of polarization and incidence/scattering angles, but these parameters are fixed in this analysis.

We can make some qualitative observations based on the contour plots shown below. Based on the rate of change in the colors, we can conclude that sensitivity of the region of validity to σ_f is more for larger dielectric constants. This sensitivity also increases as σ_f increases. Another qualitative, and expected, observation is that for Case 1 through Case 4, a combination of large σ_f and small l_f decreases the accuracy of SPM. This observation is not valid in Case 5, where the thickness is smaller, causing the effect of multiple scattering processes between the layers more pronounced. An interesting observation is that when the

correlation length becomes large enough, meaning the surfaces become very slowly vary-ing, large σ_f is tolerable and does not decrease the accuracy of SPM regardless of surface roughness height.

If we consider 1.5 dB a tolerable difference between the SPM and MoM solutions, based on Fig. 3.15 and Fig. 3.17, a conservative condition would be $k_2\sigma_2 < 0.6$ although for slowly varying surfaces, we can go beyond this limit. A similar limit can be expressed based on Fig. 3.16 and Fig. 3.18, which suggest $k_1\sigma_1 < 0.3$. This condition is similar to the one reported in [66] for one-layer structures. It is also observed that for small enough σ_f, no obvious lower limit of l_f exists. Although this statement is true for the cases simulated here, for a more accurate statement on l_f, as well as other model parameters, we need more extensive numerical simulations and more systematic comparisons between the SPM and MoM solutions. One possible method is locally minimizing a cost function defined as the difference between the bistatic scattering coefficients calculated using both methods.

3.9 Summary and Conclusion

A PMCHWT-based integral equation was used to calculate the scattering coefficients of a two-layer rough surface structure and the numerical results were compared with those found from SPM formulation. The difference between the SPM and MoM solutions implied the need for deriving the region of validity of SPM. To systematically compare the solutions of SPM and MoM, a fast solver known as the UV Multilevel Partitioning Method (UV-MLP) was implemented. To test the performance of the fast solver, it was used for a one-layer structure. It was observed that the computational cost of the method is more than that of a solver such as LU factorization, which uses the full impedance matrix. Consequently, LU factorization was used as the MoM solver and 500 different combinations of the statistical properties of the interfaces and dielectric constants of the layers were simulated. The contour plots suggested that σ_f/λ and l_f/λ are not the only parameters that would determine the region of validity, which is believed to be a function of the dielectric constants as well. Another conclusion was that the sensitivity of the region of validity to σ_f is more for larger dielectric constants and also increases as σ_f increases. An interesting observation was that
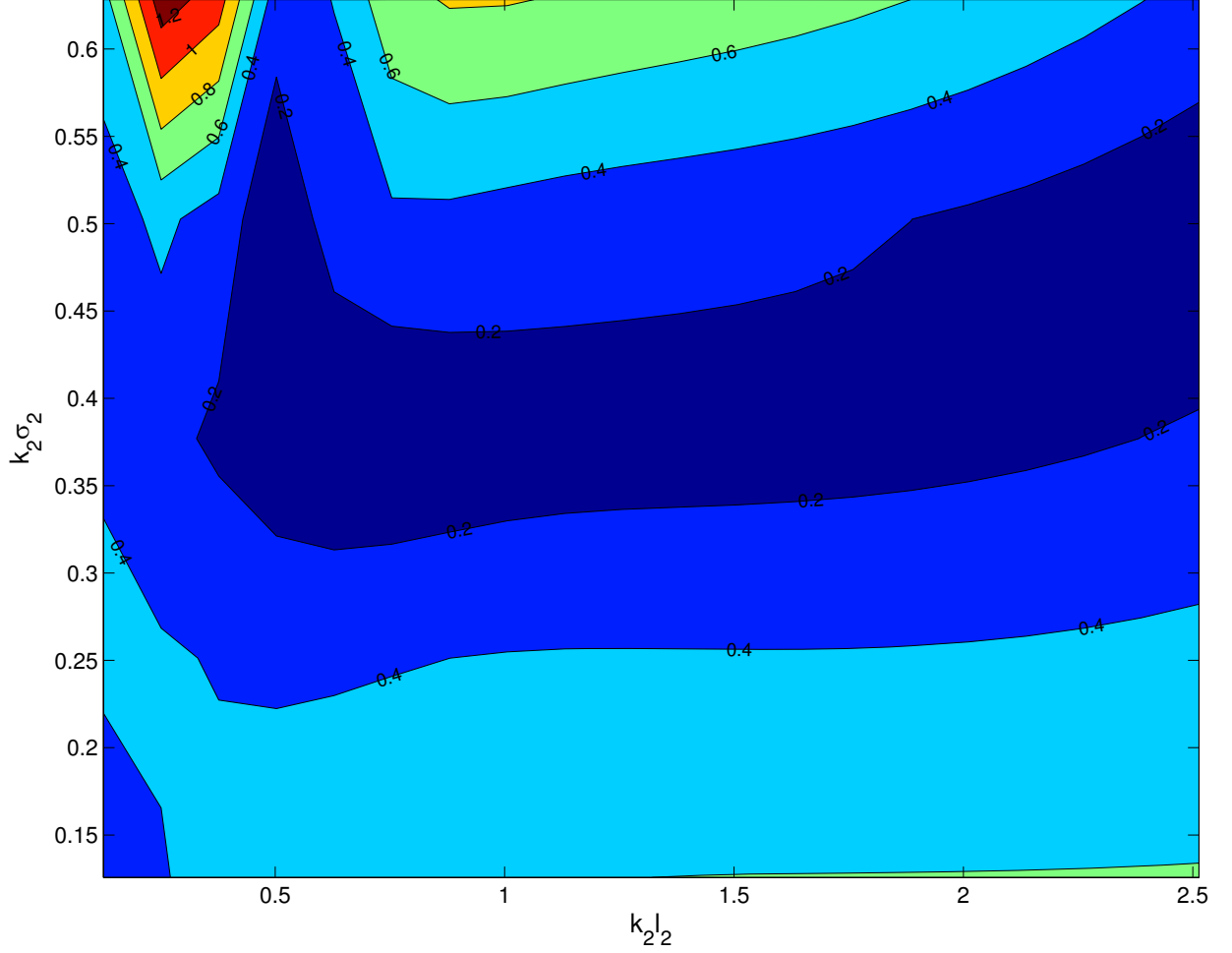
Figure 3.15: Contour plot of $|\gamma_{\mathrm{MoM}} - \gamma_{\mathrm{SPM}}|$ for Case 1. Both of the parameters γ_{MoM} and γ_{SPM} are expressed in dB.

when surfaces become very slowly varying, large σ_f becomes tolerable and does not decrease the accuracy of SPM. Quantitative observations made were that if we consider 1.5 dB a tolerable difference between the SPM and MoM solutions, $k_2\sigma_2 < 0.6$ and $k_1\sigma_1 < 0.3$ would be conservative conditions on the surface roughnesses although for slowly varying surfaces, we can go beyond these limits. It was also observed that for small enough σ_f, no obvious lower limit of l_f exists. For a more systematic comparison and more definitive statements on the limits on the model parameters, especially those limits that are affected by multiple scattering processes between the boundaries, it was suggested that an optimization problem be solved to locally minimize the error between the SPM and MoM solutions with respect to surface and media parameters.
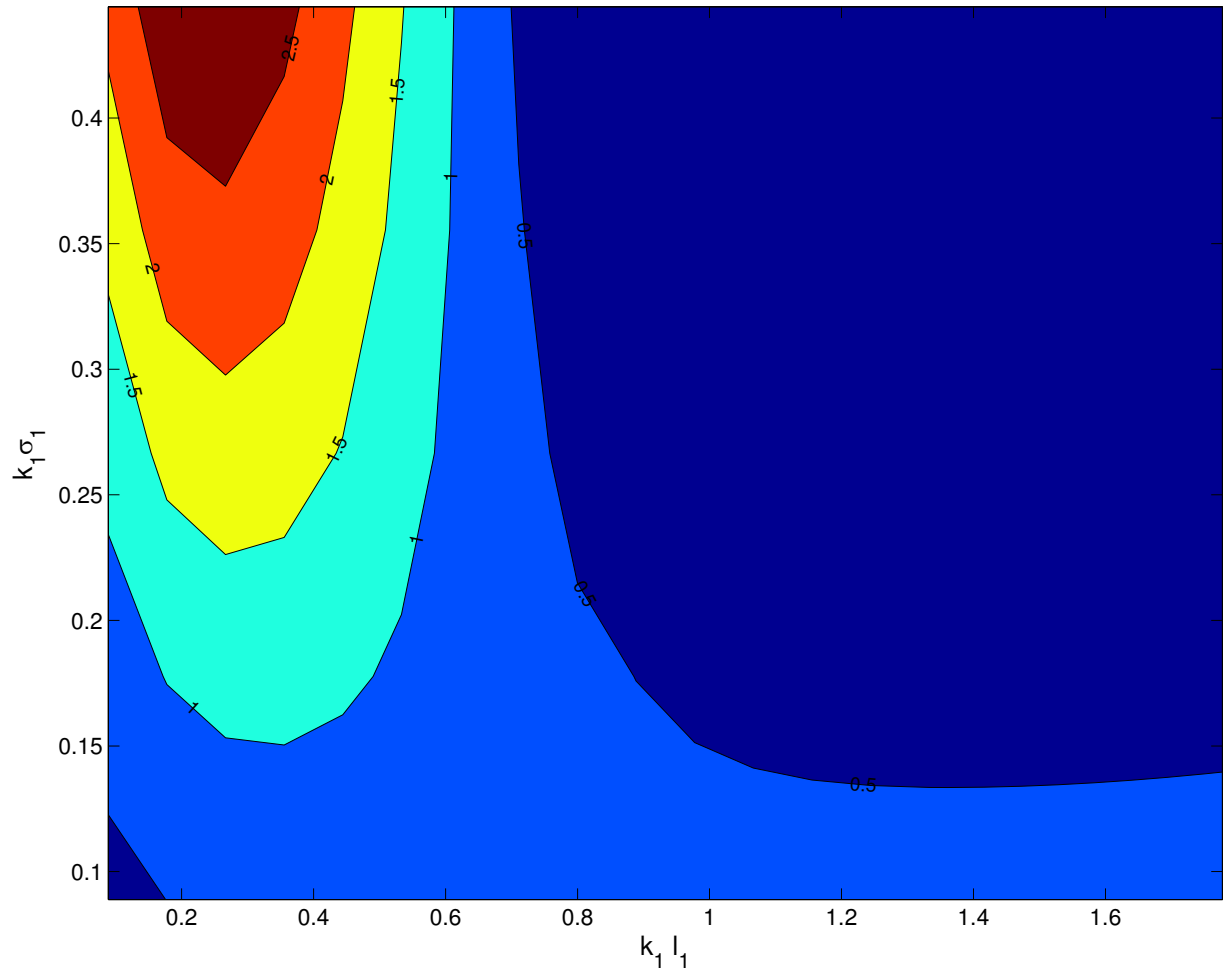
Figure 3.16: Contour plot of $|\gamma_{\mathrm{MoM}} - \gamma_{\mathrm{SPM}}|$ for Case 2. Both of the parameters γ_{MoM} and γ_{SPM} are expressed in dB.
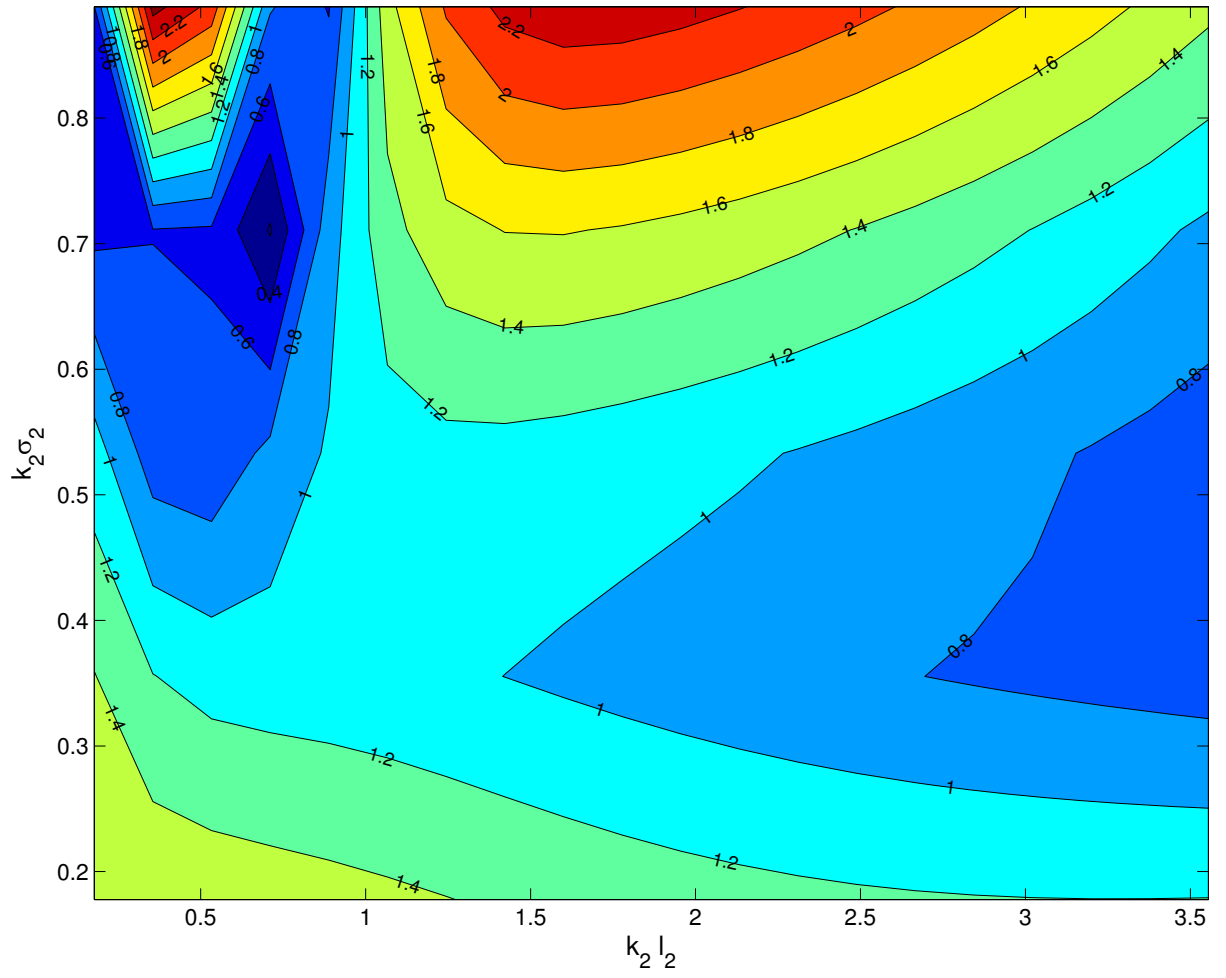
Figure 3.17: Contour plot of $|\gamma_{\text{MoM}} - \gamma_{\text{SPM}}|$ for Case 3. Both of the parameters γ_{MoM} and γ_{SPM} are expressed in dB.
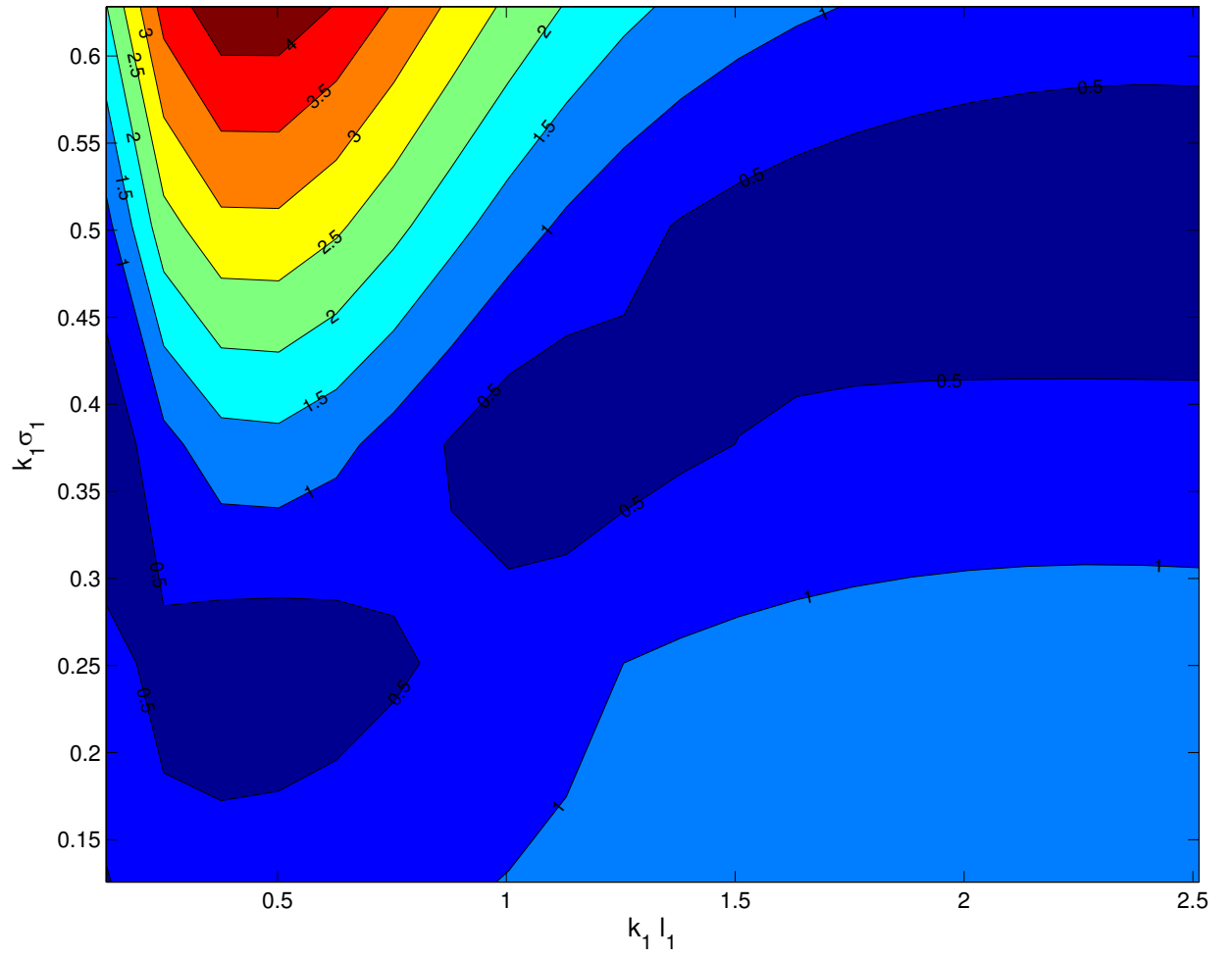
Figure 3.18: Contour plot of $|\gamma_{\mathrm{MoM}} - \gamma_{\mathrm{SPM}}|$ for Case 4. Both of the parameters γ_{MoM} and γ_{SPM} are expressed in dB.
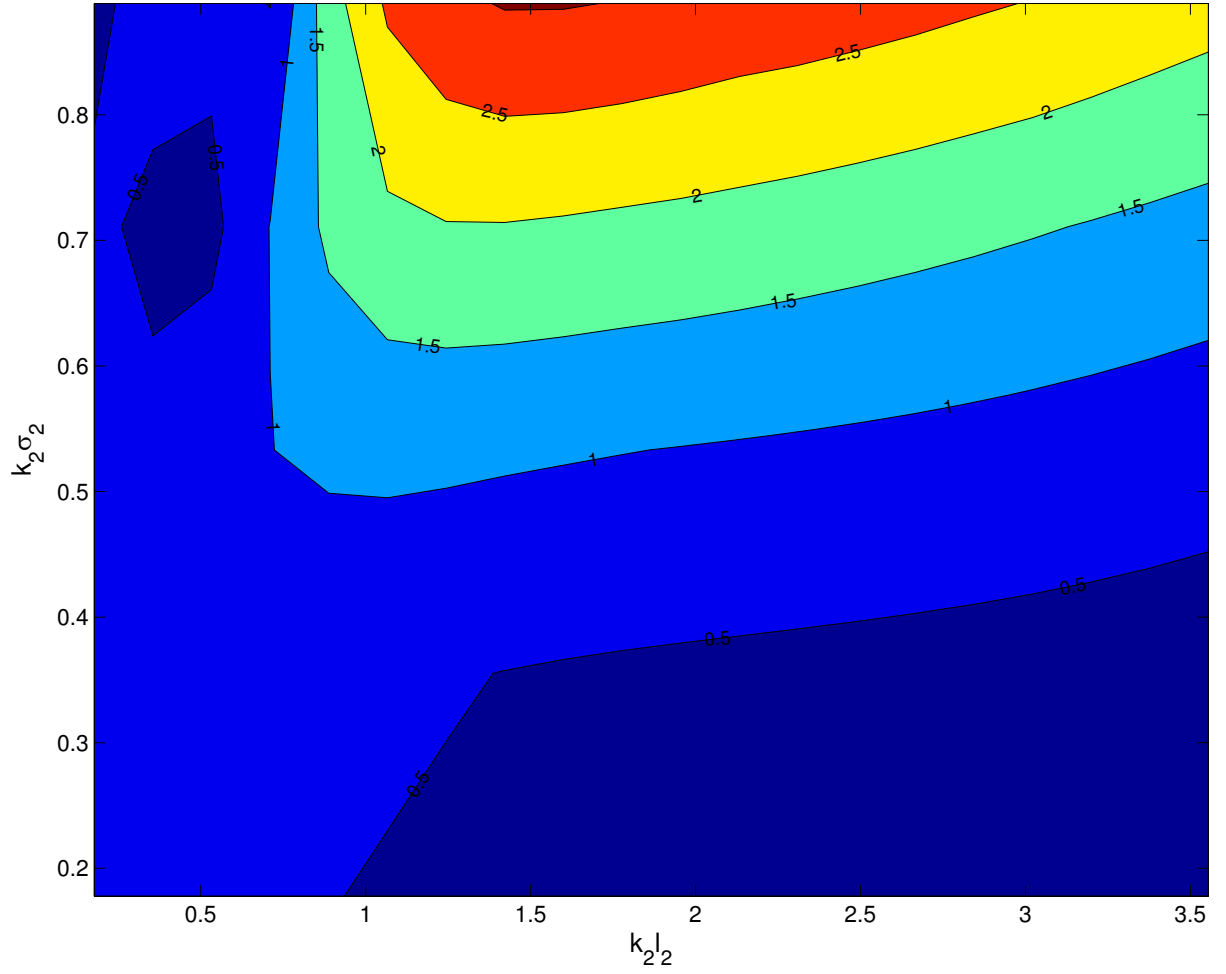
Figure 3.19: Contour plot of $|\gamma_{\mathrm{MoM}} - \gamma_{\mathrm{SPM}}|$ for Case 5. Both of the parameters γ_{MoM} and γ_{SPM} are expressed in dB. This case shows how the multiple scattering processes between the layers could lead to counter intuitive results for the region of validity.

CHAPTER 4

Inversion of Subsurface Properties of Layered Dielectric Structures with Random Slightly-Rough Interfaces Using the Method of Simulated Annealing

In this chapter, the parameters of a two-layer dielectric structure with random slightly-rough boundaries are retrieved from data that consist of the backscattering coefficients for multiple polarizations, angles, and frequencies. The Small Perturbation Method (SPM) is used to solve the forward problem and assume the roughnesses are small compared to the wavelength. The inversion problem is then formulated as a least square problem and is solved using a global optimization method known as the Simulated Annealing (SA). This method is capable of minimizing cost functions with global minima hidden among many local minima and is shown to be a robust retrieval algorithm. The algorithm performance depends on several parameters. Recommendations are made on these parameters and a technique is proposed for exiting local minima when encountered. The sensitivity of the inversion scheme to measurement noise is tested and it is shown that by averaging over several measurements, the Gaussian noise is suppressed in such a way that the algorithm retrieves the parameters successfully.

4.1 Introduction

The problem of determining the properties of layered rough surface structures from scattering data arises in many areas of science and engineering such as geosciences, biomedicine, and optics. These structures are of special interest, because they are representative models for many naturally occurring structures ranging from layered soil, rivers, and lakes to smaller scale objects such as the human body and optical thin films. This class of problems falls within the broad category of inverse scattering problems, in which the goal is to characterize the electrical and geometric scattering properties of a target from the scattered field. Complex dielectric constants, layer thicknesses, and statistical properties of the boundaries are the unknowns in an inverse scattering problem associated with a layered dielectric structure with rough boundaries. Of particular interest is estimation of soil moisture, which can be translated as estimation of the soil permittivity for a general soil type. This problem is of special interest in environmental engineering, hydrology, geology, soil physics, civil engineering, and planetary exploration.

Effects of soil moisture and surface roughness on the backscattered field have been studied dating back to the the 1960's and 70's [5–7]. Passive microwave radiometers have been widely used for soil moisture retrieval [8,9,67], but use of radiometers in soil moisture detection is limited because of their low resolution at lower frequencies, which are required for subsurface observations. Active sensors have the potential to make the inversion of soil properties more rigorous. Experiments conducted with active sensors at the ground level [7,68], and via aircraft and satellite [69] have shown strong radar backscatter dependence on soil moisture. These experiments have also demonstrated the significant effect of surface parameters such as surface roughness on radar backscatter.

The inversion models for estimation of the surface parameters, i.e., permittivity, surface roughness, and surface correlation length, can generally be categorized into empirical and theoretical models. Empirical models are based on experimental data and the scattering behavior of the rough surface in limiting cases. These models use inversion methods as simple as solving a system of algebraic equations, to estimate the surface parameters. The corresponding forward models are empirical and are developed from measurement of the

scattering coefficients σ_{hh}^o, σ_{vv}^o, and σ_{hv}^o [10, 11, 70]. The empirical inversion models are fast, hence suitable for real time inversion. However, they are not only site-specific but also difficult to develop for layered media, in which case many measurements are required to account for different combinations of the model parameters. On the other hand, inversion algorithms that utilize theoretical forward models, which sometimes use involved numerical techniques [71], are not site-specific and are more accurate, but more challenging, too [72]. Statistical inversion [73], neural network [74, 75], the simplex method [76], and the genetic algorithm [77] are among these techniques. Progress in theoretical forward models such as the Integral Equation Method (IEM) has offered alternative approaches to inversion [78].

As the number of layers increases, the number of measurements needed to invert for the unknowns also increases and the inversion process would become more challenging, due to the severe nonlinearity of the forward model. The focus of this chapter is on retrieving the parameters of a two-layer dielectric structure with rough boundaries shown in Fig. 4.1. Despite the practical importance of this problem, its solution has not yet been addressed appropriately due to a number of reasons including the complexity and lack of forward scattering solutions, lack of experimental data, and the large number of distinct physical parameters needed to characterize the scatterer. To nondestructively calculate the characteristics of layered structures, a multifrequency polarimetric radar backscattering approach can be used, where subsurface probing capability is achieved through the use of low frequency radar measurements. Such systems are at preliminary research stages, and therefore to refine their operating parameters and measurement scenarios, it is essential to use theoretical scattering models that are general enough to be able to simulate the backscattering responses of a wide range of subsurface structures. These forward models should be fast and accurate in order that they enable reliable inversion algorithms for the subsurface sensing. A number of analytical and numerical models for radar scattering from general N-layer rough surfaces, including an incoherent small perturbation model, developed in Chapter 2, and a full-wave coherent model for the general roughness case [49] have been introduced recently. The latter has provisions for including dielectric profiles and both classes of models can incorporate discrete random scatterers. These models have the required parametric flexibility suitable for inversion of layered media properties.

The inverse scattering problem considered here can be regarded as a nonlinear parameter-estimation problem. An optimization scheme, known as Simulated Annealing, is applied to solve the estimation problem. While the capability of other global optimization methods such as genetic algorithm [79] and particle swarm [80] can be studied and explored for the purpose of subsurface sensing, the purpose of this work is to investigate the performance of the Simulated Annealing method in inversion associated with layered structures.

Since the forward problem based on which the estimation is carried out is a complicated nonlinear function of the parameters, care must be taken to understand and best use the regions of sensitivity of the forward model to the parameters to ensure convergence to correct results. The scattering data used with this inversion algorithm consist of measurements of the backscattered wave for different incidence angles at center frequencies of 137 and 435 MHz. (The use of the SPM model at 137 and 435 MHz is justified because at these frequencies, most surfaces of interest appear only slightly rough.) Synthetic data are used to develop and validate the inversion algorithm. The choice of frequencies is made based on currently available radar systems and these are envisioned to be available from airborne and spaceborne platforms in the foreseeable future [19].

A brief introduction to the forward model is presented in Section 4.2. Section 4.3 introduces the inverse problem, the model parameters, the inversion algorithm, the cost function, and the measurement and inversion parameters. Simulation results including the results of a sensitivity analysis in Section 4.4 will be presented afterward. The results of noise analysis follow in Section 4.5.

4.2   The Forward Model

The success of any approach to an inverse problem depends critically on the validity of the forward model employed. The forward model, reported in Chapter 2, uses SPM to calculate the electromagnetic wave scattered from the rough surface structure shown in Fig. 4.1. The solution is analytic in the sense that it does not rely on numerical techniques or discretizing approximations to the unknowns. Therefore, its dependence on the unknowns has an explicit form, which can be evaluated fast. This is a great advantage, because in an inversion process,
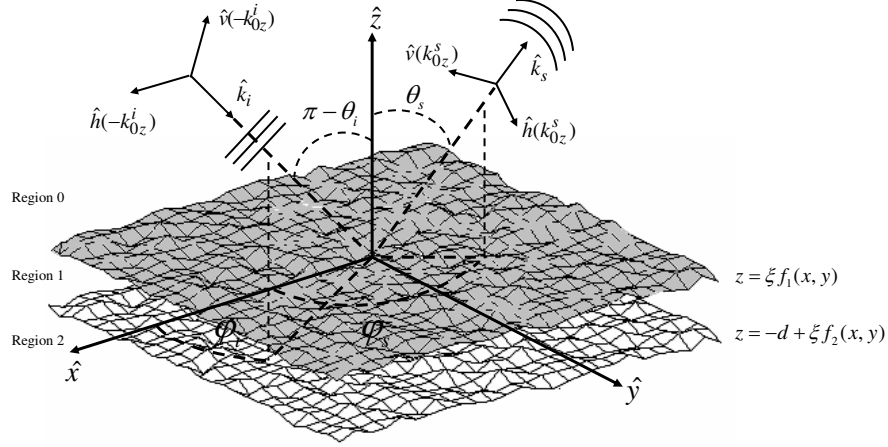
Figure 4.1: Geometry of the problem: a 3-dimensional 2-layer isotropic dielectric structure with complex permittivities. The boundaries are zero-mean stationary random processes. The layers mean separation is denoted as d.

the forward model could be evaluated a large number of times.

The forward model is presented briefly and the reader is referred to Chapter 2 for details. Consider the three-dimensional, two-layer homogeneous isotropic dielectric structure with infinite surfaces shown in Fig. 4.1, where the top and bottom regions are half-spaces. The dielectric constants are ϵ_0, ϵ_1, and ϵ_2, which in general could have complex values. The permeability of all of the layers is assumed to be μ_0, although this assumption does not impact the analysis method. The boundaries, which are assumed to be zero-mean stationary random processes with known statistical properties, are denoted by $\xi f_1(x, y)$ and $-d + \xi f_2(x, y)$. The conditions on the surface statistical properties for which the first-order SPM is accurate within a specified error bound is determined by the region of validity. This region is a function of the layers complex dielectric constants, polarization of the incidence wave, and the incidence angle. The region of validity of SPM for a single dielectric rough surface is known to be $k_1 \sigma_{f_1} < 0.3$ and $\sqrt{2} \sigma_{f_1}/l_1 < 0.3$ [66]. It has been mentioned in the same reference that no precise validity conditions have been obtained for SPM and the given conditions should be viewed only as a guideline. The focus of this chapter is on the effectiveness of the inversion algorithm independent of the physical accuracy of the forward model. The region of validity of SPM for a two-layer dielectric structure with rough boundaries was addressed

in Chapter 3.

The first-order scattered field can be represented as

$$\mathbf{E_s^{(1)}(r)} = \xi \int\limits_{-\infty}^{\infty} \int\limits_{-\infty}^{\infty} \mathrm{d}\mathbf{k}_\perp \left[a_h^{+(1)}(\mathbf{k}_\perp)\hat{h}(k_{0z}) + a_v^{+(1)}(\mathbf{k}_\perp)\hat{v}(k_{0z}) \right] e^{ik_{0z}z} e^{i\mathbf{k}_\perp \cdot \mathbf{r}_\perp} \qquad (4.1)$$

where $\mathbf{k}_\perp = k_x\hat{x} + k_y\hat{y}$, $\mathrm{d}\mathbf{k}_\perp = \mathrm{d}k_x\mathrm{d}k_y$, and $k_{0z} = \sqrt{k_0^2 - k_x^2 - k_y^2}$. The quantities k_x and k_y are the Fourier transform variables and k_0 is the incidence region wavenumber. The quantities $a_{h,v}^{+(1)}(\mathbf{k}_\perp)$ are the first order amplitudes of the scattered field and are given by

$$a_h^{+(1)}(\mathbf{k}_\perp) = \alpha_h^{f_1}(\mathbf{k}_\perp)F_1(\mathbf{k}_\perp - \mathbf{k}_\perp^i) + \alpha_h^{f_2}(\mathbf{k}_\perp)F_2(\mathbf{k}_\perp - \mathbf{k}_\perp^i) \qquad (4.2)$$

$$a_v^{+(1)}(\mathbf{k}_\perp) = \alpha_v^{f_1}(\mathbf{k}_\perp)F_1(\mathbf{k}_\perp - \mathbf{k}_\perp^i) + \alpha_v^{f_2}(\mathbf{k}_\perp)F_2(\mathbf{k}_\perp - \mathbf{k}_\perp^i) \qquad (4.3)$$

where $F_1(\mathbf{k}_\perp)$ and $F_2(\mathbf{k}_\perp)$ are the Fourier transforms of $f_1(x,y)$ and $f_2(x,y)$, respectively. The subscripts h and v represent the horizontal (h) and vertical (v) polarizations, respectively. The reader is referred to Chapter 2 for the details of calculation of the coefficients $\alpha_h^{f_1}(\mathbf{k}_\perp)$, $\alpha_h^{f_2}(\mathbf{k}_\perp)$, $\alpha_v^{f_1}(\mathbf{k}_\perp)$, and $\alpha_v^{f_2}(\mathbf{k}_\perp)$. Finally, it can be shown that the bistatic scattering coefficients of the layered structure are given by

$$\sigma_{pq}^o = 4\pi k_0^2 \cos^2\theta_s \xi^2 \left(|\alpha_{pq}^{f_1}(\mathbf{k}_\perp^s)|^2 W_{f_1}(\mathbf{k}_\perp^s - \mathbf{k}_\perp^i) + |\alpha_{pq}^{f_2}(\mathbf{k}_\perp^s)|^2 W_{f_2}(\mathbf{k}_\perp^s - \mathbf{k}_\perp^i) \right), \qquad (4.4)$$

where $\alpha_{pq}^{f_i}(\mathbf{k}_\perp^s) = \alpha_p^{f_i}(\mathbf{k}_\perp^s)$ with the incident field having q-polarization component only, where $p, q \in \{h, v\}$. The vectors $\mathbf{k}_\perp^i$ and $\mathbf{k}_\perp^s$ refer to the incidence and scattering directions, respectively, and θ_s denotes the scattering angle. The quantities $W_{f_1}(\mathbf{k}_\perp)$ and $W_{f_2}(\mathbf{k}_\perp)$ are the spectral densities of the rough surfaces, which are assumed to be independent. (If the surfaces are correlated, the joint spectral density of the two surfaces, defined as the Fourier transform of the correlation function of the two profiles, will be present in (4.4). See Chapter 2 for more details. Therefore, the number of model parameters will increase if the surfaces are correlated, but the approach to the inversion would be similar.)

4.3 The Inverse Problem

The goal in an inverse problem is to determine a vector of unknown parameters $\mathbf{X}$, given a set of data $\mathbf{d} = \mathbf{f}(\mathbf{X}, \mathbf{p}) + \mathbf{n}$, where the vector $\mathbf{f}$ represents the forward function and the vector $\mathbf{p}$ represents known measurement parameters such as the frequency of operation and incidence angle. The vector $\mathbf{n}$ represents any additive error that may contaminate the measured data. In a probabilistic approach to inverse problems, knowledge of the probability distributions of $\mathbf{d}$ and $\mathbf{n}$ is also necessary, but in this work, the approach is deterministic in that such distributions are not considered.

4.3.1 Model Parameters

There are two types of model parameters involved in the forward model: dielectric parameters, namely real and imaginary parts of a layer dielectric constant ($\epsilon_i^{'}$ and $\epsilon_i^{''}$), and geometry parameters, namely the mean separation between the two rough interfaces referred to as layer thickness (d) and statistical properties of the boundaries (σ_{f_i} and l_{f_i}). The dielectric parameters depend on the mixture model used for the scattering media. Several mixture models exist for soil and ice dielectric properties at different frequency ranges [33, 81, 82].

Nine model parameters are used to characterize the two-layer structure. These parameters are real parts of the layer permittivities ($\epsilon_1^{'}$ and $\epsilon_2^{'}$), conductivities of the layers (σ_1 and σ_2), the standard deviation and correlation length of each interface (σ_{f_i} and l_{f_i}), and the layer thickness (d). The vector of unknowns, $\mathbf{X}$, is defined in such a way that $\mathbf{X}(1) = \epsilon_{1r}^{'}$, $\mathbf{X}(2) = \sigma_1$, $\mathbf{X}(3) = \epsilon_{2r}^{'}$, $\mathbf{X}(4) = \sigma_2$, $\mathbf{X}(5) = d$, $\mathbf{X}(6) = l_{f_1}$, $\mathbf{X}(7) = \sigma_{f_1}$, $\mathbf{X}(8) = l_{f_2}$, and $\mathbf{X}(9) = \sigma_{f_2}$. SI units are used for all of the model parameters, that is to say siemens per meter (S/m) for conductivity (σ_1 and σ_2) and meter (m) for length (d, l_{f_1}, l_{f_2}, σ_{f_1}, and σ_{f_2}). Table 4.1 summarizes the physical model parameters and their analogous elements of the unknown vector $\mathbf{X}$.

Table 4.1: The physical model parameters and their analogous elements of $\mathbf{X}$.

$\mathbf{X}(1)$	$\mathbf{X}(2)$	$\mathbf{X}(3)$	$\mathbf{X}(4)$	$\mathbf{X}(5)$	$\mathbf{X}(6)$	$\mathbf{X}(7)$	$\mathbf{X}(8)$	$\mathbf{X}(9)$
$\epsilon_{1r}^{'}$	σ_1	$\epsilon_{2r}^{'}$	σ_2	d	l_{f_1}	σ_{f_1}	l_{f_2}	σ_{f_2}

Based on the dielectric model for soils given in [33], $\epsilon^{'}$ and $\epsilon^{''}$ are functions of four other parameters, i.e., volumetric moisture content (m_v), bulk density (ρ_b), and mass fractions of sand and clay (S and C). To present the general methodology of inversion by the method of Simulated Annealing and show its strength, The generic model for the complex dielectric constant is used, i.e., it is assumed that $\epsilon = \epsilon^{'} + i\sigma/\omega$ and that the real part of the dielectric constant does not vary with frequency in the frequency range considered—a good assumption according to [33]. After $\epsilon^{'}$ and σ have been retrieved, m_v can be found by making certain assumptions about type of the soil. The dielectric model used in the forward problem can always be modified to make it appropriate for the dielectric structure under study and the corresponding application based on ancillary data.

The inverse problem is posed as an optimization problem. Since multiple parameters determine the measured radar signal, multiple measurements viewed at different frequencies and observation angles are necessary to define the cost function. The cost function used in this chapter is

$$L(\mathbf{X}) = \sum_{i=1}^{N_f} \sum_{j=1}^{N_\theta} \left[\left(\frac{\sigma_{vv}^o \left(\mathbf{X}; f_i, \theta_j\right) - d_{vv}(f_i, \theta_j)}{d_{vv}(f_i, \theta_j)} \right)^2 + \left(\frac{\sigma_{hh}^o \left(\mathbf{X}; f_i, \theta_j\right) - d_{hh}(f_i, \theta_j)}{d_{hh}(f_i, \theta_j)} \right)^2 \right] \quad (4.5)$$

where N_f and N_θ are the number of frequency points and measurement angles used in measurement, respectively. As it is apparent from the definition above, all of the possible combinations of the N_f frequency points and N_θ measurement angles are used. The values of $\sigma_{pq}^o \left(\mathbf{X}; f_i, \theta_j\right)$ and $d_{pq} \left(f_i, \theta_j\right)$ are, respectively, the calculated and measured backscattering coefficient of the layered structure at a certain frequency and observation angle for pq polarization, where $p, q \in \{h, v\}$. Since the forward model is incoherent, the only backscattering coefficients available from the model are σ_{vv}^o and σ_{hh}^o. The normalizing terms in (4.5) are in fact regularizing factors. This definition of the cost function causes the measurements at different frequencies and angles to matter equally. If we do not use these normalizing terms, the elements of the measured data vector, which have different strengths at different frequencies and angles, would have unbalanced contributions to the value of the cost function.

4.3.2   Inversion Algorithm

Local optimization techniques are popular for solving optimization problems because of their speed, but due to the nonlinearity of the forward models and existence of many local minima, use of these techniques in geophysical inversion is limited. Such techniques require very good *a-priori* information, or initial guesses, to avoid converging to (or getting trapped in) local minima. Existence of many local minima in a cost function is the cause of the poor performance of local optimization methods in terms of convergence to correct results.

The inversion technique applied to the problem is an optimization scheme known as the Simulated Annealing (SA). Simulated Annealing is a global optimization technique capable of minimizing cost functions with global minima hidden among many local minima [83, 84]. This method uses an analogy between the unknown parameters in an optimization problem and particles in the annealing process of solids. These particles are distributed randomly in the liquid phase at a high temperature. If cooling happens slowly enough, at each temperature T, the solid reaches thermal equilibrium, which is characterized by the Boltzmann distribution [83]. As the temperature decreases, the distribution concentrates on lower energies, and finally, when the temperature approaches zero, the only state that has a non-zero probability is the minimum energy state. In an optimization problem, the cost function $L(\mathbf{X})$ and configurations of the model parameters are analogous to energy and different states of a solid, respectively.

In an SA-based algorithm, a small, randomly generated perturbation is applied to the current model parameters. If the cost function decreases, i.e., $\Delta L \leq 0$, the new state is accepted, otherwise it is accepted with probability $e^{-\Delta L/T}$. The quantity T represents the temperature. This rule is referred to as the Metropolis criterion [85] and the SA-based methods use this criterion at a sequence of decreasing temperatures.

The Simulated Annealing scheme used in this work is based on the algorithm by Corana *et al.* [86]. Let's start from an initial guess $\mathbf{X}_1$, an initial temperature T_1, and an initial step length vector $\mathbf{v}_o$. A random move is generated sequentially along each coordinate direction j by $\mathbf{X}' = \mathbf{X}_c + rv_j\mathbf{e}_j$, where $j = 1, \ldots, N$, $\mathbf{X}'$ denotes the trial point, which is either accepted or rejected according to the Metropolis criterion, N denotes the model space dimension, $\mathbf{X}_c$

is the current state, or the latest accepted point, r is a random number drawn uniformly from $[-1, 1]$, v_j is the jth element of the step length vector, and $\mathbf{e}_j$ is the unit vector of the jth coordinate. This set of sequential perturbations is repeated N_s times. The step length is then adjusted according to the Corana algorithm step length adjustment rule (presented at the end of this subsection) and the iteration continues until the number of step length adjustments reaches N_T. Fig. 4.2(a) illustrates the sequential perturbations followed by the step length adjustment. The temperature is reduced at this point by $T_{new} = R_T T_{old}$, where R_T is the reduction factor. The iteration continues at the new temperature starting from the current optimal point. This procedure is illustrated in Fig. 4.2(b), where the current state at each step length adjustment is denoted by $\mathbf{X}_2$, $\mathbf{X}_3$, ..., $\mathbf{X}_{N_T+1}$. Note that the first step length adjustment in each chain happens at $\mathbf{X}_2$ and the last one happens at $\mathbf{X}_{N_T+1}$, which is also the last accepted point of the corresponding chain. It can be shown that if the length of the chains formed by $\mathbf{X}_1$, $\mathbf{X}_2$, ..., $\mathbf{X}_{N_T+1}$ approaches infinity, the Simulated Annealing algorithm converges to a global minimum of the cost function as the temperature approaches zero [87].

The inversion process stops when the cost function value becomes smaller than a value denoted by δ, i.e., $L \leq \delta$, when the number of forward function evaluations reaches a certain number, or when the algorithm converges to local minima for a certain number of times. The Corana algorithm can be modified in order to make it exit a local minimum to which the algorithm has converged. If the value of the cost function at $\mathbf{X}_{N_T+1}$ is L_k^*, the following rule is used to decide whether the algorithm has been trapped in a local minimum.

$$\left| L_k^* - L_{k-i}^* \right| < \varepsilon, \quad i = 1, 2, \ldots, N_\varepsilon \tag{4.6}$$

where the subscripts $k - i$ refer to the previous chains. The quantities ε and N_ε are chosen empirically to achieve the best results. If (4.6) is satisfied, the temperature is increased to make the algorithm exit the local minimum area. To understand this approach, consider the
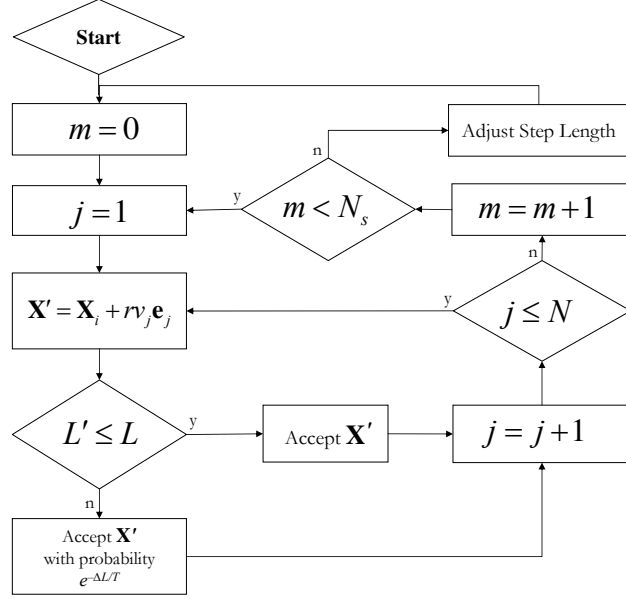
(a)
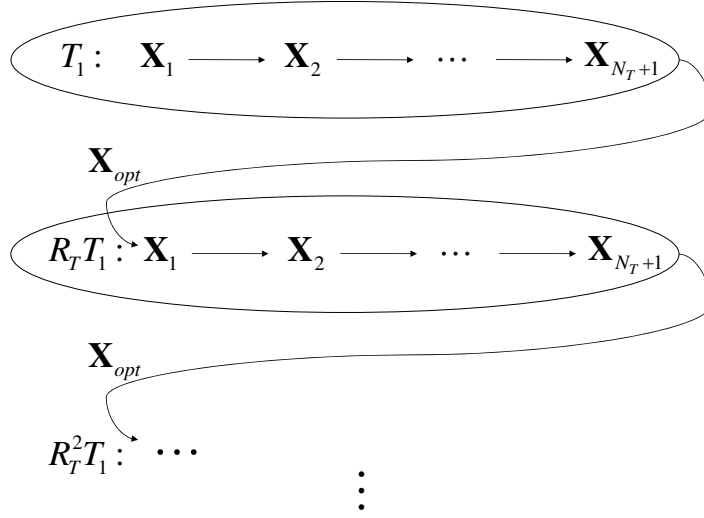
(b)

Figure 4.2: The outline of the Simulated Annealing algorithm used in this work. (a) Random moves are generated sequentially along coordinate directions. (b) Step length is adjusted N_T times at each temperature before the temperature is reduced. The current state at each step length adjustment is denoted by $\mathbf{X}_2$, $\mathbf{X}_3$, ..., $\mathbf{X}_{N_T+1}$.

step length adjustment rule in the Corana algorithm:

$$
v_j' = \begin{cases} v_j \left(1 + c_j \frac{n_j/N_s - 0.6}{0.4}\right) & \text{if } n_j > 0.6N_s \\ v_j \left(1 + c_j \frac{0.4 - n_j/N_s}{0.4}\right)^{-1} & \text{if } n_j < 0.4N_s \end{cases} \tag{4.7}
$$

where $c_j = 2$ for $1 \leq j \leq N$ and n_j $(j = 1, \ldots, N)$ is the number of accepted moves along the jth coordinate since the last step length adjustment. As the temperature decreases, the step length becomes smaller and Corana algorithm concentrates on a smaller area. On the contrary, if the temperature is forced to increase, according to the Metropolis criterion and (4.7), both the step length and the probability of accepting uphill moves increase. Therefore, in a situation where the algorithm has converged to a local minimum, by increasing the temperature, the algorithm is allowed to continue its search for the global minimum with a bigger step length, i.e., in a larger area. This process can be repeated multiple times until convergence to the global minimum is achieved.

4.3.3   Inversion and Measurement Parameters

The constraints on the model parameters are based on existing models and data for soil moisture applications [33, 77], i.e., $3.0 \leq \epsilon_r' \leq 15.0$, $0.0 \leq \sigma \leq 0.1$, $0 \leq \sigma_f \leq 5$ (cm), and $1 \leq l_f \leq 25$ (cm). The constraint on layer thickness, $0.1 \leq d \leq 1.0$ (m), is based on typical observed depths of the root zone, bedrock, and other natural features. These bounds can be modified according to the dielectric model, dielectric structure, and application. Table 4.2 summarizes these bounds.

The inversion parameters used in the algorithm are T_1, N_s, N_T, R_T, δ, ε, N_ε, and $\mathbf{v}_o$ introduced in Section 4.3.2. The process of choosing inversion parameters that would improve the inversion results is the subject of much investigation. The values of N_s, N_T, R_T used here are the values recommended by Corana *et al.*, i.e., 20, 100, and 0.85, respectively. The values of T_1, δ, ε, N_ε, and $\mathbf{v}_o(j)$, the jth element of $\mathbf{v}_o$, are derived empirically to achieve the best results. Note that it can easily be verified that the algorithm performance is independent of the initial guess if the above values of the inversion parameters are chosen. Table 4.3 summarizes the inversion parameters.

The measurement parameters are the frequency and observation angle. The algorithm is ultimately intended for use with radar data from an experimental tower-based instrument designed for estimation of subsurface soil moisture. Therefore, the frequencies used in the inverse model are the same frequencies available from the MOSS tower radar system, i.e.,

$f_1 = 120.0$, $f_2 = 137.0$, $f_3 = 150.0$, $f_4 = 420.0$, $f_5 = 435.0$, and $f_6 = 450.0$ MHz. These frequencies are centered at 137 and 435 MHz. The radar antenna is a log-periodic one, which has a rather wide beam. This beam can be focused at various locations, providing different incidence angles. The measurement angles are chosen to be $\theta_1 = 30°$ and $\theta_2 = 45°$. The choice of measurement angles used in the inversion process is based on a qualitative analysis. Since σ_{vv}^o and σ_{hh}^o are equal at $\theta = 0$, observing the difference between σ_{vv}^o and σ_{hh}^o versus measurement angle and looking for angles at which this difference is large, provides insight. Fig. 4.3 shows $|\sigma_{vv}^o - \sigma_{hh}^o|$ versus the measurement angle θ at several frequencies that are centered at 137 MHz and 435 MHz for a case where $\epsilon_{2r}' = 2\epsilon_{1r}' = 10.0$, $\sigma_2 = 2\sigma_1 = 0.01$, $d = 0.2$, $l_{f_1} = l_{f_2} = 0.2$, and $\sigma_{f_1} = \sigma_{f_2} = 0.02$. Based on this information and other similar simulation scenarios, $30°$ and $45°$ are chosen as the measurement angles. Therefore, if, for example, $N_f = 2$ and $N_\theta = 2$, then in (4.5), $f_1 = 120.0$, $f_2 = 137.0$, $\theta_1 = 30°$, and $\theta_2 = 45°$. Table 4.4 summarizes the measurement parameters used in the inversion process.

Table 4.2: Constraints on the model parameters. Units are SI.

	ϵ_{1r}'	σ_1	ϵ_{2r}'	σ_2	d	l_{f_1}	σ_{f_1}	l_{f_2}	σ_{f_2}
Lower Bound ($\mathbf{X}_l$)	3.0	0.0	3.0	0.0	0.1	0.01	0.0	0.01	0.0
Upper Bound ($\mathbf{X}_u$)	15.0	0.1	15.0	0.1	1.0	0.25	0.05	0.25	0.05

Table 4.3: Inversion parameters

T_1	N_s	N_T	R_T	c_j	δ	ε	N_ε	$\mathbf{v}_o(j)$
$100,000$	20	100	0.85	2.0	10^{-12}	10^{-10}	10	$\mathbf{X}_u(j) - \mathbf{X}_l(j)$

Table 4.4: Measurement parameters

f_1	f_2	f_3	f_4	f_5	f_6	θ_1	θ_2
120 MHz	137 MHz	150 MHz	420 MHz	435 MHz	450 MHz	$30°$	$45°$

4.4 Inversion Results

4.4.1 5-Parameter Problem

Let's start with the assumption that the first 5 parameters, i.e., ϵ_{1r}', σ_1, ϵ_{2r}', σ_2, and d, are unknown, because we are usually most interested in these 5 parameters and less interested in the statistical properties of the interfaces.
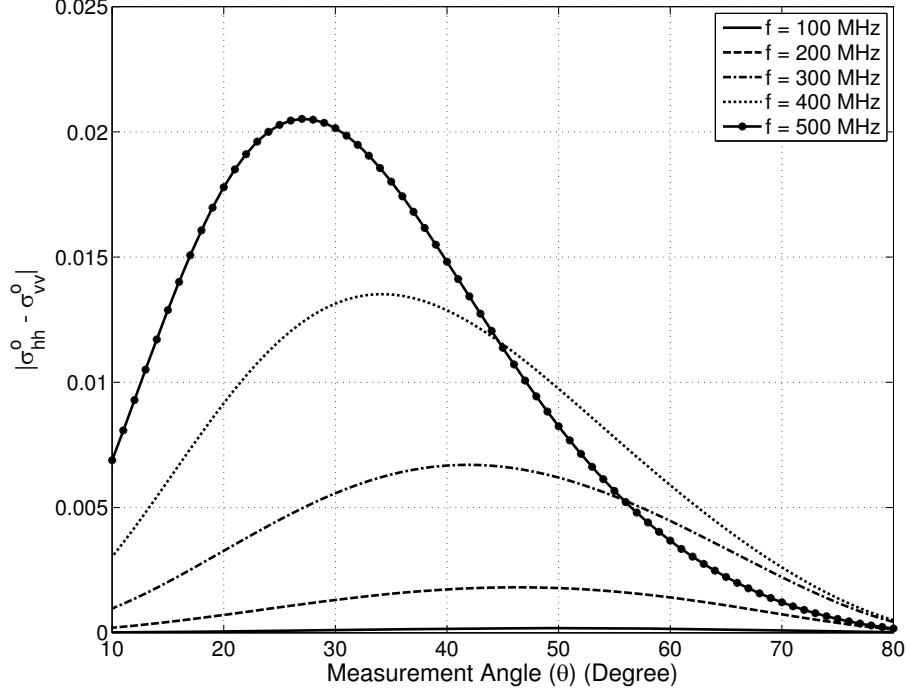
Figure 4.3: Maximizing $|\sigma^o_{hh} - \sigma^o_{vv}|$ with respect to measurement angle at different frequencies centered at 137 and 435 MHz. It is assumed that $\epsilon'_{2r} = 2\epsilon'_{1r} = 10.0$, $\sigma_2 = 2\sigma_1 = 0.01$, $d = 0.2$, $l_{f_1} = l_{f_2} = 0.2$, and $\sigma_{f_1} = \sigma_{f_2} = 0.02$. Based on this qualitative analysis and similar simulations, $30°$ and $45°$ are chosen as the measurement angles.

Fig. 4.4 shows the inversion result for a case where $\epsilon'_{1r} = 4.00$, $\sigma_1 = 2.0 \times 10^{-2}$, $\epsilon'_{2r} = 12.00$, $\sigma_2 = 1.0 \times 10^{-1}$, and $d = 0.40$. The known parameters are assumed to be $l_{f_1} = 0.5l_{f_2} = 0.1$ and $\sigma_{f_1} = 2\sigma_{f_2} = 0.02$. This case is referred to as Case 1 hereafter. This figure shows the relative error in the current value and the optimum value of $\mathbf{X}(1) = \epsilon'_{1r}$. *Current Value* refers to the value of the model parameter in the last accepted state in each chain, i.e., $\mathbf{X}_{N_T+1}$. *Optimum Value* refers to the value of the model parameter in the current optimum state in a chain, denoted by $\mathbf{X}_{opt}$ in Fig. 4.2(b). It is observed that the algorithm may accept bad solutions in terms of relative error in the model parameter, but ultimately converges to the right solution.

Fig. 4.5 shows the inversion result for another case where $\epsilon'_{1r} = 5.00$, $\sigma_1 = 5.0 \times 10^{-2}$, $\epsilon'_{2r} = 10.00$, $\sigma_2 = 1.0 \times 10^{-1}$, and $d = 0.20$. The known parameters are assumed to be $l_{f_1} = 0.5l_{f_2} = 0.1$ and $\sigma_{f_1} = 2\sigma_{f_2} = 0.02$. This case is referred to as Case 2 hereafter. It is
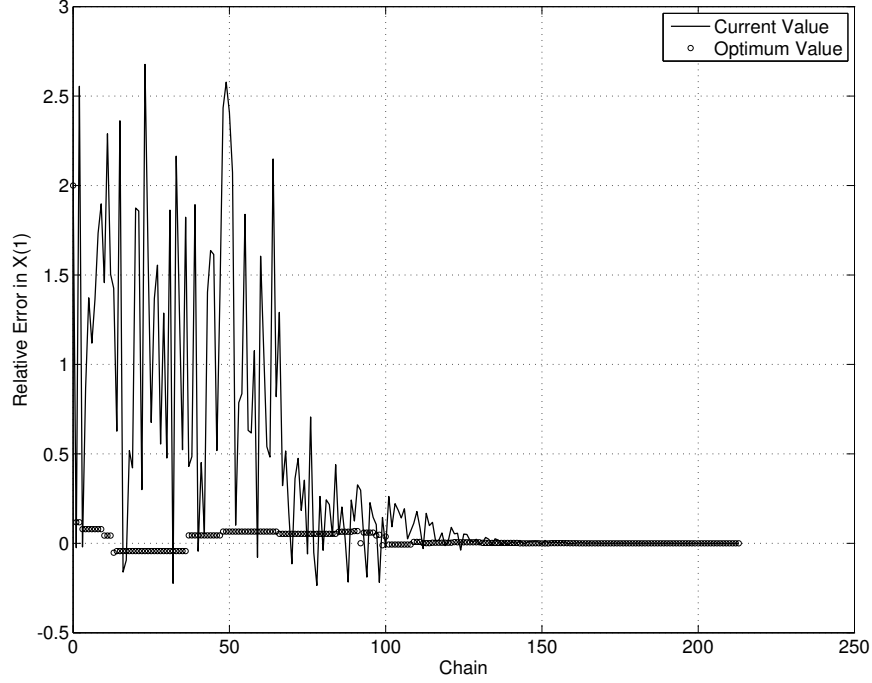
Figure 4.4: Relative error in the current value and optimum value of $X(1) = \epsilon'_{1r}$ as the Simulated Annealing algorithm progresses. The layers dielectric properties and the layer thickness are the unknown model parameters while the boundaries statistical properties are assumed known (Case 1, 5-parameter problem). Actual model parameters: $\epsilon'_{1r} = 4.00$, $\sigma_1 = 2.0 \times 10^{-2}$, $\epsilon'_{2r} = 12.00$, $\sigma_2 = 1.0 \times 10^{-1}$, $d = 0.40$, $l_{f_1} = 0.5 l_{f_2} = 0.1$, $\sigma_{f_1} = 2\sigma_{f_2} = 0.02$. Refer to Table 4.6.

apparent from this figure that the algorithm has increased the temperature 4 times in this case to achieve the correct result. Table 4.5 summarizes Case 1 and Case 2.

Table 4.5: The two cases of the true values used for simulations in Sections 4.4.1, 4.4.3, 4.4.4. Units are SI.

	ϵ'_{1r}	σ_1	ϵ'_{2r}	σ_2	d	l_{f_1}	σ_{f_1}	l_{f_2}	σ_{f_2}
Case 1	4.00	2.0×10^{-2}	12.00	1.0×10^{-1}	0.40	0.1	0.02	0.2	0.01
Case 2	5.00	5.0×10^{-2}	10.00	1.0×10^{-1}	0.20	0.1	0.02	0.2	0.01

Table 4.6 and Table 4.7 show the actual values and initial guess in each case as well as the final inversion results. The quantity N_{fcnevl} is the total number of forward function evaluations and *Number of Jumps* refers to the number of times that the temperature has
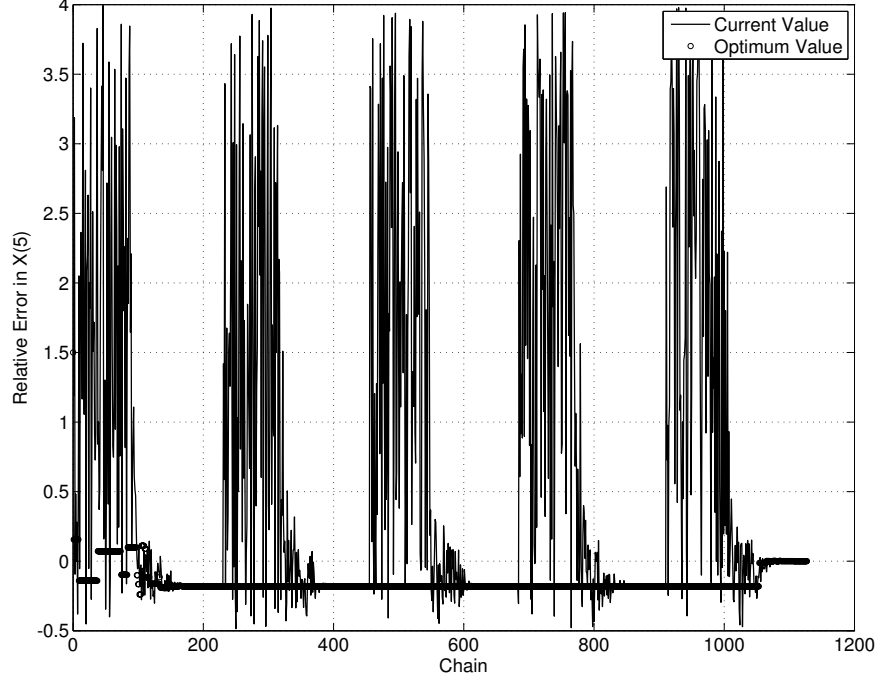
Figure 4.5: Relative error in the current value and optimum value of $X(5) = d$ as the Simulated Annealing algorithm progresses. The layers dielectric properties and the layer thickness are the unknown model parameters while the boundaries statistical properties are assumed known (Case 2, 5-parameter problem). The temperature has been increased 4 times to make the algorithm converge to the global minimum. Actual model parameters: $\epsilon'_{1r} = 5.00$, $\sigma_1 = 5.0 \times 10^{-2}$, $\epsilon'_{2r} = 10.00$, $\sigma_2 = 1.0 \times 10^{-1}$, $d = 0.20$, $l_{f_1} = 0.5 l_{f_2} = 0.1$, $\sigma_{f_1} = 2\sigma_{f_2} = 0.02$. Refer to Table 4.7.

been increased. Note that the total number of cost function evaluations is $N_{\text{fcnevl}}/N_f N_\theta$. In the majority of the cases of the 5-parameter problem that were simulated, it was observed that the combination $N_f = 3$ and $N_\theta = 2$ would lead to good results.

Each complete simulation case could take from a few minutes to a few hours depending on the number of unknown parameters, number of forward function evaluations (which is directly proportional to the product of number of frequency points and number of measurement angles), measurement noise, and the specific machine used. For example, Case 1 and Case 2 took 12 and 65 minutes, respectively, on an AMD Opteron 240, 1.4 GHz CPU with 1MB cache. When the number of unknown model parameters are 7 and 9 in Case 1, computation time is 25 minutes and 100 minutes, respectively, on the same CPU.

Table 4.6: Actual values, initial guess, and inversion results (Case 1, 5-parameter problem). Units are SI.

	ϵ'_{1r}	σ_1	ϵ'_{2r}	σ_2	d
True Value	4.00	2.0×10^{-2}	12.00	1.0×10^{-1}	0.40
Initial Guess	12.00	6.0×10^{-2}	4.00	1.0×10^{-2}	0.10
Final Value	4.00	2.0×10^{-2}	12.00	1.0×10^{-1}	0.40

N_f	N_θ	T_{final}	N_{fcnevl}	L_{min}	Number of Jumps
3	2	0.11×10^{-9}	$12,721,494$	0.70×10^{-12}	0

Table 4.7: Actual values, initial guess, and inversion results (Case 2, 5-parameter problem). Units are SI.

	ϵ'_{1r}	σ_1	ϵ'_{2r}	σ_2	d
True Value	5.00	5.0×10^{-2}	10.00	1.0×10^{-1}	0.20
Initial Guess	14.00	8.0×10^{-2}	4.00	1.0×10^{-2}	0.50
Final Value	5.00	5.0×10^{-2}	10.00	1.0×10^{-1}	0.20

N_f	N_θ	T_{final}	N_{fcnevl}	L_{min}	Number of Jumps
3	2	0.66×10^{-10}	$67,596,486$	0.92×10^{-12}	4

4.4.2 Sensitivity Analysis

The assumption that the statistical properties of the rough interfaces are known can cause the final error to be large, because in a 5-parameter problem, the values assigned to $\mathbf{X}(6) = l_{f_1}$ through $\mathbf{X}(9) = \sigma_{f_2}$ are *a-priori* while these parameters could have noticeable impact on the backscattering coefficients. To observe the impact of one parameter on the output, we may monitor the output of the forward model while changing the value of that parameter and keeping the values of the other parameters fixed. For example, Fig. 4.6 shows the sensitivity of the backscattering coefficient σ^o_{vv} to the model parameters for a case where the layers are lossless. The plots show that the backscattered power is more sensitive to the first layer dielectric properties and that the statistical properties of the second layer have a smaller effect on the backscattered power. The measurement parameters are $f = 137.0$ MHz and $\theta = 45°$. When the value of a model parameter is varied, the other model parameters are fixed at $\epsilon'_{2r} = 2\epsilon'_{1r} = 10.0$, $\sigma_2 = \sigma_1 = 0.0$, $d = 1.0$ (m), $l_{f_1} = l_{f_2} = 10.0$ (cm), and $\sigma_{f_1} = \sigma_{f_2} = 3.0$ (cm).

Loss in the first layer can mask the effect of the second layer interface. Fig. 4.7 shows

the sensitivity analysis results for a case where $\sigma_2 = 2\sigma_1 = 0.01$ and where all of the other parameters are the same as in Fig. 4.6. It is observed that even a small amount of loss has masked the effect of the second layer interface. However, increasing the contrast between the layers can nullify the effect of loss in the first layer. Fig. 4.8 shows a case where all of the parameters are the same as in Fig. 4.7 except that $\epsilon'_{2r} = 20.0$ and $\sigma_2 = 0.1$, which implies more contrast between the two layers. The added contrast has made the impact of the second interface statistical properties larger.
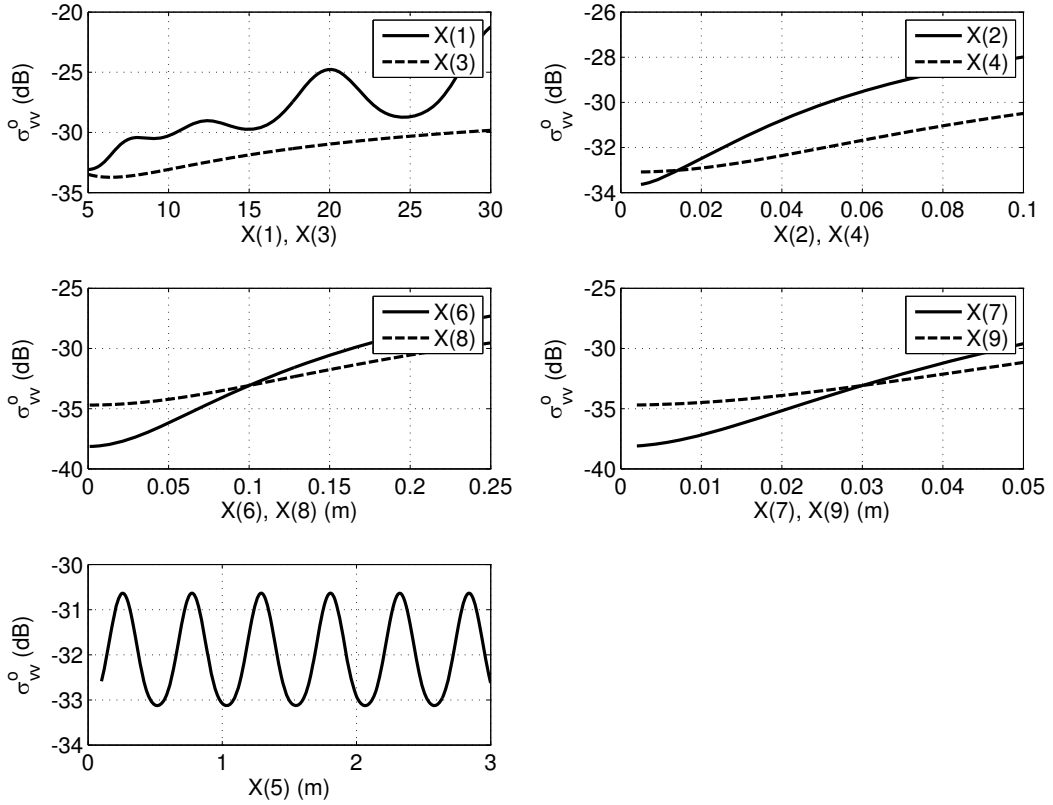
Figure 4.6: Sensitivity of the backscattering coefficient σ^o_{vv} to the model parameters. Baseline values: $\epsilon'_{2r} = 2\epsilon'_{1r} = 10$, $\sigma_2 = \sigma_1 = 0.0$, $d = 1.0$ (m), $l_{f_1} = l_{f_2} = 10$ (cm), $\sigma_{f_1} = \sigma_{f_2} = 3$ (cm). Measurement parameters: $f = 137.0$ MHz and $\theta = 45°$.
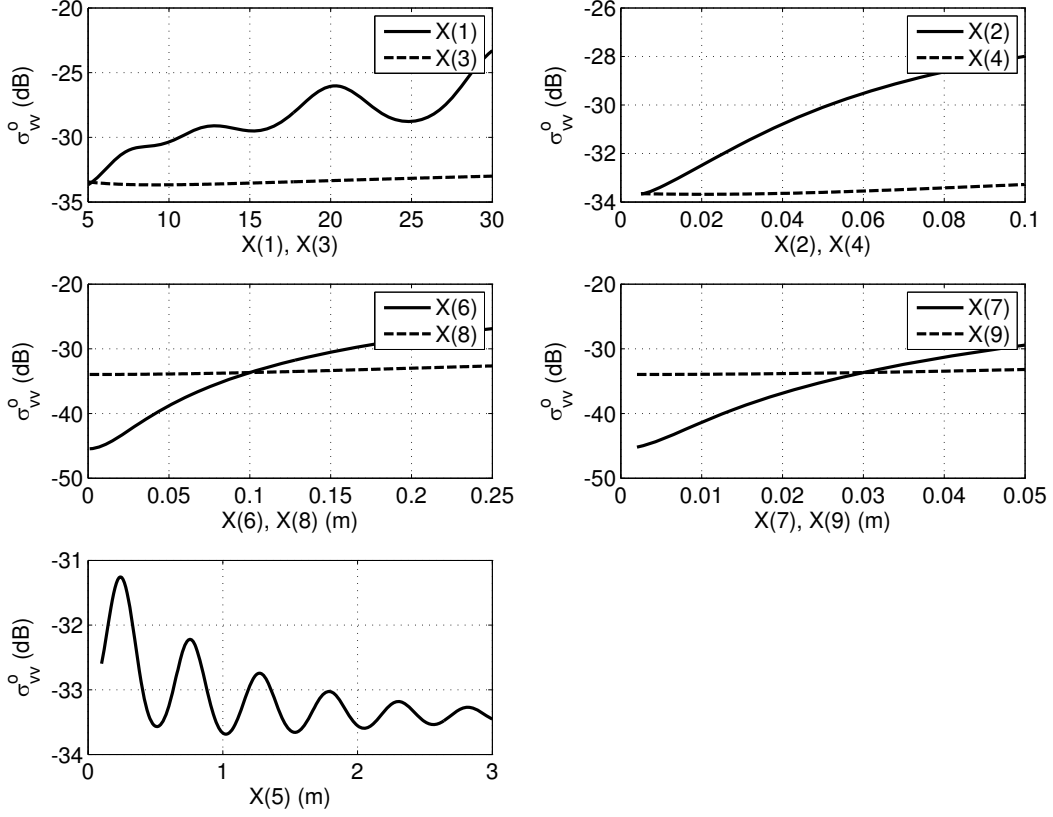
Figure 4.7: Sensitivity of the backscattering coefficient σ^o_{vv} to the model parameters. Baseline values: $\epsilon'_{2r} = 2\epsilon'_{1r} = 10$, $\sigma_2 = 2\sigma_1 = 0.01$, $d = 1.0$ (m), $l_{f_1} = l_{f_2} = 10$ (cm), $\sigma_{f_1} = \sigma_{f_2} = 3$ (cm). Measurement parameters: $f = 137.0$ MHz and $\theta = 45°$.

4.4.3 7-Parameter Problem

A simple simulation shows that a 50% error in the *a-priori* values assigned to l_{f_1}, σ_{f_1}, l_{f_2}, and σ_{f_2} would result in, for example, -100% error in σ_1 in Case 1 and -100% error in σ_2 in Case 2. To account for the impact of the error in the *a-priori* values assigned to the statistical properties of the boundaries, i.e., l_{f_1}, σ_{f_1}, l_{f_2}, and σ_{f_2}, let's consider $\mathbf{X}(1) = \epsilon'_{1r}$ through $\mathbf{X}(7) = \sigma_{f_1}$ as unknown in Case 1 of Section 4.4.1. Fig. 4.9 shows the inversion results. Only the optimum value of the model parameters is shown in this figure. Table 4.8 summarizes the actual values and initial guess as well as the final inversion results. In the majority of the cases of the 7-parameter problem that were simulated, it was observed that
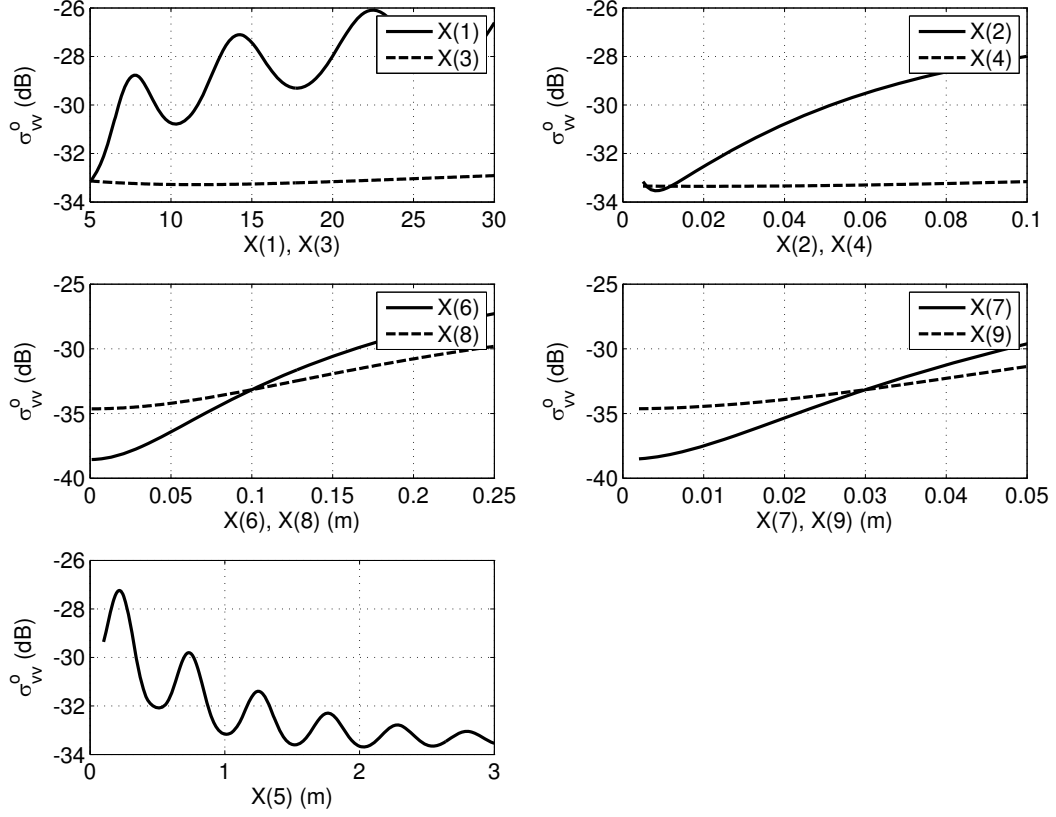
Figure 4.8: Sensitivity of the backscattering coefficient σ_{vv}^o to the model parameters. Baseline values: $\epsilon_{2r}' = 4\epsilon_{1r}' = 20$, $\sigma_2 = 20\sigma_1 = 0.1$, $d = 1.0$ (m), $l_{f_1} = l_{f_2} = 10$ (cm), $\sigma_{f_1} = \sigma_{f_2} = 3$ (cm). Measurement parameters: $f = 137.0$ MHz and $\theta = 45°$.

$N_f = 4$ and $N_\theta = 2$ would lead to good results.

Table 4.8: Actual values, initial guess, and inversion results (Case 1, 7-parameter problem). Units are SI.

	ϵ_{1r}'	σ_1	ϵ_{2r}'	σ_2	d
True Value	4.00	2.0×10^{-2}	12.00	1.0×10^{-1}	0.40
Initial Guess	12.00	6.0×10^{-2}	4.00	1.0×10^{-2}	0.10
Final Value	4.00	2.0×10^{-2}	12.00	1.0×10^{-1}	0.40

N_f	N_θ	T_{final}	N_{fcnevl}	L_{min}	Number of Jumps
4	2	6.9×10^{-12}	$25,657,440$	0.70×10^{-12}	0
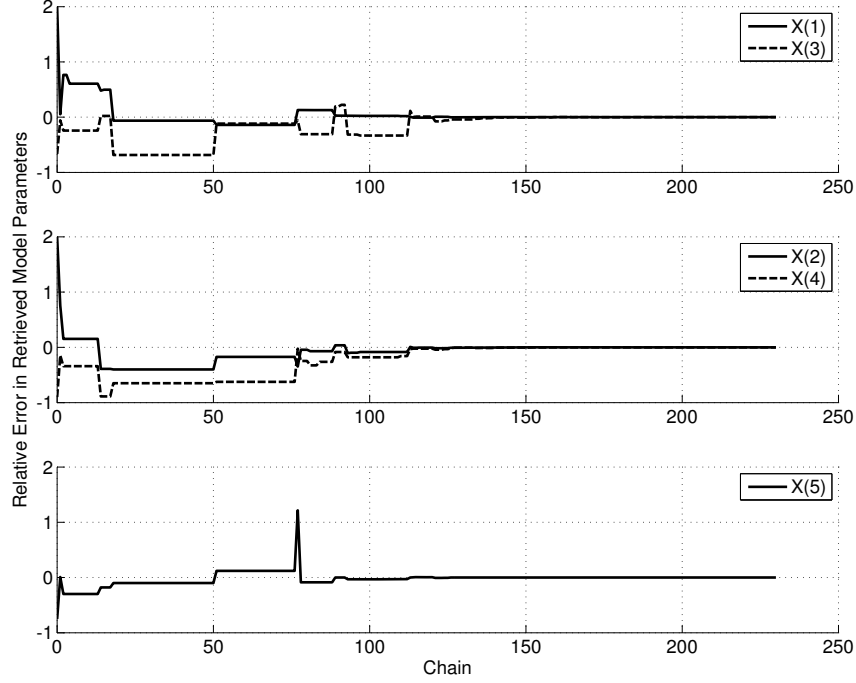
Figure 4.9: Relative error in the optimum value of $\mathbf{X}(1) = \epsilon'_{1r}$, $\mathbf{X}(2) = \sigma_1$, $\mathbf{X}(3) = \epsilon'_{2r}$, $\mathbf{X}(1) = \sigma_2$, and $\mathbf{X}(5) = d$ as the Simulated Annealing algorithm progresses. The layers dielectric properties, the thickness, and the first boundary statistical properties are the unknown model parameters while the second boundary statistical properties are assumed known (Case 1, 7-parameter problem). Refer to Table 4.8.

4.4.4   9-Parameter Problem

Simulations show that a 50% error in the *a-priori* values assigned to l_{f_2} and σ_{f_2} would result in, for example, 110% error in d in Case 1 and -20% error in ϵ'_{2r} in Case 2. These errors are smaller compared to the ones in the 5-parameter problem with the same amount of error in the *a-priori* values. However, these output errors are still large and to avoid them, all of the model parameters are now considered as unknown.

Let's first consider Case 1 in Section 4.4.1. Fig. 4.10 shows the inversion results. Table 4.9 summarizes the actual values and initial guess as well as the final inversion results. In the 9-parameter problem, it was observed that $N_f = 5$ and $N_\theta = 2$ would lead to good results in the majority of the simulated cases.

To show the performance of the algorithm in inversion of the model parameters, several
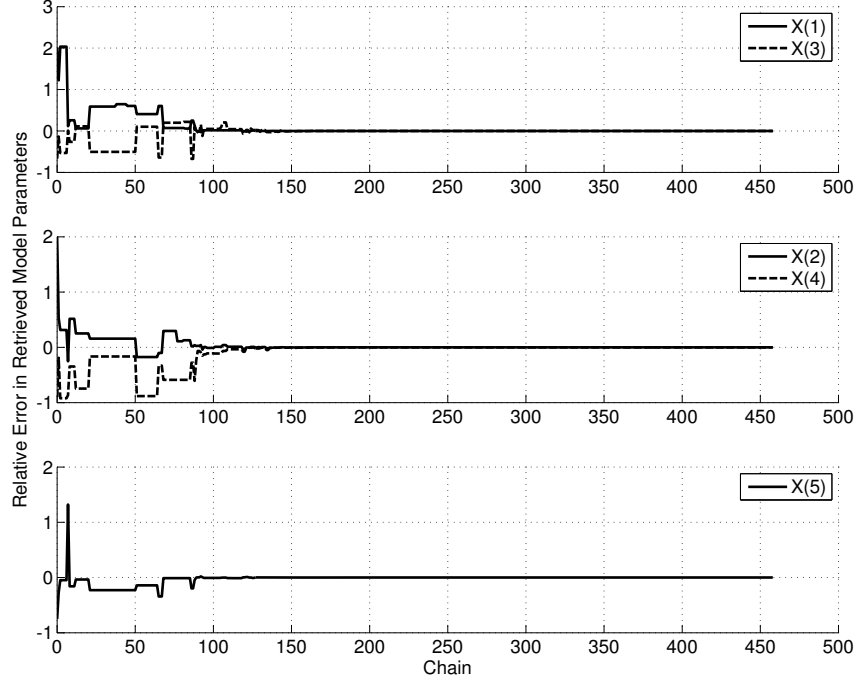
Figure 4.10: Relative error in the optimum value of $\mathbf{X}(1) = \epsilon'_{1r}$, $\mathbf{X}(2) = \sigma_1$, $\mathbf{X}(3) = \epsilon'_{2r}$, $\mathbf{X}(1) = \sigma_2$, and $\mathbf{X}(5) = d$ as the Simulated Annealing algorithm progresses. All of the model parameters are considered unknown (Case 1, 9-parameter problem). The algorithm has increased the temperature 1 time. Refer to Table 4.9.

Table 4.9: Actual values, initial guess, and inversion results (Case 1, 9-parameter problem). Units are SI.

	ϵ'_{1r}	σ_1	ϵ'_{2r}	σ_2	d
True Value	4.00	2.0×10^{-2}	12.00	1.0×10^{-1}	0.40
Initial Guess	12.00	6.0×10^{-2}	4.00	1.0×10^{-2}	0.10
Final Value	4.00	2.0×10^{-2}	12.00	1.0×10^{-1}	0.40

N_f	N_θ	T_{final}	N_{fcnevl}	$L_{\min}$	Number of Jumps
5	2	9.5×10^{-12}	$82,260,040$	0.90×10^{-12}	1

cases are simulated as follows and the final errors in $\mathbf{X}(1) = \epsilon'_{1r}$, $\mathbf{X}(3) = \epsilon'_{2r}$, and $\mathbf{X}(5) = d$ are presented. A baseline case is chosen where $\epsilon'_{1r} = 6.00$, $\sigma_1 = \epsilon'_{1r}/150 = 0.04$, $\epsilon'_{2r} = 12.00$, $\sigma_2 = \epsilon'_{2r}/150 = 0.08$, $d = 0.4$, $l_{f_1} = 0.5 l_{f_2} = 0.1$ and $\sigma_{f_1} = 2\sigma_{f_2} = 0.04$. Then, the true value of one of the three parameters ϵ'_{1r}, ϵ'_{2r}, and d is varied while the other two are assumed to have their baseline values. The true values of ϵ'_{1r} are 3.0, 4.0,...,15.0, the true values of ϵ'_{2r}

are 3.0, 3.5, 4.0, 4.5, 5.0, 5.5, 6.0, 7.0,...,15.0, and the true values of d are 0.2, 0.3,...,1.0. These variations of true value result in 36 cases. Note that while σ_1 and σ_2 are considered unknown, their true values are assumed to be $\epsilon'_{1r}/150$ and $\epsilon'_{2r}/150$, respectively.

Fig. 4.11, Fig. 4.12, and Fig. 4.13 show the final values of ϵ'_{1r}, ϵ'_{2r}, and d versus their actual values. While the algorithm shows a great performance in inverting all of the model parameters, especially ϵ'_{1r} and σ_1, in a small number of these cases, as indicated in the figures, significant errors in ϵ'_{2r}, σ_2, and d are observed. Similarly good results are obtained for the other unknowns.
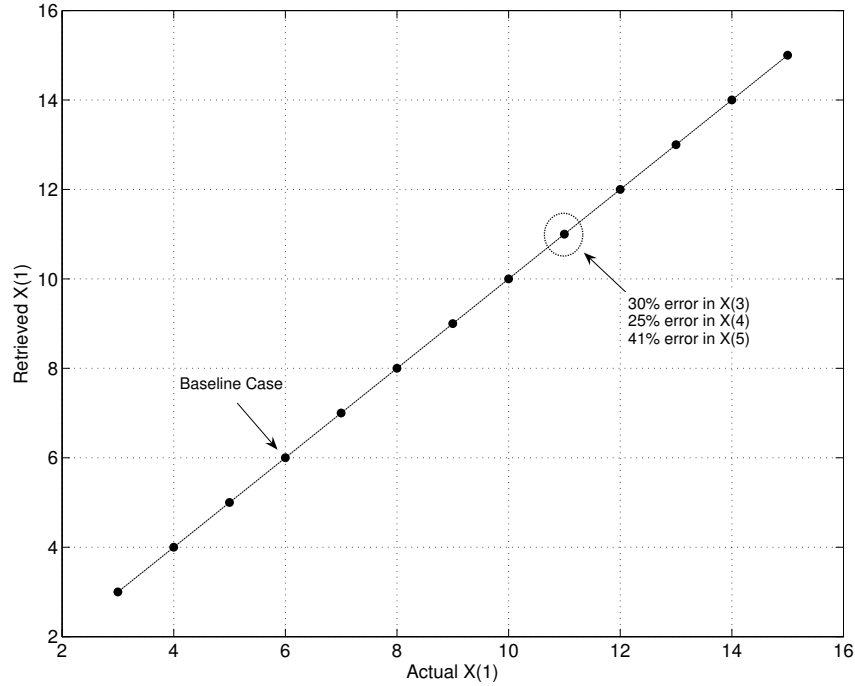
Figure 4.11: Error in the retrieved model parameter $\mathbf{X}(1) = \epsilon'_{1r}$ for the cases simulated in Section 4.4.4. The true values of ϵ'_{1r} are varied while the other model parameters (except for σ_1) are fixed at their baseline values. The true value of σ_1 is assumed to be $\epsilon'_{1r}/150$.

4.4.5 Discussion

The presented results show that the method of Simulated Annealing is a powerful tool for retrieval of the subsurface properties of a two-layer rough surface structure. We observed

100
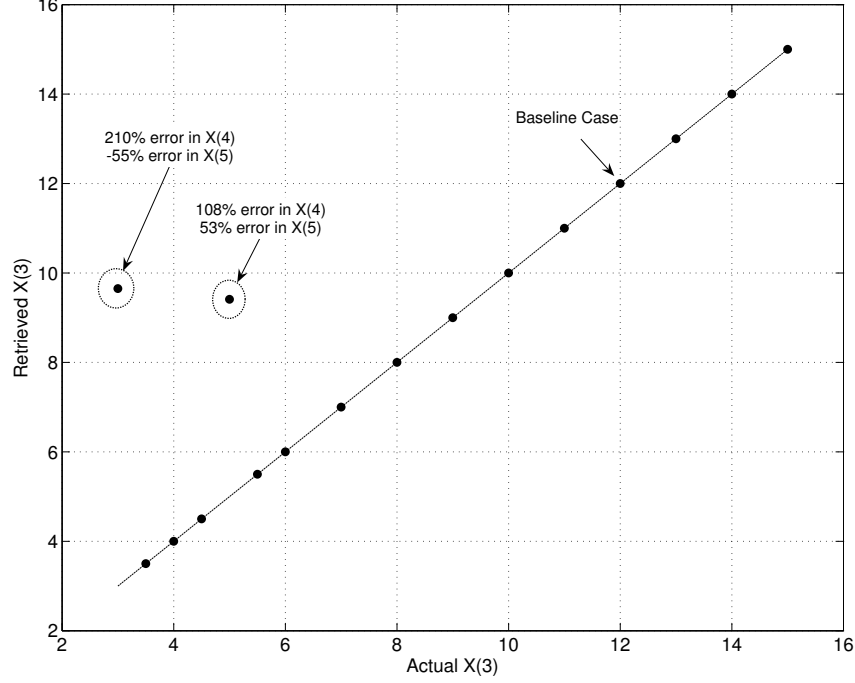
Figure 4.12: Error in the retrieved model parameter $\mathbf{X}(3) = \epsilon'_{2r}$ for the cases simulated in Section 4.4.4. The true values of ϵ'_{2r} are varied while the other model parameters (except for σ_2) are fixed at their baseline values. The true value of σ_2 is assumed to be $\epsilon'_{2r}/150$.

significant errors in the retrieved $\mathbf{X}(3) = \epsilon'_{2r}$, $\mathbf{X}(4) = \sigma_2$, and $\mathbf{X}(5) = d$ in very few cases, but the errors in the retrieved $\mathbf{X}(1) = \epsilon'_{1r}$ and $\mathbf{X}(2) = \sigma_1$ were always small.

The inversion parameters presented in Table 4.3 are either recommendations by Corana *et al.* [86] or recommendations derived empirically in this work. The measurement parameters, i.e., frequency points and measurement angles, are based on the specifications of the MOSS tower radar [19] and the simple analysis presented in Section 4.3.3, respectively.

The quantities N_f and N_θ, which are the number of frequency points and the number of measurement angles, respectively, are key to successful retrieval. These numbers affect both the smoothness and information content of the cost function. The values of N_f and N_θ in this chapter are based on several inversion cases with different number of unknown model parameters. However, the optimum values of these parameters as well as the values of the frequency points and measurement angles, with the number of cost function evaluations
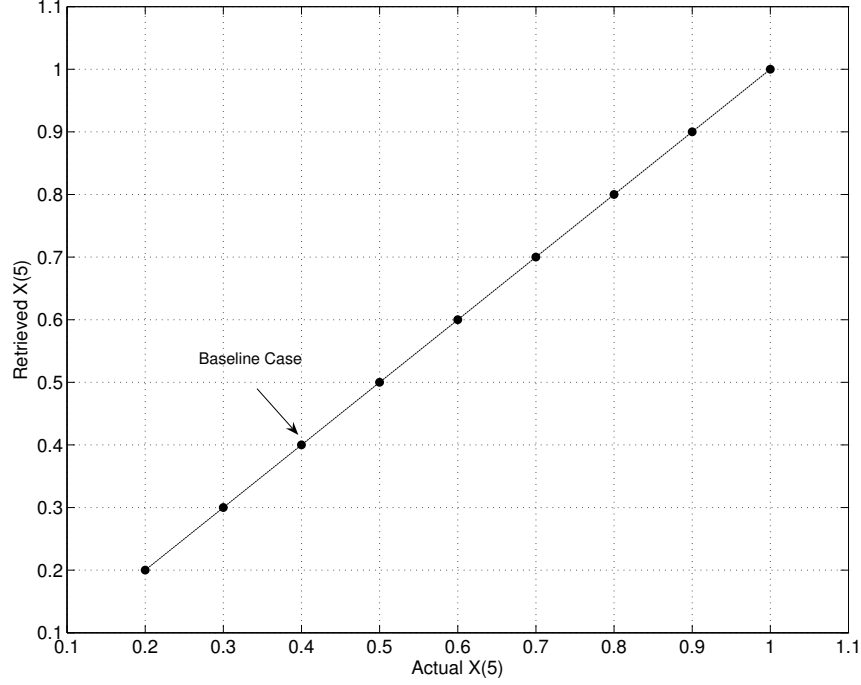
Figure 4.13: Error in the retrieved model parameter $\mathbf{X}(5) = d$ for the cases simulated in Section 4.4.4. The true values of d are varied while the other model parameters are fixed at their baseline values.

being a constraint, could be explored further.

4.5 Noise Analysis

As mentioned in Section 4.4.1 and Section 4.4.3, the results would suffer from large errors if only a subset of the model parameters are treated as unknown and imperfect *a-priori* values are assigned to the rest of the model parameters. Therefore, the noise analysis results are presented assuming all of the 9 model parameters are unknown.

Assuming the measured scattered power is contaminated by noise, the inversion algorithm is evaluated in presence of Gaussian noise. The noisy data is modeled as

$$\sigma_n^o = \sigma^o + \Delta \times N(0,1) \times \sigma^o \tag{4.8}$$

where σ_n^o is the noise contaminated data point, σ^o is the synthesized noise free data point predicted by the forward model, Δ is the additive noise standard deviation, and $N(0, 1)$ represents a random number drawn from a normal distribution with a zero mean and unit standard deviation.

We should note that noise contaminates the received voltage, not the power. However, this analysis, which assumes the backscattered coefficients are contaminated by Gaussian noise directly, offers insight into the sensitivity of the inversion algorithm when the measured data deviate from what the forward model predicts. If we consider a noise model where Gaussian noise contaminates the measured voltage, Δ in the received power would correspond to the larger value of $\sqrt{\Delta}$ in the received voltage. In other words, larger than normal data perturbations are considered here. For instance, a Δ of 0.05 (5% noise) would correspond to a significant amount of noise, which if expressed in terms of signal to noise ratio (SNR), would give a value of < 20 dB. This SNR can easily be achieved and surpassed in realistic radar systems. An SNR of 30 dB, which is also achievable in current radar systems, would correspond to less than 1% noise in this assessment.

Two cases, designated as Case 3 and Case 4, are simulated. These cases are presented in Table 4.10 assuming different values for Δ. The inversion algorithm is run 50 times for each case of the model parameters and noise standard deviation. The average and standard deviation of the relative output error for $\mathbf{X}(1)$ through $\mathbf{X}(5)$ are plotted. Fig. 4.14 and Fig. 4.15 show these results. The inversion parameters are the same as in Table 4.4 except that $N_\varepsilon = 5$.

Table 4.10: The two cases of the true values used for simulations in Section 4.5. Units are SI.

	ϵ'_{1r}	σ_1	ϵ'_{2r}	σ_2	d	l_{f_1}	σ_{f_1}	l_{f_2}	σ_{f_2}
Case 3	5.00	1.0×10^{-2}	10.00	2.0×10^{-2}	0.50	0.1	0.02	0.2	0.01
Case 4	5.00	5.0×10^{-2}	10.00	1.0×10^{-1}	0.30	0.1	0.02	0.2	0.01

We should consider the fact that the performance of the inversion algorithm has been tested in presence of extremely large noise amplitudes. Nevertheless, the noise analysis results suggest that $\mathbf{X}(3) = \epsilon_{2r}$ and $\mathbf{X}(5) = d$ are retrieved with reasonably small error ($< 20\%$) for all noise amplitudes considered. Large standard deviations in most cases, especially in
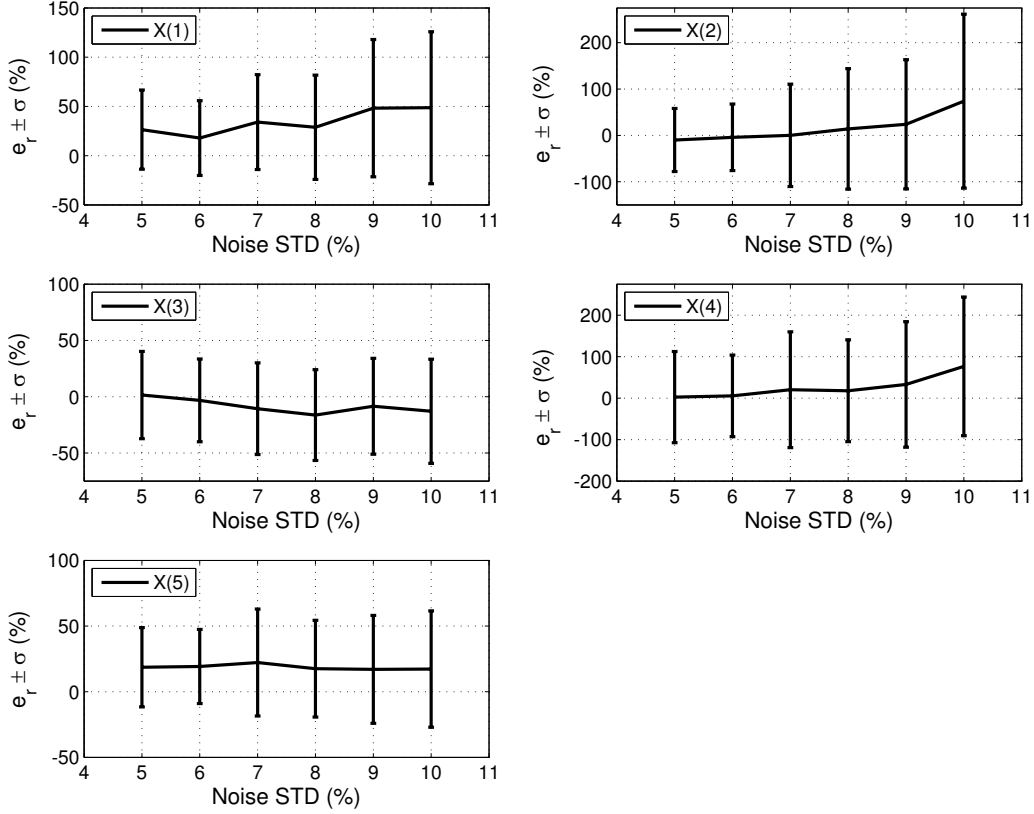
Figure 4.14: Average and standard deviation of the output error at 6 different noise strengths (5%, 6%, 7%, 8%, 9%, and 10%) for Case 3 (See Table 4.10). Number of realizations is 50.

cases where the average output error is small, suggest that we cannot rely on the average output error as the only piece of information about the retrieved model parameters. Other measures of sensitivity to noise are, for example, the most probable point and distribution of the output error. These measures are easily presented by the histogram of the output error. Case 1 and Case 2, presented in Table 4.10, are simulated assuming 5% Gaussian noise, i.e., $\Delta = 0.05$. The inversion algorithm is run 100 times and the histograms of the output for $\mathbf{X}(1)$ through $\mathbf{X}(5)$ are plotted. Fig. 4.16 and Fig. 4.17 show these histograms. An immediate conclusion from these histograms is that as far as the *most probable point* is concerned, all of the model parameters, except for $\mathbf{X}(3)$, are retrieved with small deviation from the average.
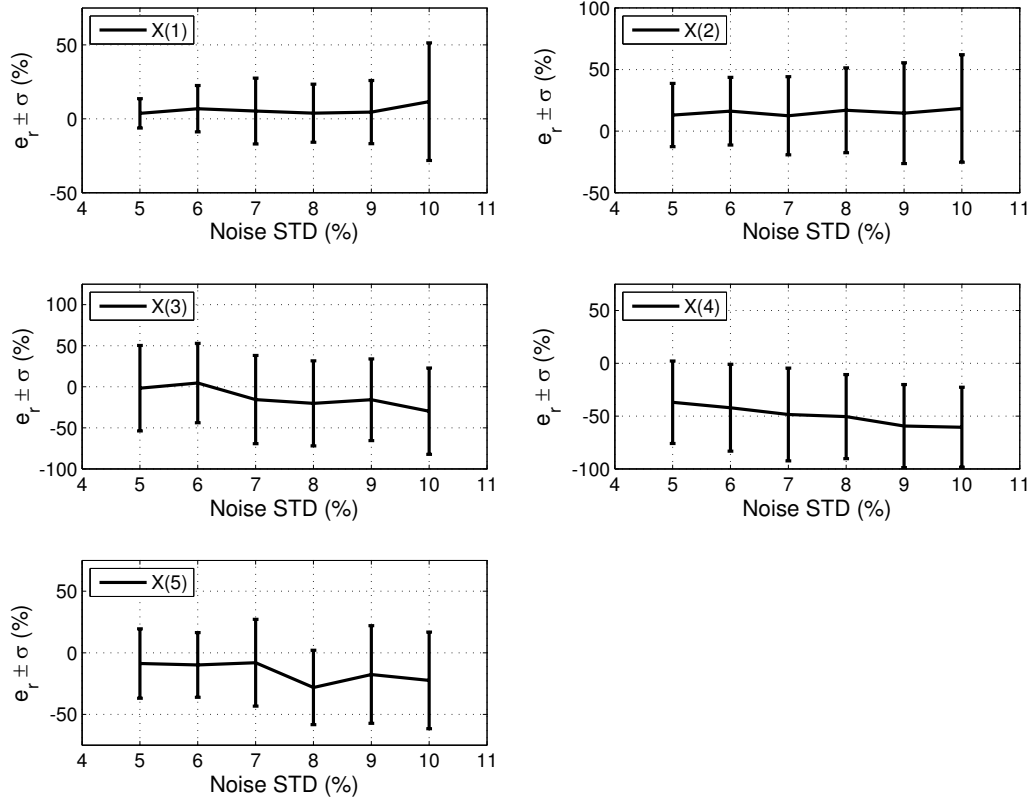
Figure 4.15: Average and standard deviation of the output error at 6 different noise strengths (5%, 6%, 7%, 8%, 9%, and 10%) for Case 4 (See Table 4.10). Number of realizations is 50.

We can use another noise model in which the Gaussian noise contaminates the received voltage. Assume

$$v_n = v + \Delta \times N \times v \tag{4.9}$$

where v denotes the noise free voltage and v_n denotes the measured voltage received at the antenna. We then have

$$v_n^2 = v^2 + 2v\Delta N + \Delta^2 N^2 v^2 \tag{4.10}$$

Averaging (4.10) over realizations of the rough surface with the assumption that N and v
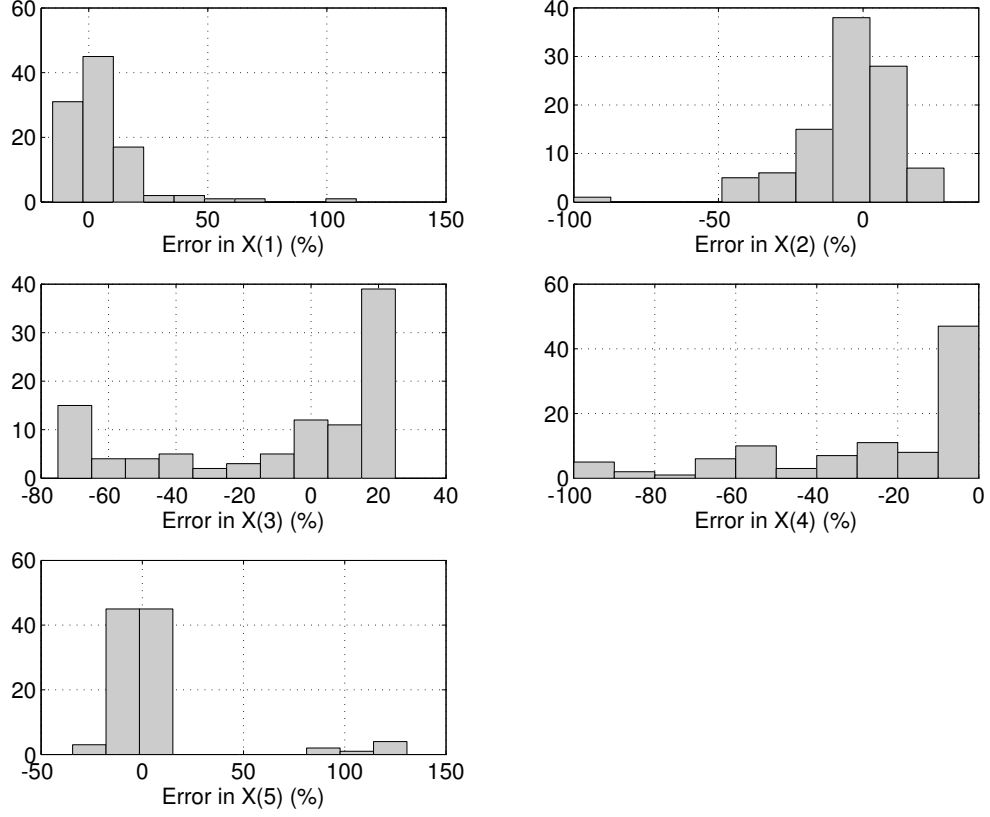
Figure 4.16: Histograms of the error in the retrieved model parameters in presence of 5% Gaussian noise added to the measured data for Case 1 in Section 4.5. Number of simulated realizations: 100.

are independent random variables,

$$\langle v_n^2 \rangle = \langle v^2 \rangle \left(1 + \Delta^2 N^2\right) \tag{4.11}$$

Since the measured voltage is proportional to the measured electric field, (4.11) and (2.65) give

$$\sigma_n^o = \sigma^o \left(1 + \Delta^2 N^2\right) \tag{4.12}$$

where N^2 has Rayleigh distribution. Case 3 is simulated with the new noise model considering 5 different noise strengths, that is, $\Delta = 0.01, 0.02, 0.03, 0.04, 0.05$, or equivalently,
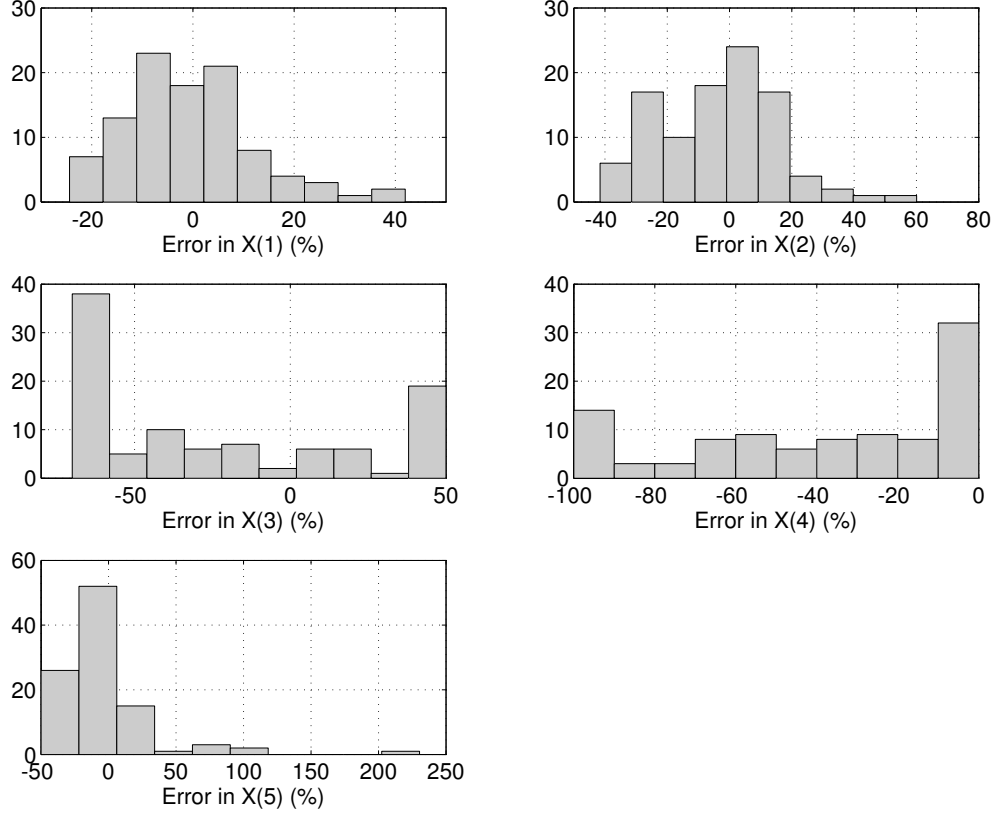
Figure 4.17: Histograms of the error in the retrieved model parameters in presence of 5% Gaussian noise added to the measured data for Case 2 in Section 4.5. Number of simulated realizations: 100.

noting that $\langle N^2 \rangle = 1$, SNR $\sim$ 40, 34, 30, 28, 26 dB. Fig. 4.18 shows the average and standard deviation of the relative output error for the model parameters for the SNR values considered.

Notice that for the practical SNR values considered in this simulation, the output error is always smaller than 25%. The largest errors are observed in ϵ_{1r} and d, and the errors in other model parameters are smaller than 13.7%.

The above results indicate that the estimated values generally show sensitivity to the input noise and we should put effort into reducing the input noise as much as possible. This is not surprising given the extremely nonlinear nature of the scattering model. A strategy to overcome the instability of inversion in presence of large amounts of noise is to average several
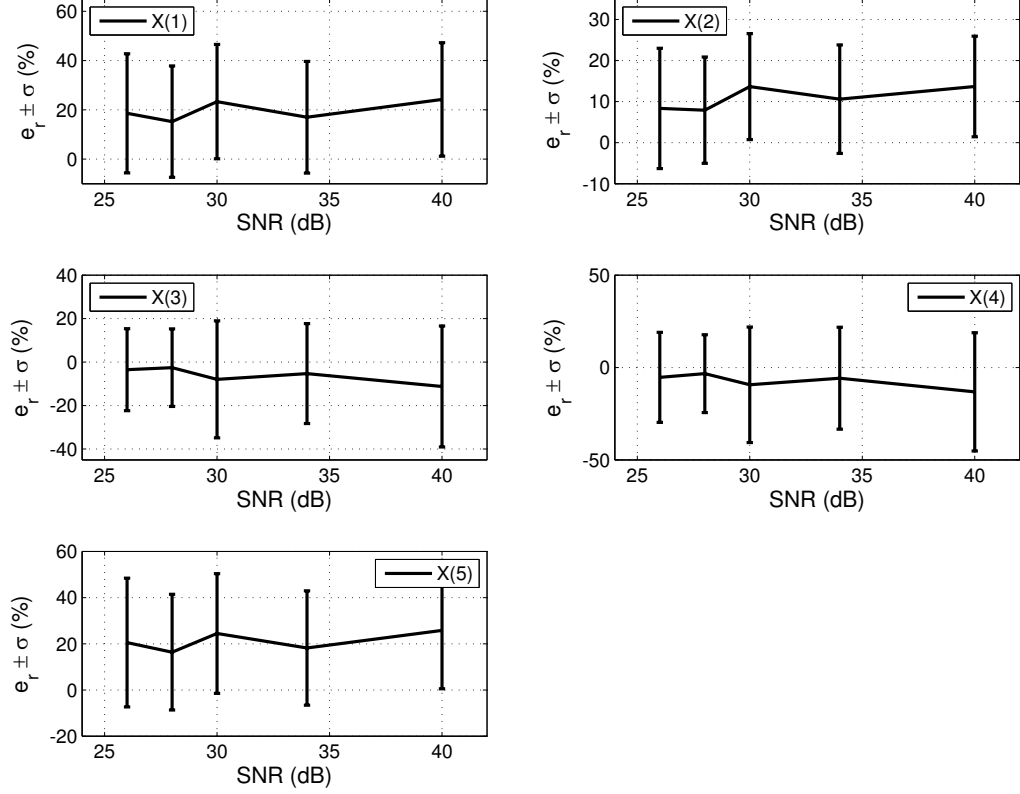
Figure 4.18: Average and standard deviation of the output error at 5 different noise strengths (Δ =0.01, 0.02, 0.03, 0.04, 0.05, or equivalently, SNR $\sim$ 40, 34, 30, 28, 26 dB) for Case 3 (See Table 4.10). Number of realizations is 50.

noise-contaminated data points and feed the averaged data into the inversion algorithm. If we collect N data points at each frequency and incidence angle, the averaging over data samples in (4.8) would be $\mathbf{d}_{avg} = \sum_{i=1}^{N} \mathbf{d}_i / N$. Here, it is assumed that $N = 256$. Table 4.11 shows the output error in the model parameters $\mathbf{X}(1)$–$\mathbf{X}(5)$ for Case 1 and Case 2 after averaging the noise over 256 data points. It is apparent that the output error in all of the model parameters has been improved significantly showing that averaging the input data cancels the additive noise in the measured data.

Table 4.11: Output error in the model parameters after averaging the noise over 256 data points contaminated by 10% Gaussian noise.

	ϵ'_{1r}	σ_1	ϵ'_{2r}	σ_2	d
Case 1	-1.1%	-4.3%	-13.1%	-6.4%	0.2%
Case 2	-0.7%	0.5%	-3.3%	-4.0%	-0.5%

4.6   Summary and Conclusion

This chapter presented the application of the Simulated Annealing method to the inversion of the 9 model parameters characterizing a two-layer dielectric structure with rough boundaries. The forward model calculates the backscattering coefficients of the structure using SPM. It was shown that the Simulated Annealing is a powerful tool capable of retrieving all of the 9 unknown model parameters and minimizing the associated cost function globally. The parameters of most interest are dielectric properties of the layers and the layer thickness. However, it was shown that if we only consider these parameters as unknown and treat the rest as known, error in the *a-priori* values assigned to statistical properties of the interfaces would result in large errors in the retrieved model parameters, and therefore, we need to consider all of the 9 model parameters as unknown.

Values of the inversion parameters were either recommended by Corana *et al.* or derived empirically in order to achieve robust and accurate inversion results. The values of frequency points are forced by the application and measurement system, but the values of observation angles were selected qualitatively in order that the maximum difference between σ^o_{vv} and σ^o_{hh} would result. The other measurement parameters, namely the number of frequency points and the number of measurement angles, were also derived empirically in order to achieve accurate inversion results. These numbers directly impact nonlinearity of the cost function as well as its information content. The values $N_f = 5$ and $N_\theta = 2$ were selected for the cases where all of the 9 model parameters were considered unknown.

To have the algorithm exit a local minimum, the algorithm was enhanced by forcing the temperature to increase when a local minimum is encountered. Based on the Metropolis criterion and the step length adjustment rule of the Corana algorithm, if the temperature is forced to increase, both the step length and the probability of accepting uphill moves

increase, allowing the algorithm to continue its search for the global minimum with a bigger step length, hence in a larger area.

The inversion algorithm shows sensitivity to input noise due to the severe nonlinearity of the problem. However, we should consider the fact that the performance of the inversion algorithm has been tested in presence of extremely large noise amplitudes. Still, depending on the measure considered, all of the model parameters could be considered well retrieved, especially when we assume that measurement noise contaminates measured voltage and when practical values of SNR (20–40 dB) are considered. This is promising for the retrieval of subsurface soil moisture layers. Error in the model parameters can be reduced significantly by averaging the noise over several data points—256 in this work.

While it was shown that the Simulated Annealing is a powerful scheme for inversion of subsurface properties of a layered structure, other algorithms and strategies can also be investigated to speed up the inversion. Use of faster Simulated Annealing schemes such as Very Fast Simulated Reannealing (VFSR) [88] or hybrid optimization schemes [89] are methods yet to be evaluated for inversion of a layered structure properties.

CHAPTER 5

Conclusions and Recommendations for Future Work

5.1 Summary

Layered structures with rough boundaries are representative models for many naturally occurring structures such as layered soil, multiyear ice, and snow-covered lands. Mapping soil moisture, sea ice, and snow is of special interest to scientists due to the critical information content of these maps; knowledge of soil moisture is critical for weather and climate prediction, flood control, and reservoir management. Due to the role of sea ice in the mass balance and heat transfer between the ocean and the atmosphere, a negative change in the sea ice extent would indicate a global warming scenario. Snow mapping is also important for climate reasons as well as for estimating spring runoff amounts for predicting water supply, hydroelectric energy production, and potential flooding. Mapping soil moisture, sea ice, and snow strongly depends on our ability to retrieve the model parameters of the corresponding layered structures. This work addressed the problem of electromagnetic scattering from layered dielectric structures with rough boundaries and the associated inverse problem of retrieving the subsurface parameters of the structure using the scattered field. To this end, a forward scattering model based on the Small Perturbation Method (SPM) was developed to calculate the first-order spectral-domain bistatic scattering coefficients of an N-layer rough surface structure. The region of validity of the forward model was investigated to ensure proper use of the model. Finally, to retrieve the model parameters of the layered structure using the scattered field, an inversion scheme based on the simulated annealing method was

developed and a method was proposed to address a shortcoming of all inversion algorithms, that is, convergence to a local minimum.

5.2 Contributions

The following subsections outline the contributions of this dissertation.

5.2.1 Scattering from Layered Rough Surfaces

The first-order bistatic scattering coefficients of a three-dimensional N-layer dielectric structure with slightly rough interfaces were calculated in the spectral domain using SPM. The layers were considered isotropic and homogenous. The amplitudes of the fields in all regions were obtained simultaneously. The solution is analytical and intrinsically takes into account multiple scattering processes between the boundaries. The method is fast and appropriate for being used in inversion schemes.

5.2.2 Region of Validity of Small Perturbation Method

The region of validity of SPM was investigated. The bistatic scattering coefficients of a two-dimensional two-layer dielectric structure with rough boundaries were calculated using the Method of Moments (MoM). The UV Multilevel Partitioning Method (UV-MLP) was applied to accelerate the MoM solver and it was shown that for a dielectric rough surface scattering, contrary to expectation, UV-MLP does not make the MoM solver faster than a solver such as LU factorization. Five hundred different combinations of the statistical properties of the interfaces and dielectric constants of the layers were simulated. Several observations were reported based on the contour plots of $|\gamma_{\mathrm{MoM}} - \gamma_{\mathrm{SPM}}|$, where γ is the bistatic scattering coefficient.

5.2.3 Inversion of Subsurface Parameters of Two Layer Rough Surfaces

To retrieve the model parameters of a three-dimensional two-layer dielectric structure with rough boundaries, an inversion algorithm based on the simulated annealing was investigated and a method was proposed to address convergence to a local minimum. Some of the inversion parameters were empirically derived to guarantee convergence to correct results. The forward model used in the inversion algorithm to evaluate the cost function as well as to synthesize measured data was the forward model developed in Chapter 2. The algorithm was shown to be capable of retrieving the layers dielectric constants, conductivities, and the mean separation between the layers. All of the model parameters were shown to be well retrieved in presence of noise.

5.3 Future Work

This dissertation addressed a very broad area of research in electromagnetic scattering. The forward modeling of electromagnetic scattering from layered dielectric rough surfaces is a new research area that has much room for advancement. Inverse electromagnetic scattering, which falls into the broader category of inverse problems, though an old area, is still challenging and calls for more research as new forward models are developed and as retrieval of more model parameters with better accuracy and resolution is demanded. The area of inverse electromagnetic scattering is particularly rich with possibilities of being applied to random media. This section outlines a few research areas most relevant to this dissertation.

5.3.1 Forward Model Development

An accurate and fast forward model is necessary to insure a successful inversion process. The first order scattered field in the SPM solution, presented in Chapter 2, is incoherent. While for many applications, the first order solution is considered accurate enough, the coherent scattered field needs to be calculated in order that more sensitive measurements and more accurate inversion become feasible. Extension of the current SPM solution to

higher orders, especially second order, would address this need. The second order solution would also allow calculation of the co-pol phase difference, which has been shown to be very sensitive to subsurface parameters [90].

Naturally occurring structures are represented by different models. For example, the structure in Fig. 2.1 can represent a lake or a simple layered ground while more complex structures would involve inhomogeneous layers, irregular interfaces including very rough as well as undulating interfaces, layers with buried objects, and layers covered by vegetation (Fig. 1.1). Development of analytical and numerical models for scattering from layered rough surfaces that include such media can be very useful in geophysical research, especially mapping soil moisture.

5.3.2   Region of Validity of Small Perturbation Method

It was shown in Chapter 3 that for dielectric rough surfaces, UV-MLP is not faster than a solver such as LU factorization. It was also concluded that for more definitive statements on the limits on the model parameters, especially those affected by multiple scattering processes between the boundaries, more extensive numerical simulations are needed to allow finer sampling of the model space. Possible future work includes developing fast solvers that are more appropriate for scattering from dielectric rough surfaces. These solvers should be fast enough to allow, for example, use of an iterative nonlinear optimizer, which requires fine sampling of the model space as well as measurement parameters such as incidence/scattering angles and polarization.

5.3.3   Inverse Model Development

The Simulated Annealing was shown to be a powerful scheme for inversion of subsurface properties of a layered structure. In addition to investigating the capability of other algorithms and strategies such as genetic algorithms [79] and particle swarm algorithm [80], use of faster Simulated Annealing schemes such as Very Fast Simulated Re-Annealing (VFSR) [88] or hybrid optimization schemes [89] are yet to be studied and developed further for inversion of a layered structure properties.
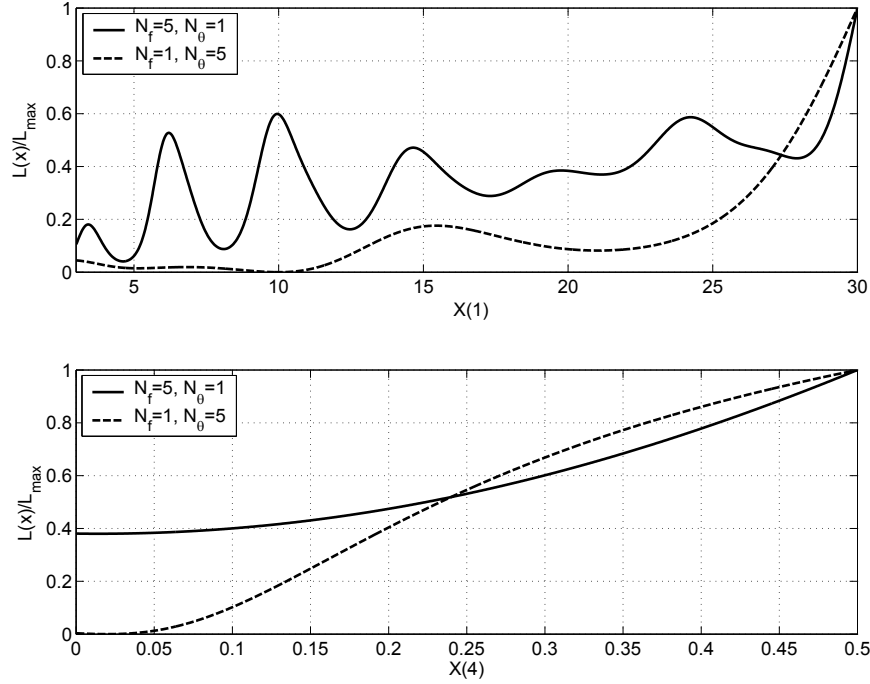
Figure 5.1: A sample cost function used in the inversion algorithm in Chapter 4 plotted versus two of the model parameters for two different sets of measurement parameters. $\mathbf{X}(1)$ represents ϵ'_{1r} and $\mathbf{X}(4)$ represents σ_2.

5.3.4 Design Space for Future Remote Sensing Systems

To successfully and efficiently retrieve the unknowns in the optimization problem associated with the inverse problem in Chapter 4, the number and value of measurement frequencies and observation angles should be chosen judiciously to increase the efficiency and accuracy of the inversion algorithm. These numbers and values affect both the smoothness and information content of the cost function. Fig. 5.1 shows a cost function versus two different model parameters. This figure shows how the nonlinearity of the cost function along different coordinates can vary depending on the number of frequency points and measurement angles. In this dissertation, these quantities were selected empirically based on many inversion cases with different number of unknown model parameters. However, finding the optimum values of these parameters as well as the values of frequency points and measurement angles, with the number of cost function evaluations being a constraint, remains a subject to explore.

APPENDIX

APPENDIX A

A.1 Necessary Expansions

This appendix presents some of the expansions used in the analysis in Chapter 2.
The vectors $\hat{h}(\cdot)$ and $\hat{v}(\cdot)$ are defined as below,

$$\hat{h}(-k_{0z}^i) := \frac{\hat{K}_0^i \times \hat{z}}{|\hat{K}_0^i \times \hat{z}|} \tag{A.1}$$

$$\hat{v}(-k_{0z}^i) := \hat{h}(-k_{0z}^i) \times \hat{K}_0^i \tag{A.2}$$

The minus sign in $\hat{h}(-k_{0z}^i)$ and $\hat{v}(-k_{0z}^i)$ indicates that the incident plane wave is down-going.
Similarly,

$$\hat{h}(k_{nz}) = \frac{\hat{k}_n \times \hat{z}}{|\hat{k}_n \times \hat{z}|} \tag{A.3}$$

$$\hat{v}(k_{nz}) = \hat{h}(k_{nz}) \times \hat{k}_n \tag{A.4}$$

$$\hat{h}(-k_{nz}) = \frac{\hat{K}_n \times \hat{z}}{|\hat{K}_n \times \hat{z}|} \tag{A.5}$$

$$\hat{v}(-k_{nz}) = \hat{h}(-k_{nz}) \times \hat{K}_n \tag{A.6}$$

where $\hat{k}_n = (k_x\hat{x} + k_y\hat{y} + k_{nz}\hat{z})/k_n$, $\hat{K}_n = (k_x\hat{x} + k_y\hat{y} - k_{nz}\hat{z})/k_n$, $k_{nz} = \sqrt{k_n^2 - k_x^2 - k_y^2}$, $k_n = \omega\sqrt{\mu_0\epsilon_n}$, and $n = 0, 1, 2$. It is worth mentioning that k_{nz} is considered a positive quantity throughout the analysis.

According to (A.3)–(A.6),

$$\hat{h}(\pm k_{nz}) = \frac{-k_x \hat{y} + k_y \hat{x}}{k_\rho} \tag{A.7}$$

and

$$\hat{v}(\pm k_{nz}) = \mp \frac{k_{nz}}{k_n k_\rho}(k_x \hat{x} + k_y \hat{y}) + \frac{k_\rho}{k_n}\hat{z} \tag{A.8}$$

where $k_\rho = \sqrt{k_x^2 + k_y^2}$. Also, the unit vectors normal to the boundaries are

$$\hat{n}_1(\mathbf{r}_\perp) = \frac{-\xi f_{1x}\hat{x} - \xi f_{1y}\hat{y} + \hat{z}}{\sqrt{\xi^2 f_{1x}^2 + \xi^2 f_{1y}^2 + 1}} \tag{A.9}$$

and

$$\hat{n}_2(\mathbf{r}_\perp) = \frac{-\xi f_{2x}\hat{x} - \xi f_{2y}\hat{y} + \hat{z}}{\sqrt{\xi^2 f_{2x}^2 + \xi^2 f_{2y}^2 + 1}} \tag{A.10}$$

where subscripts 'x' and 'y' indicate the partial derivative with respect to x and y, respectively. Therefore, the expressions for $\hat{n}_{1,2} \times \hat{h}(\cdot)$ and $\hat{n}_{1,2} \times \hat{v}(\cdot)$ are as follows.

$$\hat{n}_{1,2} \times \hat{h}(\pm k_{nz}) = \frac{k_x \hat{x} + k_y \hat{y} + (\xi f_{1,2x}k_x + \xi f_{1,2y}k_y)\hat{z}}{k_\rho \sqrt{\xi^2 f_{1,2x}^2 + \xi^2 f_{1,2y}^2 + 1}} \tag{A.11}$$

$$\hat{n}_{1,2} \times \hat{v}(\pm k_{nz}) = \frac{(\pm k_{nz}k_y - \xi f_{1,2y}k_\rho^2)\hat{x} + (\mp k_{nz}k_x + \xi f_{1,2x}k_\rho^2)\hat{y} + (\pm \xi f_{1,2x}k_{nz}k_y \mp \xi f_{1,2y}k_{nz}k_x)\hat{z}}{k_n k_\rho \sqrt{\xi^2 f_{1,2x}^2 + \xi^2 f_{1,2y}^2 + 1}} \tag{A.12}$$

When the boundary conditions are applied, the exponential terms in the integrands should be expanded in terms of ξ using Taylor series representation.

$$e^{+ik_{0z}\xi f_1(x,y)} = \sum_{n=0}^{\infty} \frac{(+ik_{0z}f_1(x,y))^n \xi^n}{n!} \tag{A.13}$$

Other exponential terms are expanded similarly. Additionally, note that

$$\sum_{m=0}^{\infty} \frac{a_{h,v}^{+(m)}\xi^m}{m!} \times \sum_{n=0}^{\infty} \frac{(+ik_{0z}f_1(x,y))^n \xi^n}{n!} = \sum_{m=0}^{\infty} \sum_{n=0}^{m} \frac{a_{h,v}^{+(n)}(+ik_{0z}f_1(x,y))^{m-n}\xi^m}{n!(m-n)!} \tag{A.14}$$

Similar relations hold for the terms that include $b_{h,v}^{\pm(m)}$ and $c_{h,v}^{-(m)}$.

A.2   Analytical Validation of the Zeroth- and First-Order Solutions for the Two-Layer Case

A.2.1   Zeroth-Order Solution

Solving for the zeroth-order coefficients results in

$$a_h^{+(0)}(\mathbf{k}_\perp) = \frac{(k_{1z} + k_{2z})(k_{1z} - k_{0z}) - e^{i2k_{1z}d_1}(k_{1z} - k_{2z})(k_{1z} + k_{0z})}{e^{i2k_{1z}d_1}(k_{1z} - k_{2z})(k_{1z} - k_{0z}) - (k_{1z} + k_{2z})(k_{1z} + k_{0z})} E_o^h \delta(\mathbf{k}_\perp - \mathbf{k}_\perp^i) \quad \text{(A.15)}$$

The reflection coefficient of a two-layer dielectric structure for horizontal (perpendicular or TE) polarization is known to be [51]

$$R^h = \frac{R_{01}^h + R_{12}^h e^{i2k_{1z}d_1}}{1 + R_{01}^h R_{12}^h e^{i2k_{1z}d_1}} \quad \text{(A.16)}$$

where R_{01}^h and R_{12}^h are the Fresnel reflection coefficients for horizontal polarization and are given by

$$R_{01}^h = \frac{k_{0z} - k_{1z}}{k_{0z} + k_{1z}} \quad \text{(A.17)}$$

and

$$R_{12}^h = \frac{k_{1z} - k_{2z}}{k_{1z} + k_{2z}} \quad \text{(A.18)}$$

Substituting (A.17) and (A.18) into (A.16) will result in

$$R^h = \frac{(k_{1z} + k_{2z})(k_{1z} - k_{0z}) - e^{i2k_{1z}d_1}(k_{1z} - k_{2z})(k_{1z} + k_{0z})}{e^{i2k_{1z}d_1}(k_{1z} - k_{2z})(k_{1z} - k_{0z}) - (k_{1z} + k_{2z})(k_{1z} + k_{0z})} \quad \text{(A.19)}$$

The solution for vertical polarization as well as the solution to the three-layer case can be validated similarly.

A.2.2   First-Order Solution

In the special case of $\epsilon_1 = \epsilon_2$ and with the assumption $E_o^v = 0$, Mathematica gives

$$a_h^{+(1)}(\mathbf{k}_\perp) = \frac{ik_\rho F_1(\mathbf{k}_\perp - \mathbf{k}_\perp^{\mathbf{i}})}{k_\rho^i(k_x^2 + k_y^2)(k_{1z} + k_{0z})} \times$$

$$\left[a_h^{+(0)}(\mathbf{k}_\perp^i) \left((k_\rho^i)^2 \left(k_x^2 - k_x k_x^i + k_y^2 - k_y k_y^i\right) - \left(k_x k_x^i + k_y k_y^i\right) k_{0z}^i \left(k_{1z} + k_{0z}^i\right) \right) - \right.$$

$$b_h^{-(0)}(\mathbf{k}_\perp^i) \left((k_\rho^i)^2 (k_x^2 - k_x k_x^i + k_y^2 - k_y k_y^i) + (k_x k_x^i + k_y k_y^i)k_{1z}^i(k_{1z} - k_{1z}^i) \right) +$$

$$\left. E_o^h \left((k_\rho^i)^2 \left(k_x^2 - k_x k_x^i + k_y^2 - k_y k_y^i\right) + \left(k_x k_x^i + k_y k_y^i\right) k_{0z}^i \left(k_{1z} - k_{0z}^i\right) \right) \right] \quad \text{(A.20)}$$

Since $k_x^s = k_0 \sin\theta_s \cos\phi_s$, $k_y^s = k_0 \sin\theta_s \sin\phi_s$, $k_x^i = k_0 \sin\theta_i \cos\phi_i$, $k_y^i = k_0 \sin\theta_i \sin\phi_i$, $k_\rho^s = k_0 \sin\theta_s$, and $k_\rho^i = k_0 \sin\theta_i$, after inserting the zeroth-order solution into (A.20), the following will result:

$$a_h^{+(1)}(\mathbf{k}_\perp^s) = \frac{i2E_o^h F_1(\mathbf{k}_\perp^s - \mathbf{k}_\perp^i)(k_{1z}^i - k_{0z}^i)k_{0z}^i \cos(\phi_i - \phi_s)}{k_{1z}^s + k_{0z}^s} \quad \text{(A.21)}$$

Multiplying both the numerator and denominator by $(k_{1z}^i + k_{0z}^i)$, and inserting the result into (2.64) and (2.65) will give

$$\sigma_{hh}^o(\hat{k}_s, \hat{k}_i) = 16\pi k_0^4 \cos^2\theta_s \cos^2\theta_i \left| \frac{(k_1^2 - k_0^2)}{(k_{0z}^s + k_{1z}^s)(k_{0z}^i + k_{1z}^i)} \right|^2 \cos^2(\phi_s - \phi_i) W_{f_1}(\mathbf{k}_\perp^s - \mathbf{k}_\perp^i) \quad \text{(A.22)}$$

which shows a perfect match with the literature [37]. Similar calculations can be done for other coefficients.

Another special case is when $F_1(\mathbf{k}_\perp - \mathbf{k}_\perp^i) = 0$, which means a rough interface covered by a flat dielectric layer, in which case Mathematica gives

$$a_h^{+(1)}(\mathbf{k}_\perp) = \frac{-i2k_{1z}k_\rho e^{id_1(k_{1z} - k_{1z}^i)} F_2(\mathbf{k}_\perp - \mathbf{k}_\perp^i)}{k_\rho^i(k_x^2 + k_y^2)\left(e^{i2d_1 k_{1z}}(k_{1z} - k_{2z})(k_{1z} - k_{0z}) - (k_{1z} + k_{2z})(k_{1z} + k_{0z})\right)} \times$$

$$\left[b_h^{-(0)}(\mathbf{k}_\perp^i)e^{i2d_1 k_{1z}^i} \left((k_\rho^i)^2(k_x^2 - k_x k_x^i + k_y^2 - k_y k_y^i) - k_{1z}^i(k_{1z}^i - k_{2z})(k_x k_x^i + k_y k_y^i) \right) + \right.$$

$$b_h^{+(0)}(\mathbf{k}_\perp^i) \left((k_\rho^i)^2(k_x^2 - k_x k_x^i + k_y^2 - k_y k_y^i) - k_{1z}^i(k_{1z}^i + k_{2z})(k_x k_x^i + k_y k_y^i) \right) -$$

$$\left. c_h^{-(0)}(\mathbf{k}_\perp^i)e^{id_1(k_{1z}^i + k_{2z}^i)} \left((k_\rho^i)^2(k_x^2 - k_x k_x^i + k_y^2 - k_y k_y^i) + k_{2z}^i(k_{2z} - k_{2z}^i)(k_x k_x^i + k_y k_y^i) \right) \right] \quad \text{(A.23)}$$

With similar substitutions, $a_h^{+(1)}(\mathbf{k}_\perp^s)$ can be shown to be

$$a_h^{+(1)}(\mathbf{k}_\perp^s) = -8e^{id_1(k_{1z}^s + k_{1z}^i)} k_{1z}^s k_{1z}^i (k_1^2 - k_2^2) k_{0z}^i \cos(\phi_s - \phi_i) \times$$
$$\frac{1}{e^{id_1 k_{1z}^s}(k_{1z}^s - k_{0z}^s)(k_{1z}^s - k_{2z}^s) - (k_{1z}^s + k_{0z}^s)(k_{1z}^s + k_{2z}^s)} \times$$
$$\frac{1}{e^{id_1 k_{1z}^i}(k_{1z}^i - k_{0z}^i)(k_{1z}^i - k_{2z}^i) - (k_{1z}^i + k_{0z}^i)(k_{1z}^i + k_{2z}^i)} \quad \text{(A.24)}$$

Inserting (A.24) into (2.65) gives

$$\sigma_{hh}^o = 256\pi k_0^4 \cos^2\theta_i \cos^2\theta_s |k_1^2 - k_2^2|^2 \cos^2(\phi_s - \phi_i)$$
$$\times \left| \frac{k_{1z}^i}{e^{i2d_1 k_{1z}^i}(k_{1z}^i - k_{0z}^i)(k_{1z}^i - k_{2z}^i) - (k_{1z}^i + k_{0z}^i)(k_{1z}^i + k_{2z}^i)} \right|^2$$
$$\times \left| \frac{k_{1z}^s}{e^{i2d_1 k_{1z}^s}(k_{1z}^s - k_{0z}^s)(k_{1z}^s - k_{2z}^s) - (k_{1z}^s + k_{0z}^s)(k_{1z}^s + k_{2z}^s)} \right|^2 W_{f_2}(\mathbf{k}_\perp^s - \mathbf{k}_\perp^i) \quad \text{(A.25)}$$

which is similar to the results in [46]. Similar calculations can be done for other coefficients. It is worth reminding that in the zeroth-order coefficients appearing in (A.20) and (A.23), $\delta(\mathbf{k}_\perp - \mathbf{k}_\perp^\mathbf{i})$ is suppressed. The solution to the three-layer case can be validated similarly.

A.3   Note on Power Spectral Density

Power spectral density of a 2D rough surface profile has the following definition:

$$W_{f_1}(\mathbf{k}_\perp) := \frac{\sigma_{f_1}^2}{(2\pi)^2} \int\limits_{-\infty}^{\infty}\int\limits_{-\infty}^{\infty} \mathrm{d}\mathbf{r}_\perp \, C_{f_1}(\mathbf{r}_\perp) e^{-i\mathbf{k}_\perp \cdot \mathbf{r}_\perp} \tag{A.26}$$

It also satisfies the relation

$$W_{f_1}(\mathbf{k}_\perp) = (2\pi)^2 \lim_{A\to\infty} \frac{\langle |F_1(\mathbf{k}_\perp)|^2 \rangle}{A} \tag{A.27}$$

where $C_{f_1}(\mathbf{r}_\perp)$, the correlation coefficient between two points on the surface $f_1(x,y)$, is defined as $\langle f_1(\mathbf{r}_{\perp 1}) f_1(\mathbf{r}_{\perp 2}) \rangle / \sigma_{f_1}^2$ and in general is a function of $\mathbf{r}_{\perp 2}$ and $\mathbf{r}_{\perp 1}$. Since the surface is assumed to be statistically homogeneous isotropic, C_{f_1} is a function of $|\mathbf{r}_\perp| = |\mathbf{r}_{\perp 2} - \mathbf{r}_{\perp 1}|$. The quantity σ_{f_1} is the standard deviation of $f_1(x,y)$. Likewise, we may define $C_{f_1 f_2}$ as $\langle f_1(\mathbf{r}_{\perp 1}) f_2(\mathbf{r}_{\perp 2}) \rangle / \sigma_{f_1} \sigma_{f_2}$ and define $W_{f_1 f_2}$ accordingly. Assuming that $C_{f_1 f_2}$ is a function of $|\mathbf{r}_\perp| = |\mathbf{r}_{\perp 2} - \mathbf{r}_{\perp 1}|$, $W_{f_1 f_2}$ will be real and will satisfy the following relation:

$$W_{f_1 f_2}(\mathbf{k}_\perp) = (2\pi)^2 \lim_{A\to\infty} \frac{\langle F_1(\mathbf{k}_\perp) F_2^*(\mathbf{k}_\perp) \rangle}{A} \tag{A.28}$$

APPENDIX B

B.1 Random Rough Surface Generation

This section describes how realizations of Gaussian random rough surfaces can be generated [64].

If z_1 and z_2 are two random variables, their correlation coefficient is defined as

$$C = \frac{\langle (z_1 - \eta_1)(z_2 - \eta_2) \rangle}{\sigma_1 \sigma_2} \tag{B.1}$$

where η_i and σ_i are the mean value and standard deviation of z_i, respectively. Similarly, the correlation function of a random process $f(x)$ is defined as

$$C(x_1, x_2) = \frac{\langle (f(x_1) - \eta_1)(f(x_2) - \eta_2) \rangle}{\sigma_1 \sigma_2} \tag{B.2}$$

Let's assume that the rough surface is represented by a random process that is stationary to order two. Therefore, $\eta_1 = \eta_2$, $\sigma_1 = \sigma_2$, and $C(x_1, x_2) = C(x_1 - x_2)$. If we assume that $\eta_1 = \eta_2 = 0$ and $\sigma_1 = \sigma_2 = \sigma$,

$$C(x_1 - x_2) = \frac{\langle f(x_1)f(x_2) \rangle}{\sigma^2} \tag{B.3}$$

Let's also assume that the process $f(x)$ is normal, that is, the random variables $f(x_1)$, $f(x_2)$, ..., $f(x_n)$ are jointly normal for every n and x_1, x_2, ..., x_n. Therefore, the statistics of $f(x)$ are completely determined by η and $C(x_1 - x_2)$. The Fourier transform of $\sigma^2 C(x)$ is the

spectral density

$$W(k_x) := \sigma^2 \mathscr{F}\{C(x)\} = \frac{\sigma^2}{2\pi} \int_{-\infty}^{+\infty} C(x) \exp\left(-ik_x x\right) dx \tag{B.4}$$

A surface of finite length L is to be generated. The function $f(x)$ is made periodic outside L, i.e., $f(x) = f(x+L)$ and use a Fourier series to represent $f(x)$.

$$f(x) = \frac{1}{L} \sum_{n=-\infty}^{\infty} b_n \exp\left(\frac{i2\pi nx}{L}\right) \tag{B.5}$$

where b_n is a Gaussian random variable. From (B.5), we have

$$\langle f(x_1) f(x_2) \rangle = \frac{1}{L^2} \sum_{n=-\infty}^{\infty} \sum_{m=-\infty}^{\infty} \langle b_n b_m^* \rangle \exp\left(\frac{i2\pi nx_1}{L}\right) \exp\left(\frac{-i2\pi mx_2}{L}\right) \tag{B.6}$$

From (B.3), (B.4), and (B.6), we can write

$$\langle b_n b_m^* \rangle = \delta_{nm} B_n \tag{B.7}$$

and

$$\int_{-\infty}^{\infty} dk_x \exp\left(ik_x(x_1 - x_2)\right) W(k_x) = \frac{1}{L^2} \sum_{n=-\infty}^{\infty} B_n \exp\left(i\frac{2\pi n}{L}(x_1 - x_2)\right) \tag{B.8}$$

where δ_{nm} is the Kronecker delta function. If $\Delta k_x = \frac{2\pi}{L}$ and $K_n = \frac{2\pi n}{L} = n\Delta k_x$, discretizing the integral in (B.8) results in

$$\frac{2\pi}{L} \sum_{n=-\infty}^{\infty} \exp\left(iK_n(x_1 - x_2)\right) W(K_n) = \frac{1}{L^2} \sum_{n=-\infty}^{\infty} B_n \exp\left(iK_n(x_1 - x_2)\right) \tag{B.9}$$

which results in

$$B_n = 2\pi L W(K_n) \tag{B.10}$$

From (B.7) and (B.10),

$$\langle |b_n|^2 \rangle = 2\pi L W(K_n) \tag{B.11}$$

From the properties of the Fourier series (B.5), we have $b_n = b_{-n}^*$. If we let $m = -n$ in (B.7),

we get $\langle b_n b_{-n}^* \rangle = 0$. Therefore,

$$\langle b_n b_n \rangle = 0 \tag{B.12}$$

which, letting $b_n = \Re\{b_n\} + i\Im\{b_n\}$, gives

$$\langle (\Re\{b_n\})^2 \rangle = \langle (\Im\{b_n\})^2 \rangle \tag{B.13}$$

and

$$\langle \Re\{b_n\} \Im\{b_n\} \rangle = 0 \tag{B.14}$$

From (B.5), $\langle b_n \rangle = 0$, so $\langle \Re\{b_n\} \rangle = 0$ and $\langle \Im\{b_n\} \rangle = 0$. Therefore,

$$\langle \Re\{b_n\} \Im\{b_n\} \rangle = \langle \Re\{b_n\} \rangle \langle \Im\{b_n\} \rangle \tag{B.15}$$

meaning that $\Re\{b_n\}$ and $\Im\{b_n\}$ are independent Gaussian random variables with a variance equal to half of the variance of $|b_n|$. This can easily be seen from $\Re\{b_n\} = (b_n + b_n^*)/2$, $\Im\{b_n\} = (b_n - b_n^*)/2$, and (B.12).

Since the surface is generated with a limited number of points, the DFT version of (B.5) is used. Let there be N points in both spatial and spectral domains, that is, $\Delta x = \frac{L}{N}$ and $x_m = m\Delta x$ for $m = -\frac{N}{2} + 1, \ldots, 0, 1, \ldots, \frac{N}{2}$. Then

$$f_m = \frac{1}{L} \sum_{n=-\frac{N}{2}+1}^{\frac{N}{2}} b_n \exp\left(i\frac{2\pi nm}{N}\right) \tag{B.16}$$

The inverse DFT is

$$b_n = \frac{L}{N} \sum_{m=-\frac{N}{2}+1}^{\frac{N}{2}} f_m \exp\left(-i\frac{2\pi nm}{N}\right) \tag{B.17}$$

Both f_m and b_n are periodic sequences with period N. That is, $b_{n+N} = b_n$ and $f_{m+N} = f_m$. Therefore,

$$b_{-\frac{N}{2}} = b_{\frac{N}{2}} \tag{B.18}$$

Therefore, $b_{\frac{N}{2}}$ is real, because $b_n = b_{-n}^*$, which also implies b_0 is real.

To summarize, b_0 and $b_{\frac{N}{2}}$ are two Gaussian numbers. The quantities $b_{-\frac{N}{2}+1}$, $b_{-\frac{N}{2}+2}$,

... , b_{-2}, b_{-1} are complex numbers with real and imaginary parts that are Gaussian. The quantities b_1, b_2, ... , $b_{\frac{N}{2}-1}$ can be calculated using the fact that $b_n = b^*_{-n}$. The algorithm to generate the Gaussian random rough surface is as follows.

- Generate N independent Gaussian random numbers with zero mean and unit variance. Denote these numbers by r_1, r_2, ... , r_N.

- Calculate

$$b_0 = \sqrt{2\pi L W(0)} r_\alpha \tag{B.19}$$

$$b_{\frac{N}{2}} = \sqrt{2\pi L W(\frac{\pi N}{L})} r_\beta \tag{B.20}$$

  where r_α and r_β are two of the N Gaussian random numbers generated.

- Calculate

$$b_n = \sqrt{2\pi L W(|K_n|)} \left\{ \frac{1}{\sqrt{2}} (r_\sigma + i r_\xi) \right\} \tag{B.21}$$

  for $n = -\frac{N}{2} + 1$, ... , -2, -1 where r_σ and r_ξ are two of the N Gaussian numbers generated.

- Calculate

$$b_n = b^*_{-n} \tag{B.22}$$

  for $n = 1, 2, 3, \ldots, \frac{N}{2} - 1$

- The rough surface profile is calculated from (B.16).

B.1.1 Numerical Example

If we assume the correlation function is Gaussian, i.e., if

$$C(x) = \exp\left(-\frac{x^2}{l^2}\right) \tag{B.23}$$

where l is the random process correlation length, the spectral density will be

$$W(k_x) = \frac{\sigma^2 l}{2\sqrt{\pi}} \exp\left(-\frac{k_x^2 l^2}{4}\right) \tag{B.24}$$

Fig. B.1 shows two Gaussian rough surface profiles generated with the above algorithm. The top surface has been generated with 1000 points and the bottom surface has been constructed using 800 points. The top rough surface has a correlation length of 20 cm and the bottom rough surface correlation length is 50 cm. Both surfaces have a standard deviation of 1 cm. Both of the rough surfaces are assumed to have Gaussian correlation functions. The mean separation between the rough surfaces is 30 cm.
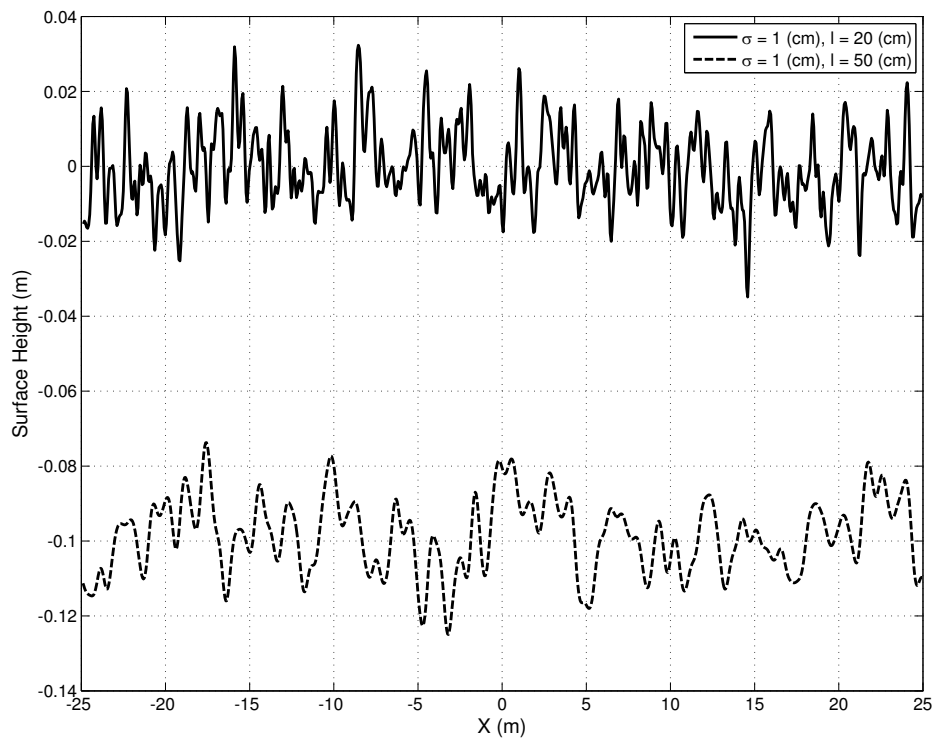

Figure B.1: Two Gaussian random rough surfaces generated using the algorithm in Appendix B.1.

B.2 Electric and Magnetic Potential Functions

Assuming the boundaries in Fig. 3.1 are parameterized in t, the potential functions in (3.27)–(3.30) are

$$\mathbf{A}_0(t) = \frac{i}{4} \int_{S_1} \mathbf{J}_1(t') H_0^{(1)}(k_0 R) dt' \tag{B.25}$$

$$\mathbf{A}_1(t) = \frac{i}{4} \int_{S_2} \mathbf{J}_2(t') H_0^{(1)}(k_1 R) dt' - \frac{i}{4} \int_{S_1} \mathbf{J}_1(t') H_0^{(1)}(k_1 R) dt' \tag{B.26}$$

$$\mathbf{A}_2(t) = -\frac{i}{4} \int_{S_2} \mathbf{J}_2(t') H_0^{(1)}(k_2 R) dt' \tag{B.27}$$

$$\mathbf{F}_0(t) = \frac{i}{4} \int_{S_1} \mathbf{K}_1(t') H_0^{(1)}(k_0 R) dt' \tag{B.28}$$

$$\mathbf{F}_1(t) = \frac{i}{4} \int_{S_2} \mathbf{K}_2(t') H_0^{(1)}(k_1 R) dt' - \frac{i}{4} \int_{S_1} \mathbf{K}_1(t') H_0^{(1)}(k_1 R) dt' \tag{B.29}$$

$$\mathbf{F}_2(t) = -\frac{i}{4} \int_{S_2} \mathbf{K}_2(t') H_0^{(1)}(k_2 R) dt' \tag{B.30}$$

$$\Phi_{m0} = \frac{i}{4} \int_{S_1} \frac{\rho_{m1}(t')}{\mu_0} H_0^{(1)}(k_0 R) dt' \tag{B.31}$$

$$\Phi_{m1} = \frac{i}{4} \int_{S_2} \frac{\rho_{m2}(t')}{\mu_0} H_0^{(1)}(k_1 R) dt' - \frac{i}{4} \int_{S_1} \frac{\rho_{m1}(t')}{\mu_0} H_0^{(1)}(k_1 R) dt' \tag{B.32}$$

$$\Phi_{m2} = -\frac{i}{4} \int_{S_2} \frac{\rho_{m2}(t')}{\mu_0} H_0^{(1)}(k_2 R) dt' \tag{B.33}$$

and $R = \sqrt{(x(t) - x(t'))^2 + (y(t) - y(t'))^2}$.

B.3 Derivation of the Bistatic Scattering Coefficient of a 1D Rough Surface

This appendix describes how (3.71) is derived. Assume the total field in the incidence region is $\psi(\boldsymbol{\rho})$, which represents E^z for TM incidence and H^z for TE incidence. According to Huygen's principle, the scattered field is

$$\psi_s(\boldsymbol{\rho}') = -\int_{S_1} ds \left[\psi(\boldsymbol{\rho})\hat{n} \cdot \nabla g(\boldsymbol{\rho}, \boldsymbol{\rho}') - g(\boldsymbol{\rho}, \boldsymbol{\rho}')\hat{n} \cdot \nabla \psi(\boldsymbol{\rho}) \right] \tag{B.34}$$

Given $\psi(\boldsymbol{\rho})$ and $\hat{n} \cdot \nabla \psi(\boldsymbol{\rho})$ on the surface, the scattered wave $\psi_s(\boldsymbol{\rho})$ can be calculated by calculating the above integral.

Assuming the observation point $\boldsymbol{\rho}'$ is in the far-field region,

$$g(\boldsymbol{\rho}, \boldsymbol{\rho}') = \frac{i}{4}\sqrt{\frac{2}{\pi k_o \rho'}} e^{-i\frac{\pi}{4}} e^{ik_o \rho'} e^{-ik_o(x\cos\phi_s + y\sin\phi_s)} \tag{B.35}$$

Therefore,

$$\hat{n} \cdot \nabla g(\boldsymbol{\rho}, \boldsymbol{\rho}')\big|_{y=f(x)} \sqrt{1 + \left(\frac{df}{dx}\right)^2} = \frac{i}{4}\sqrt{\frac{2}{\pi k_o \rho'}} e^{-i\frac{\pi}{4}} e^{ik_o \rho'}$$
$$\times \left[\frac{df(x)}{dx}(ik_o \cos\phi_s) - ik_o \sin\phi_s \right] e^{-ik_o(x\cos\phi_s + f(x)\sin\phi_s)} \tag{B.36}$$

From (B.34), (B.35), and (B.36), we have

$$\psi_s(\boldsymbol{\rho}') = \frac{i}{4}\sqrt{\frac{2}{\pi k_o \rho'}} e^{-i\frac{\pi}{4}} e^{ik_o \rho'} \psi_s^{(N)}(\phi_s) \tag{B.37}$$

where

$$\psi_s^{(N)}(\phi_s) = -\int_{-\infty}^{\infty} dx \left(-U(x) + ik_o \psi(x) \left[\frac{df}{dx}\cos\phi_s - \sin\phi_s \right] \right)$$
$$\times e^{-ik_o(x\cos\phi_s + f(x)\sin\phi_s)} \tag{B.38}$$

where $U(x) = \hat{n} \cdot \nabla\psi|_{y=f(x)} \sqrt{1 + \left(\frac{df}{dx}\right)^2}$. Noting that

$$dx = \frac{ds}{\sqrt{1 + \left(\frac{df}{dx}\right)^2}} \tag{B.39}$$

we can rewrite (B.38) as

$$\psi_s^{(N)}(\phi_s) = -\int_{S_1} ds \left(-\hat{n} \cdot \nabla\psi(x) + ik_0\psi(x) \frac{\frac{df}{dx}\cos\phi_s - \sin\phi_s}{\sqrt{1 + \left(\frac{df}{dx}\right)^2}} \right)$$
$$\times e^{-ik_0\,(x\cos\phi_s + f(x)\sin\phi_s)} \tag{B.40}$$

Assuming a TM incidence, that is, $\mathbf{E}_{inc} = \hat{z}\psi_{inc}$ and the total field in the incidence region is $\mathbf{E}_0 = \hat{z}\psi = \hat{z}(\psi_{inc} + \psi_s)$, we can write

$$\nabla \times \hat{z}\psi = ik_0\eta_0\mathbf{H}_0 \tag{B.41}$$

Since $\nabla \times \hat{z}\psi = \nabla\psi \times \hat{z}$, we have $\mathbf{H}_0 = \nabla\psi \times \hat{z}/ik_0\eta_0$. Applying the boundary condition $\hat{n} \times \mathbf{H}_0 = \mathbf{J}_1$ on S_1 gives

$$\hat{n} \times \mathbf{H_0} = \frac{\hat{n} \times (\nabla\psi \times \hat{z})}{ik_0\eta_0} = -\frac{\hat{n} \cdot \nabla\psi\hat{z}}{ik_0\eta_0} = J_{1z}\hat{z} \tag{B.42}$$

So

$$\hat{n} \cdot \nabla\psi(x) = -ik_0\eta_0 J_{1z}(x) \tag{B.43}$$

The boundary condition $\hat{n} \times \hat{z}\psi = -\mathbf{K}_1$ implies

$$\psi(x) = K_{1t} \tag{B.44}$$

because $\hat{n} \times \hat{z} = -\hat{t}$ according to the convention shown in Fig. 3.3. Equations (B.40), (B.43),

(B.44) result in

$$\psi_s^{(N)}(\phi_s) = -\int_{S_1} ds \left(ik_0 \eta_0 J_{1z} + ik_0 K_{1t} \frac{f'(x)\cos\phi_s - \sin\phi_s}{\sqrt{1 + f'(x)^2}} \right)$$
$$\times \exp\left[-ik_0\left(x\cos\phi_s + f(x)\sin\phi_s\right)\right] \qquad (B.45)$$

Similarly, for TE incidence,

$$\psi_s^{(N)}(\phi_s) = -\int_{S_1} ds \left(ik_0 \eta_0 M_{1z} - ik_0 J_{1t} \frac{f'(x)\cos\phi_s - \sin\phi_s}{\sqrt{1 + f'(x)^2}} \right)$$
$$\times \exp\left[-ik_0\left(x\cos\phi_s + f(x)\sin\phi_s\right)\right] \qquad (B.46)$$

B.4 Index-Dependent Probability Density Functions

For sampling rows and columns of a block, one might want to use a density function that depends on the row and column indices. Consider $\mathbf{Z}_{ek_1}^{s_2}$ in (3.106) and assume it has been decomposed to 25 blocks of the same size. See Fig. B.2(a). Although this decomposition is not consistent with multilevel partitioning, it helps understand the distribution used for row and column samples. Since the location of the block is below the diagonal, for a fixed column, i.e., cell current, as the index of the observation cell increases, the contribution of the cell current to the boundary field decreases. See Fig. B.2(b). Therefore, the probability of choosing rows with larger row indices should be smaller for this block. On the other hand, since for a fixed row, as the column index increases, the distance between the cell current and an observation point on the second boundary decreases, the probability of choosing columns with larger indices should be larger. Similar discussion holds for blocks above the diagonal, except that for such blocks, the probability of choosing rows/columns with larger indices, should be larger/smaller. We may, therefore, use the following probabilities for sampling rows and columns of a block within a submatrix. If i and j denote the row and column indices, respectively, and if i_b and j_b respectively denote the relative indices of a block within a submatrix,

$$Pr\{i\} = \begin{cases} \dfrac{i^{-1}}{\displaystyle\sum_{l=1}^{M} l^{-1}} & \text{if } i_b > j_b \\[2em] \dfrac{i}{\displaystyle\sum_{l=1}^{M} l} & \text{if } i_b < j_b \end{cases} \tag{B.47}$$

$$Pr\{j\} = \begin{cases} \dfrac{j}{\displaystyle\sum_{l=1}^{M} l} & \text{if } i_b > j_b \\[2em] \dfrac{j^{-1}}{\displaystyle\sum_{l=1}^{M} l^{-1}} & \text{if } i_b < j_b \end{cases} \tag{B.48}$$

This appendix describes how such distributions can be generated from a uniform distribution. Assuming the probability density function of a random variable X is $f_X(x)$, the
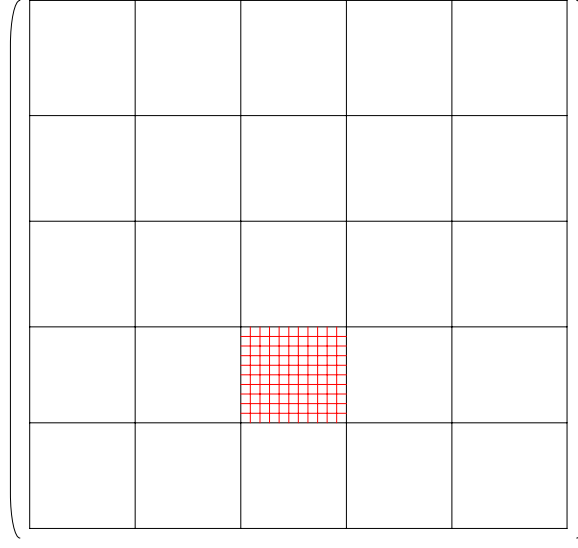
(a)
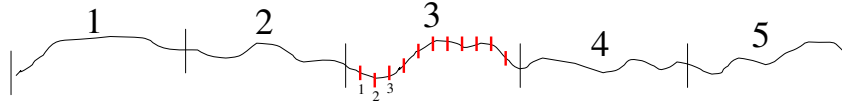
(b)

Figure B.2: (a) A block within a submatrix of the impedance matrix. The red block represents the interaction between the red current elements on the first boundary and the boundary field at the red cells on the second interface. (b) Red cells on the first boundary correspond to the columns of the red block and red cells on the second boundary correspond to the rows of the red block.

probability density function of the random variable $Y = g(X)$ is

$$f_Y(y) = \frac{f_X(x_1)}{g'(x_1)} \tag{B.49}$$

where x_1 is the solution to the equation $y = g(x)$. The goal is generating an integer, representing a row or column index, with a probability that is either directly or inversely proportional to the integer. Equivalently, if the integer is the integral part of $y = g(x)$, we look for a function $g(x)$ so that the random variable Y would have the probability density function shown in Fig. B.3. Assume $y = g(x)$ has only one solution and will build the function $g(x)$ with such a property. It is also assumed that the random variable X is uniformly distributed between 0 and 1, i.e.,

$$f_X(x) = \begin{cases} 1 & : & 0 \le x < 1 \\ 0 & : & \text{otherwise} \end{cases} \tag{B.50}$$

For the case where $Pr\{i\} \propto i$, the following probability density function is used. See Fig. B.3(a).

$$f_Y(y) = \begin{cases} 1/\alpha & : & 1 \le y < 2 \\ 2/\alpha & : & 2 \le y < 3 \\ \vdots & & \\ M/\alpha & : & M \le y < M+1 \end{cases} \tag{B.51}$$

where M is the block size and

$$\alpha = \sum_{l=1}^{M} l \tag{B.52}$$

From (B.49), (B.50), and (B.51), we have the following equation for $g(x)$.

$$\frac{i}{\alpha} = \frac{1}{g'(x)} \quad : \quad i \le g(x) < i+1 \tag{B.53}$$

for $i = 1, 2, \cdots, M$. Therefore,

$$g(x) = \frac{\alpha}{i} x + c_i \quad : \quad i \le g(x) < i+1 \tag{B.54}$$

134

for $i = 1, 2, \cdots, M$. To find c_i, note that from (B.54),

$$\frac{i(i - c_i)}{\alpha} \leq x < \frac{i(i + 1 - c_i)}{\alpha} \tag{B.55}$$

for $i = 1, 2, \cdots, M$. Since $x \geq 0$, set $\dfrac{i(i - c_i)}{\alpha} = 0$ for $i = 1$, which gives $c_1 = 1$. The following condition is also imposed on (B.55), because x is a continues variable.

$$\frac{i(i + 1 - c_i)}{\alpha} = \frac{(i + 1)(i + 1 - c_{i+1})}{\alpha} \tag{B.56}$$

or equivalently,

$$(i + 1)c_{i+1} = ic_i + i + 1 \tag{B.57}$$

for $i = 1, 2, \cdots, M - 1$. Solving this recursive equation with $c_1 = 1$ gives

$$c_i = \frac{i + 1}{2} \tag{B.58}$$

for $i = 1, 2, \cdots, M$. From (B.54), (B.55), and (B.58) we have

$$g(x) = \frac{\alpha x}{i} + \frac{i + 1}{2} \quad : \quad \frac{i(i - 1)}{2\alpha} \leq x < \frac{i(i + 1)}{2\alpha} \tag{B.59}$$

Similarly, for the case where $Pr\{i\} \propto i^{-1}$, the following probability density function is assumed. See Fig. B.3(b).

$$f_Y(y) = \begin{cases} 1/\alpha & : & 1 \leq y < 2 \\ 2^{-1}/\alpha & : & 2 \leq y < 3 \\ \vdots & & \\ M^{-1}/\alpha & : & M \leq y < M + 1 \end{cases} \tag{B.60}$$

where M is the block size and

$$\alpha = \sum_{l=1}^{M} l^{-1} \tag{B.61}$$

From (B.49), (B.50), and (B.60), we have the following equation for $g(x)$.

$$\frac{1}{i\alpha} = \frac{1}{g'(x)} \quad : \quad i \le g(x) < i+1 \tag{B.62}$$

for $i = 1, 2, \cdots, M$. Therefore,

$$g(x) = i\alpha x + c_i \quad : \quad i \le g(x) < i+1 \tag{B.63}$$

for $i = 1, 2, \cdots, M$. From (B.63),

$$\frac{i - c_i}{\alpha i} \le x < \frac{i+1-c_i}{\alpha i} \tag{B.64}$$

for $i = 1, 2, \cdots, M$. Since $x \ge 0$, set $\dfrac{i - c_i}{\alpha i} = 0$ for $i = 1$, which gives $c_1 = 1$. Moreover, continuity of x results in

$$\frac{i+1-c_i}{\alpha i} = \frac{i+1-c_{i+1}}{\alpha(i+1)} \tag{B.65}$$

or equivalently,

$$c_{i+1} = (c_i - 1)\frac{i+1}{i} \tag{B.66}$$

for $i = 1, 2, \cdots, M - 1$. From (B.63) and (B.64), we have

$$g(x) = i\alpha x + c_i \quad : \quad \frac{(i - c_i)}{\alpha i} \le x < \frac{i+1-c_i}{\alpha i} \tag{B.67}$$

where c_i is found from (B.66) with $c_1 = 1$.
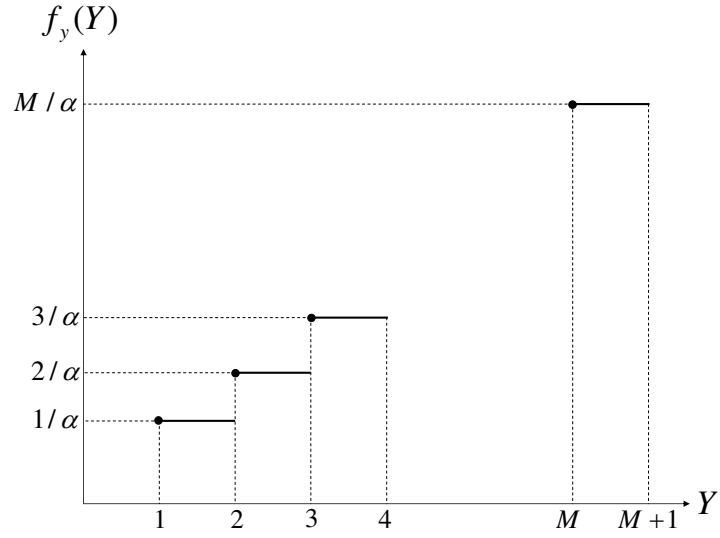
(a) Probability of choosing a row or column is directly proportional to its index i.
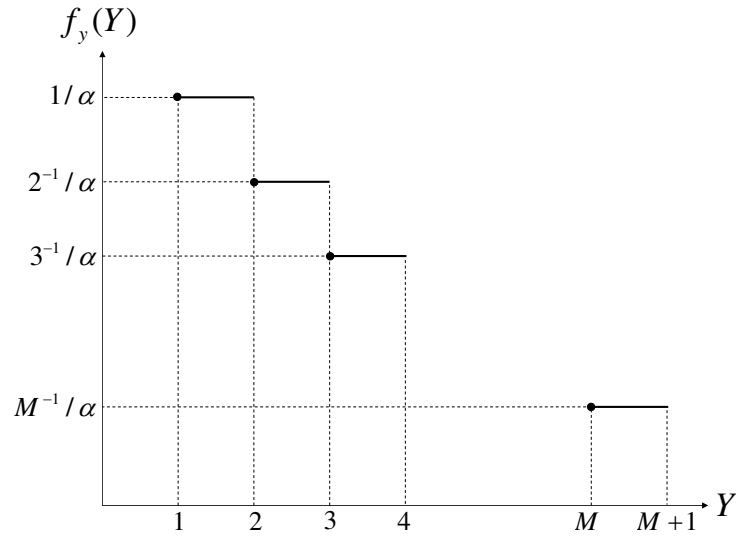
(b) Probability of choosing a row or column is inversely proportional to its index i.

Figure B.3: Probability density functions used for sampling rows and columns of the blocks in the impedance matrix in Chapter 3.

BIBLIOGRAPHY

[1] W. S. Ament, "Forward- and Back-Scattering From Certain Rough Surfaces," *IEEE Transactions on Antennas and Propagation*, vol. 4, no. 3, pp. 369–373, July 1956.

[2] V. Twersky, "On Scattering and Reflection of Electromagnetic Waves by Rough Surfaces," *IEEE Transactions on Antennas and Propagation*, vol. 5, no. 1, pp. 81–90, January 1957.

[3] P. Beckmann, "A New Approach to the Problem of Reflection From a Rough Surface," *Acta Technica CSAV*, vol. 2, no. 4, pp. 311–355, 1957.

[4] T. M. Elfouhaily and C.-A. Guerin, "A Critical Survey of Approximate Scattering Wave Theories From Random Rough Surfaces," *Waves in Random Media*, vol. 14, no. 4, pp. R1–R40, October 2004.

[5] J. R. Lundien, "Terrain Analysis by Electromagnetic Means, Report 2: Radar Responses to Laboratory Responses Soil Samples," *U.S. Army Corps of Engineers Waterwaves Experiment Station Technical Report 3-693*, Vicksburg, MS, September 1966.

[6] A. T. Edgerton, "Engineering Applications of Microwave Radiometry," in *Proceedings of the 5th International Symposium on Remote Sensing of Environment*, 1968.

[7] F. T. Ulaby, "Radar Measurement of Soil Moisture Content," *IEEE Transactions on Antennas and Propagation*, vol. 22, no. 2, pp. 257–265, March 1974.

[8] G. A. Poe, "Remote Sensing of the Near-Surface Moisture Profile of Specular Soils With Multi-Frequency Microwave Radiometry," in *SPIE Proceedings*, vol. 27, November 1971, pp. 135–145.

[9] E. G. Njoku and J. A. Kong, "Theory for Passive Microwave Remote Sensing of Near-Surface Soil Moisture," *Journal of Geophysical Research*, vol. 82, no. 20, pp. 3108–3118, 1977.

[10] Y. Oh, K. Sarabanadi, and F. T. Ulaby, "An empirical Model and an Inversion Technique for Radar Scattering From Bare Soil Surfaces," *IEEE Transactions on Geoscience and Remote Sensing*, vol. 30, no. 2, pp. 370–381, March 1992.

[11] P. C. Dubois, J. J. Van Zyl, and E. T. Engman, "Measuring Soil Moisture With Imaging Radar," *IEEE Transactions on Geoscience and Remote Sensing*, vol. 33, no. 4, pp. 915–926, July 1995.

[12] F. Lemaitre, J. C. Poussiere, Y. H. Kerr, M. Dejus, R. Durbe, P. de Rosnay, and J. C. Calvet, "Design and Test of the Ground-Based L-Band Radiometer for Estimating Water in Soils (LEWIS)," *IEEE Transactions on Geoscience and Remote Sensing*, vol. 42, no. 8, pp. 1666–1676, August 2004.

[13] U. Narayan, V. Lakshmi, and T. J. Jackson, "High-Resolution Change Estimation of Soil Moisture Using L-Band Radiometer and Radar Observations Made During the SMEX02 Experiments," *IEEE Transactions on Geoscience and Remote Sensing*, vol. 44, no. 6, pp. 1545–1554, June 2006.

[14] D. Entekhabi, E. G. Njoku, P. Houser, M. Spencer, T. Doiron, K. Yunjin, J. Smith, R. Girard, S. Belair, W. Crow, T. J. Jackson, Y. H. Kerr, J. S. Kimball, R. Koster, K. C. McDonald, P. E. O'Neill, T. Pultz, S. W. Running, S. Jiancheng, E. Wood, and J. van Zyl, "The Hydrosphere State (Hydros) Satellite Mission: An Earth System Pathfinder for Global Mapping of Soil Moisture and Land Freeze/Thaw," *IEEE Transactions on Geoscience and Remote Sensing*, vol. 42, no. 10, pp. 2184–2195, October 2004.

[15] Z. Xiwu, P. R. Houser, J. P. Walker, and W. T. Crow, "A Method for Retrieving High-Resolution Surface Soil Moisture From Hydros L-Band Radiometer and Radar Observations," *IEEE Transactions on Geoscience and Remote Sensing*, vol. 44, no. 6, pp. 1534–1544, June 2006.

[16] M. C. Dobson, F. T. Ulaby, T. LeToan, A. Beaudoin, E. S. Kasischke, and N. Christensen, "Dependence of Radar Backscatter on Coniferous Forest Biomass," *IEEE Transactions on Geoscience and Remote Sensing*, vol. 30, no. 2, pp. 412–415, March 1992.

[17] E. Rignot, R. Zimmermann, J. van Zyl, and R. Oren, "Spaceborne Applications of a P-Band Imaging Radar for Mapping of Forest Biomass," *IEEE Transactions on Geoscience and Remote Sensing*, vol. 33, no. 5, pp. 1162–1169, September 1995.

[18] M. Moghaddam, S. Saatchi, and R. H. Cuenca, "Estimating Subcanopy Soil Moisture With Radar," *Journal of Geophysical Research*, vol. 105, no. D11, pp. 14899–14911, 2000.

[19] M. Moghaddam, Y. Rahmat-Samii, E. Rodriguez, D. Entekhabi, J. Hoffman, D. Moller, L. E. Pierce, S. Saatchi, and M. Thomson, "Microwave Observatory of Subcanopy and Subsurface (MOSS): A Mission Concept for Global Deep Soil Moisture Observations," *IEEE Transactions on Geoscience and Remote Sensing*, vol. 45, no. 8, pp. 2630–2643, August 2007.

[20] G. A. Maykut, "Energy Exchange Over Young Sea Ice in the Central Arctic," *Journal of Geophysical Research*, vol. 83, no. C7, pp. 3646–3658, July 1978.

[21] G. A. Maykut, "Large-Scale Heat Exchange and Ice Production in the Central Arctic," *Journal of Geophysical Research*, vol. 87, no. C10, pp. 7971–7984, September 1982.

[22] W. Dierking and T. Busche, "Sea Ice Monitoring by L-Band SAR: An Assessment Based on Literature and Comparisons of JERS-1 and ERS-1 Imagery," *IEEE Transactions on Geoscience and Remote Sensing*, vol. 44, no. 2, pp. 957–970, April 2006.

[23] N. P. Walker, K. C. Partington, M. L. Van Woert, and T. L. T. Street, "Arctic Sea Ice Type and Concentration Mapping Using Passive and Active Microwave Sensors," *IEEE Transactions on Geoscience and Remote Sensing*, vol. 44, no. 12, pp. 3574–3584, December 2006.

[24] P. Kanagaratnam, T. Markus, V. Lytle, B. Heavey, P. Jansen, G. Prescott, and S. P. Gogineni, "Ultrawideband Radar Measurements of Thickness of Snow Over Sea Ice,"

IEEE Transactions on Geoscience and Remote Sensing, vol. 45, no. 9, pp. 2715–2724, September 2007.

[25] A. Ishimaru, "Backscattering Enhancement: From Radar Cross Sections to Electron and Light Localizations to Rough Surface Scattering," *IEEE Antennas and Propagation Magazine*, vol. 33, no. 5, pp. 7–11, October 1991.

[26] A. R. McGurn and A. A. Maradudin, "Localization Effects in the Elastic Scattering of Light From a Randomly Rough Surface," *Journal of the Optical Society of America B*, vol. 4, no. 6, pp. 910–926, June 1987.

[27] A. A. Maradudin and E. R. Mendez, "Enhanced Backscattering of Light From Weakly Rough, Random Metal Surfaces," *Applied Optics*, vol. 32, no. 19, pp. 3335–3343, July 1993.

[28] K. A. O'Donnell, R. Torre, and C. S. West, "Observations of Second-Harmonic Generation From Randomly Rough Metal Surfaces," *Physical Review B*, vol. 55, no. 12, pp. 7985–7992, March 1997.

[29] E. Betzig, A. Lewis, A. Harootunian, M. Isaacson, and E. Kratschmer, "Near-Field Scanning Optical Microscopy (NSOM): Development and Biophysical Applications," *Biophysical Journal*, vol. 49, no. 1, pp. 269–279, January 1986.

[30] D. Entekhabi and M. Moghaddam, "Mapping Recharge From Space: Roadmap to Meeting the Grand Challenge," *Hydrogeology Journal*, vol. 15, no. 1, February 2007.

[31] S. V. Nghiem, R. Kwok, S. H. Yueh, and M. R. Drinkwater, "Polarimetric Signatures of Sea Ice: 1. Theoretical Model," *Journal of Geophysical Research*, vol. 100, no. C7, pp. 13665–13679, July 1995.

[32] C.-h. Kuo and M. Moghaddam, "A Theoretical Analysis of Backscattering Enhancement Due to Surface Plasmons From Multilayer Structures With Rough Interfaces," *IEEE Transactions on Antennas and Propagation*, vol. 56, no. 4, pp. 1133–1143, April 2008.

[33] N. R. Peplinski, F. T. Ulaby, and M. C. Dobson, "Dielectric Properties of Soils in the 0.3–1.3-GHz Range," *IEEE Transactions on Geoscience and Remote Sensing*, vol. 33, no. 3, pp. 803–807, May 1995.

[34] S. O. Rice, "Reflection of Electromagnetic Waves From Slightly Rough Surfaces," *Communications on Pure and Applied Mathematics*, vol. 4, no. 2/3, pp. 351–378, 1951.

[35] G. C. Brown, V. Celli, M. Haller, and A. Marvin, "Vector Theory of Light Scattering From a Rough Surface: Unitary and Reciprocal Expansions," *Surface Science*, vol. 136, no. 2/3, pp. 381–397, January 1984.

[36] A. R. McGurn and A. A. Maradudin, "Perturbation Theory Results for the Diffuse Scattering of Light From Two-Dimensional Randomly Rough Metal Surfaces," *Waves in Random Media*, vol. 6, no. 3, pp. 251–267, July 1996.

141

[37] L. Tsang, J.A. Kong, and R.T. Shin, *Theory of Microwave Remote Sensing*. New York, NY: Wiley, 1985.

[38] J. T. Johnson, "Third-Order Small Perturbation Method for Scattering From Dielectric Rough Surfaces," *Journal of the Optical Society of America A*, vol. 16, no. 11, pp. 2720–2736, November 1999.

[39] K. F. Warnick and W. C. Chew, "Numerical Simulation Methods for Rough Surface Scattering," *Waves in Random Media*, vol. 11, no. 1, pp. R1–R30, January 2001.

[40] F. D. Hastings, J. B. Schneider, and S. L. Broschat, "A Monte-Carlo FDTD Technique for Rough Surface Scattering," *IEEE Transactions on Antennas and Propagation*, vol. 43, no. 11, pp. 1183–1191, November 1995.

[41] H. T. Chou and J. T. Johnson, "A Novel Acceleration Algorithm for the Computation of Scattering From Rough Surfaces With the Forward-Backward Method," *Radio Science*, vol. 33, no. 5, pp. 1277–1287, September–October 1998.

[42] D. A. Kapp and G. S. Brown, "A New Numerical Method for Rough-Surface Scattering Calculations," *IEEE Transactions on Antennas and Propagation*, vol. 44, no. 5, pp. 711–721, May 1996.

[43] V. Jandhyala, E. Michielssen, S. Balasubramaniam, and W. C. Chew, "A Combined Steepest Descent-Fast Multipole Algorithm for the Fast Analysis of Three-Dimensional Scattering by Rough Surfaces," *IEEE Transactions on Geoscience and Remote Sensing*, vol. 36, no. 3, pp. 738–748, May 1998.

[44] I. M. Fuks and A. G. Voronovich, "Wave Diffraction by Rough Interfaces in an Arbitrary Plane-Layered Medium," *Waves in Random Media*, vol. 10, no. 2, pp. 253–272, April 2000.

[45] G. Franceschetti, P. Imeratore, A. Iodice, D. Riccio, and G. Ruello, "Scattering From Layered Medium With One Rough Interface: Comparison and Physical Interpretation of Different Methods," in *Proceedings of IEEE IGARSS*, Toulouse, France, July 2003, pp. 2912–2914.

[46] R. Azadegan and K. Sarabandi, "Analytical Formulation of the Scattering by a Slightly Rough Dielectric Boundary Covered With a Homogeneous Dielectric Layer," in *Proceedings of IEEE AP-S International Symposium*, Columbus, Ohio, June 2003, pp. 420–423.

[47] K. Krishen, "Scattering of Electromagnetic Waves From a Layer With Rough Front and Plane Back (Small Perturbation Method by Rice)," *IEEE Transactions on Antennas and Propagation*, vol. 18, no. 4, pp. 573–576, July 1970.

[48] A. Soubret, G. Berginc, and C. Bourrely, "Backscattering Enhancement of an Electromagnetic Wave Scattered by Two-Dimensional Rough Layers," *Journal of the Optical Society of America A*, vol. 18, no. 11, pp. 2778–2788, November 2001.

[49] C.-h. Kuo and M. Moghaddam, "Bistatic Scattering From Multilayer Rough Surfaces Based on the Extended Boundary Condition Method Regularized Using Truncated Singular Value Decomposition," *IEEE Transactions on Antennas and Propagation*, vol. 54, no. 10, pp. 2917–2929, October 2006.

[50] R. E. Collin, *Antenna and Radio Wave Propagation*. New York, NY: McGraw-Hill, 1985.

[51] J. A. Kong, *Electromagnetic Wave Theory*. Cambridge, MA: EMW Publishing, 2000.

[52] A. J. Poggio and E. K. Miller, "Integral Equation Solution of Three Dimensional Scattering Problems," in *Computer Techniques for Electromagnetics*, R. Mittra, Ed. Elmsford, NY: Pergamon Press, 1973, pp. 159–264.

[53] Y. Chang and R. F. Harrington, "A Surface Formulation for Characteristic Modes of Material Bodies," *IEEE Transactions on Antennas and Propagation*, vol. 25, no. 6, November 1977.

[54] T. K. Wu and L. L. Tsai, "Scattering from Arbitrarily-Shaped Lossy Dielectric Bodies of Revolution," *Radio Science*, vol. 12, no. 5, November 1977.

[55] L. Tsang, D. Chen, P. Xu, Q. Li, and V. Jandhyala, "Wave Scattering With the UV Multilevel Partitioning Method: 1. Two-Dimensional Problem of Perfect Electric Conductor Surface Scattering," *Radio Science*, vol. 39, no. 5, October 2004.

[56] P. Beckmann and A. Spizzichino, *The Scattering of Electromagnetic Waves from Rough Surfaces*, Oxford, NY: Pergamon Press, 1963.

[57] R. F. Harrington, *Field Computation by Moment Methods*. New York, NY: McMillan, 1963.

[58] E. I. Thorsos, "The Validity of the Kirchhoff Approximation Far Rough Surface Scattering Using a Gaussian Roughness Spectrum," *Journal of the Acoustical Society of America*, vol. 83, no. 1, pp. 78–92, January 1988.

[59] E. I. Thorsos and D. R. Jackson, "The Validity of the Perturbation Approximation for Rough Surface Scattering Using a Gaussian Roughness Spectrum," *Journal of the Acoustical Society of America*, vol. 86, no. 1, pp. 261–277, July 1989.

[60] J. M. Soto-Crespo, M. Nieto-Vesperinas, and A. T. Friberg, "Scattering From Slightly Rough Random Surfaces: A Detailed Study on the Validity of the Small Perturbation Method," *Journal of the Optical Society of America A*, vol. 7, no. 7, pp. 1185–1201, July 1990.

[61] F. Millet and K. Warnick, "Validity Study of Rough Surface Scattering Models," in *Proceedings of IEEE AP-S International Symposium*, Columbus, Ohio, June 2003, pp. 565–568.

[62] M.-J. Kim and A. J. Stoddart, "The Region of Validity of Perturbation Theory," *Waves in Random Media*, vol. 3, no. 4, pp. 325–342, October 1993.

[63] M.-J. Kimt, H. M. Berenyi, R. E. Burge, and S. Tajbakhsh, "Region of Validity of Perturbation Theory for Dielectrics and Finite Conductors," *Waves in Random Media*, vol. 5, no. 3, pp. 305–327, July 1995.

[64] L. Tsang, J. A. Kong, K.-H. Ding, and C. O. Ao, *Scattering of Electromagnetic Waves: Numerical Simulations.* New York, NY: John Wiley and Sons, 2001.

[65] R. W. Freund, "A Transpose-Free Quasi-Minimal Residual Algorithm for Non-Hermitian Linear Systems," *SIAM Journal on Scientific Computing*, vol. 14, no. 2, pp. 470–482, March 1993.

[66] F. T. Ulaby, R. K. Moore, and A. K. Fung, *Microwave Remote Sensing: Active and Passive.* Reading, MA: Addison-Wesley, 1982.

[67] J. Shi, L. Jiang, L. Zhang, K. S. Chen, J.-P. Wigneron, A. Chanzy, and T. J. Jackson, "Physically Based Estimation of Bare-Surface Soil Moisture With the Passive Radiometers," *IEEE Transactions on Geoscience and Remote Sensing*, vol. 44, no. 11, pp. 3145–3153, November 2006.

[68] F. T. Ulaby, P. P. Batlivala, and M. C. Dobson, "Microwave Backscatter Dependence on Surface Roughness, Soil Moisture, and Soil Texture: Part I—Bare Soil," *IEEE Transactions on Geoscience and Remote Sensing*, vol. 16, no. 4, pp. 286–295, October 1978.

[69] M. C. Dobson and F. T. Ulaby, "Preliminary Evaluation of the SIR-B Response to Soil Moisture, Surface Roughness, and Crop Cover Canopy," *IEEE Transactions on Geoscience and Remote Sensing*, vol. 24, no. 4, pp. 517–527, July 1986.

[70] Y. Oh, K. Sarabandi, and F. T. Ulaby, "An Inversion Algorithm for Retrieving Soil Moisture and Surface Roughness From Polarimetric Radar Observation," in *Proceedings of IEEE IGARSS*, Pasadena, California, August 1994, pp. 1582–1584.

[71] M. El-Shenawee, "Polarimetric Scattering From Two-Layered Two-Dimensional Random Rough Surfaces With and Without Buried Objects," *IEEE Transactions on Geoscience and Remote Sensing*, vol. 42, no. 1, pp. 67–76, January 2004.

[72] M. El-Shenawee and E. L. Miller, "Multiple-Incidence and Multifrequency for Profile Reconstruction of Random Rough Surfaces Using the 3-D Electromagnetic Fast Multipole Model," *IEEE Transactions on Geoscience and Remote Sensing*, vol. 42, no. 11, pp. 2499–2510, November 2004.

[73] K. S. Rao, S. Raju, and J. R. Wang, "Estimation of Soil Moisture and Surface Roughness Parameters From Backscattering Coefficient," *IEEE Transactions on Geoscience and Remote Sensing*, vol. 31, no. 5, pp. 1094–1099, September 1993.

[74] J. C. Souyris, L. Wang, C. C. Hsu, J. A. Kong, T. Le Toan, N. Boudier, S. H. Yueh, U. Wegmuller, and C. Matzler, "Inversion of Soil Moisture With Radar Backscattering Data," in *Proceedings of IEEE IGARSS*, Pasadena, California, August 1994, pp. 1392–1394.

[75] C. Notarnicola, M. Angiulli, and F. Posa, "Soil Moisture Retrieval From Remotely Sensed Data: Neural Network Approach versus Bayesian Method," *IEEE Transactions on Geoscience and Remote Sensing*, vol. 46, no. 2, pp. 547–557, February 2008.

[76] L. Zongqian and T. Yuhua, "Inversion for Moisture and Roughness of Bare Soil From Backscattering Coefficients Based upon the Model of Wet Soil and the Scattering Models," in *Proceedings of SPIE*, vol. 3503, pp. 238–244, September 1998.

[77] Y. Oh, "Robust Inversion Technique for Retrieving Soil Moisture From Multi-Polarised Backscatter of Bare Surface," *IEE Electronic Letters*, vol. 42, no. 7, pp. 414–415, March 2006.

[78] J. Shi, J. Wang, A. Y. Hsu, P. E. O'Neill, and E. T. Engman, "Estimation of Bare Soil Moisture and Surface Roughness Parameter Using L-Band SAR Image Data," *IEEE Transactions on Geoscience and Remote Sensing*, vol. 35, no. 5, pp. 1254–1266, September 1997.

[79] B. C. K. Tso and P. M. Mather, "Classification of Multisource Remote Sensing Imagery Using a Genetic Algorithm and Markov Random Fields," *IEEE Transactions on Geoscience and Remote Sensing*, vol. 37, no. 3, pp. 1255–1260, May 1999.

[80] W. H. Slade, H. W. Ressom, M. T. Musavi, and R. L. Miller, "Inversion of Ocean Color Observations Using Particle Swarm Optimization," *IEEE Transactions on Geoscience and Remote Sensing*, vol. 42, no. 9, pp. 1915–1923, September 2004.

[81] M. C. Dobson, F. T. Ulaby, M. T. Hallikainen, and M. A. El-Rayes, "Microwave Dielectric Behavior of Wet Soil—Part II: Dielectric Mixing Models," *IEEE Transactions on Geoscience and Remote Sensing*, vol. GE-23, no. 1, pp. 35–46, January 1985.

[82] M. R. Vant, R. O. Ramseier, and V. Makros, "The Complex Dielectric Constant of Sea Ice at Frequencies in the Range 0.1–40 GHz," *Journal of Applied Physics*, vol. 49, no. 3, pp. 1264–1280, March 1978.

[83] S. Kirkpatrick, C. D. Gelatt, and M.P. Vecchi, "Optimization by Simulated Annealing," *Science*, vol. 220, no. 4598, pp. 671–680, May 1983.

[84] S. Kirkpatrick, "Optimization by Simulated Annealing: Quantitative Studies," *Journal of Statistical Physics*, vol. 34, no. 5/6, pp. 975–986, March 1984.

[85] N. Metropolis, A. Rosenbluth, M. Rosenbluth, A. Teller, and M. Teller, "Equation of State Calculations by Fast Computing Machines," *Journal of Chemical Physics*, vol. 21, no. 6, pp. 1087–1092, June 1953.

[86] A. Corana, M. Marchesi, C. Martini, and S. Ridella, "Minimizing Multimodal Functions of Continuous Variables With the "Simulated Annealing" Algorithm," *ACM Transactions on Mathematical Software*, vol. 13, no. 3, pp. 262–280, September 1987.

[87] P. J. M. van Laarhoven and E. H. L. Aarts, *Simulated Annealing: Theory and Applications*, Dordrecht, Holland: D. Reidel Publishing Company, 1987.

[88] L. Ingber, "Very Fast Simulated Re-Annealing," *Mathematical and Computer Modelling*, vol. 12, no. 8, pp. 967–973, 1989.

[89] R. K. Chunduru, M. K. Senz, and P. L. Stoffa, "Hybrid Optimization Methods for Geophysical Inversion," *Geophysics*, vol. 62, no. 4, pp. 1196–1207, July–August 1997.

[90] C.-h. Kuo and M. Moghaddam, "Electromagnetic Scattering From Multilayer Rough Surfaces With Arbitrary Dielectric Profiles for Remote Sensing of Subsurface Soil Moisture," *IEEE Transactions on Geoscience and Remote Sensing*, vol. 45, no. 2, pp. 349–366, February 2007.